Rayleigh Wave Interactions with Tribological Contacts

Eng Seng OOI

Thesis submitted for the degree of Doctor of Philosophy

Department of Mechanical Engineering

University of Sheffield

March 2015

Summary

The use of ultrasonic reflectometry is a proven method of condition monitoring machine systems. The working principles are simple. A burst of ultrasonic signal is sent to the interface of interest where reflection of the signal takes place. The manner in which reflection takes place depends on the properties of the interface. As such, the reflected signal carries information regarding the interface that can be extracted with proper techniques.

However, the use of ultrasonic reflectometry in condition monitoring is not without its limitations. Conventional ultrasound techniques make use of ultrasonic bulk waves that travel through the body of a given material. Problems arise when the medium through which the wave travels is attenuative. This prevents any passage of ultrasonic signals as most of the energy will be absorbed by the material. In addition, most components have complex designs, requiring that the signal pass through multiple interfaces before reaching the interface of interest. Reflections occur at these intermediate interfaces, reducing the overall energy content of the signal.

In order to overcome these issues, the use of Rayleigh wave as an alternative is researched in the work carried out here. Instead of having to travel through the bulk of the material, Rayleigh waves function by propagating along the free surface of the said material, thereby circumventing the existing issues with the use of conventional bulk waves.

The research here was carried out to seek an understanding of how Rayleigh waves interact with a contact interface. This was performed on three separate fronts. First, a novel analytical model was developed by modelling the contact interface as a series of springs. It is discovered that the stiffness of the springs are directly proportional to the reflection coefficient of the Rayleigh wave incident upon the interface. The implication of this finding is that rough interfaces will have a lesser reflection coefficient (due to decreased stiffness), with a perfectly smooth interface giving the maximum reflection coefficient obtainable from a particular interface.

This was then followed by studies performed using both finite element simulations as well as experimental work. Data from all three studies (analytical model, finite element simulations and experimental work) were compared against each other and it was shown that a good agreement exists between all three methods.

Exploratory work on lip seals were performed in order to research the potential of using Rayleigh wave as a condition monitoring tool. By measuring the delay in the time of arrival of a Rayleigh wave pulse reflected from the sealing zone, it is possible to measure the extent of misalignment that is present in a lip seal. Axial misalignments of the lip between 6mm to 8mm were successfully measured. Additional work in measuring the degradation of a lubricating film via evaporation was qualitative in nature, with the amplitude of the reflected pulse slowly decreasing as the layer of fluid at the sealing zone diminishes via evaporation.

Contents

Acknowledgements

Nomenclature

Greek Alphabet

Symbol	Description	Units
α	Longitudinal wave attenuation coefficient	Nepers/m
α	Approach of bodies under compression (section 5.4.2)	m
α	$\sqrt{k_l^2 - k^2}$, defined in the calculation of Lamb wave dispersion curves (section 3.5)	m^{-1}
β	Shear wave attenuation coefficient	Nepers/m
β	Radius of asperity tip	m
β	$\sqrt{k_t^2 - k^2}$, defined in the calculation of Lamb wave dispersion curves (section 3.5)	m^{-1}
γ	Rayleigh wave attenuation coefficient	Nepers/m
η	Asperity density	m^{-2}
η_r	c_r/c_s	Dimensionless
θ	Angle	Degrees
λ	Wavelength	m
v	Poisson's ratio	Dimensionless
ξ	c_s/c_l	Dimensionless
ρ	Density	kg/m^3
ς	Dimensionless coefficient quantifying Rayleigh wave attenuation coefficient	Dimensionless
σ	RMS roughness	m
ω	Angular frequency	Radians/s
$\varphi, \varphi', \psi, \psi'$	Dimensionless constants used to calculate reflected Rayleigh wave	Dimensionless

Miscellaneous symbols

Symbol	Description	Units
A_x	Wave amplitude at x	N/A
A_m	Asymmetrical lamb wave mode where m is an integer starting from 0 denoting the exact mode	N/A
a	Hertzian half contact width	µm
B	Rayleigh wave amplitude coefficient	Dimensionless
C	Stiffness ratio	Dimensionless
c_l	Longitudinal wave velocity	m/s
c_s	Shear wave velocity	m/s
c_r	Rayleigh wave velocity	m/s
D	Diameter of cylinder	m or mm
d	Thickness of substrate	m
E	Young's modulus	GPa
E'	Combined Young's modulus	GPa
F_y	Vertical excitation force applied to generate Rayleigh waves in FE simulations	N
$\boldsymbol{F}$	Spring force vector in finite element calculations	N
f	Frequency	MHz
G	Shear modulus	GPa
$\boldsymbol{g}$	Body forces	N
h	Lubricant film thickness	m
h or $h(x)$	Nominal separation of the interface	m
h_o	Central seperation	m
K	Layer stiffness	GPa/m
K_σ	Normal stiffness	MN/m
K_τ	Tangential stiffness	MN/m

k_i	Stiffness for a single asperity, i	N/m
$k_{\sigma\text{-}asperity}$	Distributed asperity stiffness	MN/m^2
k_l, k_t, k_r	Wavenumber of longitudinal, shear and Rayleigh waves	m^{-1}
$\boldsymbol{k_p}$	Vector of spring stiffness	N/m
l	Half the width of the line contact	m
l_t	Distance travelled by a wave	m
M	Coefficient used in determining the minimum required thickness of a substrate	Dimensionless
N	Total number of asperity at the interface	Dimensionless
n	Number of asperities that are in contact	Dimensionless
P	Total load applied to the line contact	N
P_i	Load on a single asperity, i	N
$p, p(z,x)$	Pressure profile of a rough line contact	N/m
R	Reflection coefficient	Dimensionless
R_x, R_y	Component of R in the x and y direction	Dimensionless
R_a	Centre line average of roughness	μm
S_m	Symmetrical lamb wave mode where m is an integer starting from 0 denoting the exact mode	N/A
s	Stress tensor	N
T	Transmission coefficient	Dimensionless
t	time	s
$\boldsymbol{u}$	Displacement vector	m
$\boldsymbol{u_o}$	Initial spring displacement vector	m
W_I	Incident Rayleigh wave displacements in the y-direction	m
U_I	Incident Rayleigh wave displacements in the x-direction	m

W_{RI}, U_{RI}	Reflected Rayleigh wave displacements in the y and x directions due to W_I	m
W_{R2}, U_{R2}	Reflected Rayleigh wave displacements in the y and x directions due to U_I	m
x	x-coordinate	m
x	Distance where A_0 and S_0 modes behave like Rayleigh waves	m
z	Acoustic impedance in material	kgm^2s
δF	Periodic force due to spring excitation	N

Abbreviations

DAQ	Data acquisition
EMAT	Electromagnetic transducers
FE	Finite element
FEA	Finite element analysis
IBEM	Indirect boundary element method
IDT	Interdigital transducers
NDT	Non destructive testing
PC	Personal computer
SAW	Surface acoustic wave
TOF	Time of flight
UPR	Ultrasonic pulser receiver

1 Introduction

1.1 Problem Statement

Condition monitoring plays a vital role in ensuring that machinery does not fail unexpectedly. This prevents unexpected breakdowns from occurring and at the same time, allows predictive maintenance to be scheduled effectively. All of this increases machine uptime and reduces overall operating costs by mitigating losses due to unexpected machine failure.

At the core of all these are the techniques involved in condition monitoring where ultrasonic methods have been a continual mainstay. Over the years, pioneering methods have been developed using ultrasonic principles, allowing accurate predictions of contact parameters such as lubricant film thickness in common but essential components such as bearings.

In general, conventional ultrasonic methods work by sending a pulse of high frequency waves through the bulk of the material to interrogate a particular system. One limitation to this occurs when the wave tries to travel through highly attenuative materials such as elastomeric seals and rubber gaskets, which are a common occurrence in most machine systems. The bulk of the ultrasonic energy is absorbed by the materials, preventing any passage of ultrasound.

Additionally, the interior of machineries are rarely homogeneous and often consist of multiple interfaces and discontinuities through which the pulse would have to pass through before reaching the intended interface. This results in spurious reflections emerging from the intermediate interfaces, resulting in an overall deterioration of signal quality.

One alternative that shows potential is in the use of Rayleigh waves whereby the waves travel along the surface of the material instead of through the bulk. This mitigates the issues encountered when using conventional ultrasonic wave modes. An immediate application for Rayleigh waves is in the condition monitoring of lip seals commonly found in rotary applications such as wind turbines. The limitations inherent to bulk waves can be circumvented by sending the Rayleigh wave down the axis of the shaft towards the sealing zone.

However, the use of Rayleigh waves in probing an inteface have been limited, with only a meagre understanding of the mechanisms that governs the interaction of Rayleigh waves with an interface. Therefore, in order for Rayleigh waves to be viable, it is crucial to first develop a better understanding of how a Rayleigh wave responds to an interface in order to allow interpretation of any possible expeirmantal data.

1.2 Aims and Objectives

The aim of this research is to develop an improved understanding of the physical mechanisms that governs Rayleigh wave reflection from an interface. This would allow more information to be extracted from Rayleigh wave data, allowing for better condition monitoring capabilities using Rayleigh waves.

The following are the objectives of the project:

- Develop a meaningful understanding of Rayleigh waves by developing an intuitive analytical model cast in a form that uses physical quantities of practical significance.

- Validation of the analytical model using finite element simulations.

- Perform experiments to simultaneously study how Rayleigh waves reflects from an interface and to obtain experimental data which can then be compared to results obtained from both the analytical model and finite element simulations.

- Demonstrate the potential of using Rayleigh wave through exploratory work performed on lip seals.

1.3 Thesis Layout

This thesis is divided into 9 chapters in total. A brief summary of each chapter (excluding the introduction) is given below:

Chapter 2 Background of Ultrasonic Techniques
In this chapter, the background of ultrasonic systems is given. The governing physics of conventional ultrasound are introduced. Common applications that take advantage of useful ultrasound properties are discussed. This is then followed by a discourse on the developments of ultrasound in the field of Tribology.

Chapter 3 Background of Rayleigh Wave
This chapter serves to provide the necessary background on Rayleigh waves. Important features of Rayleigh waves such as its propagation characteristic and methods of generation are detailed. The practical considerations of utilizing Rayleigh waves are introduced here and will be applied when performing the experiments in Chapter 7. Existing applications of Rayleigh waves in various fields are discussed next.

Chapter 4 Rayleigh Wave Reflection – Literature Review
Rayleigh waves can reflect from a variety of sources. Here, the existing literatures pertaining to Rayleigh wave reflection are reviewed.

Chapter 5 An Analytical Model of Rayleigh Wave Reflection from an Interface

The development of a novel model that describes Rayleigh wave interactions with a contact interface is detailed in this chapter. The contact interface is modelled as a series of springs characterised by their stiffness. In this way, a relationship between reflection coefficient and interface stiffness was established. Interfaces with varying roughness and contact pairs were studied using this new model and the results are presented and discussed.

Chapter 6 A Finite Element Study of Rayleigh Wave Reflection from an Interface

In this chapter, finite element studies are performed to validate results obtained from the analytical model. This is performed using COMSOL Multiphysics, a finite element software package. The practicalities of setting up a and simulating a model is detailed. The methods employed in extracting and analysing data from the simulations are described with the use of a sample simulation.

Chapter 7 Experimental Measurement of Rayleigh Wave Reflections

Here, Rayleigh wave reflection from a contact interface is studied experimentally. The experimental layout is first described followed by the type of tests that are to be performed. The loading methods are described next. Then, ultrasonic instrumentation procedures are detailed followed by a description of the methodology involved in the collection and subsequent processing of the experimental data. The experimental results are then compared to results from Chapters 5 and 6 and discussed.

Chapter 8 Application to Condition Monitoring of Lip Seals

The potential of Rayleigh wave as a condition monitoring tool is explored in this chapter by conducting pilot studies in applying Rayleigh wave to condition monitor a lip seal.

2 Background of Ultrasonic Techniques

This chapter first details the physics of elastic waves at ultrasonic frequencies. This is followed by a look at some of the most common applications of ultrasonic waves. The problems of applying conventional ultrasonic methods to tribology applications are highlighted, followed by a review on the development of novel methods to apply ultrasound in tribology.

2.1 Introduction

A wave, in its most general definition simply means an oscillating motion that propagates through space. Two broad categories of waves exist – mechanical waves which requires a medium through which the wave can propagate through and electromagnetic waves which does not require a medium but instead relies on the oscillation of electrical and magnetic fields.

The rate at which a wave oscillates is known as its frequency. In general, frequencies are further categorized into either infrasound, acoustic or ultrasonic frequencies. Infrasound waves have frequencies below 20Hz. Mechanical waves in the range of 20Hz to 20kHz lie in the audible range. These are the sounds that humans can detect with their ears. Ultrasonic waves are generally waves with a frequency higher than 20kHz.

The work conducted here involves the use of ultrasonic mechanical waves.

2.2 Ultrasonic Physics

Ultrasonic waves are harmonic waves that vibrate at a frequency that is above the hearing range of the average person (20kHz). Since the research here involves using ultrasonic mechanical waves, it is important to first discuss some aspects of the relevant physics that will help shape a better understanding of this physical phenomenon.

Mechanical waves travel through a medium via the energy transfer between particles of a medium. Fig. 2.1 illustrates how this process takes place. An external stimulus locally excites a region of the medium. This local distortion then propagates through the medium via the restoring forces of neighbouring particles owing to the inherent elasticity of the medium, causing alternating regions of compression and dilation. It should be noted that no permanent deformation takes place in any part of the medium since the distortions are small.

There exist many different ways in which the oscillating motion can occur and for each unique type of oscillating motion, a unique wave mode is identified. However, a broad

classification can be ascribed based on the most common types of oscillation. They are longitudinal waves, transverse waves, surface waves and guided waves.

When the oscillations are parallel to the direction of propagation (Fig. 2.1), they are known as longitudinal waves. When the oscillations are perpendicular to the direction of propagation (Fig. 2.2), they are known as transverse waves. Both longitudinal and transverse waves are collectively known as bulk waves since they propagate through the bulk of a medium. Guided waves are waves that are guided along the geometry in which it propagates e.g. Lamb waves propagating in plates of different shapes.
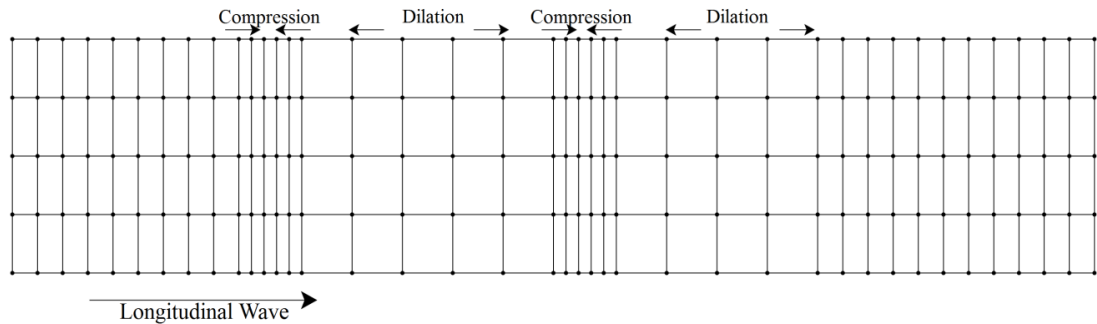
Fig. 2.1 Longitudinal Wave Motion
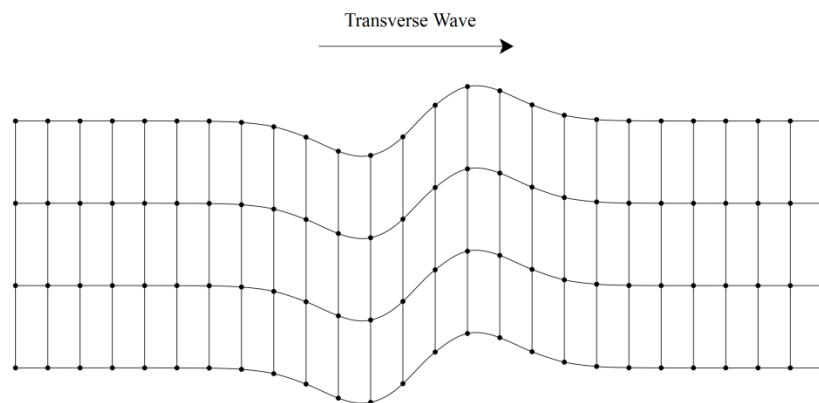
Fig. 2.2 Transverse wave motion

Surface waves on the other hand, propagate only on the surface of a material. The oscillations of surface waves can vary greatly and therefore, there exist different types of surface waves. A separate chapter is dedicated towards surface waves as it is this form of mechanical waves that is used in this study.

2.3 Common Applications of Ultrasonic Waves

The main way by which ultrasonic waves are generated is through the phenomena known as piezoelectricity whereby an electrical charge is generated in a piezoelectric material when it is subject to a mechanical stress. This effect also occurs in reverse i.e. an electric charge generates a change in dimension of the piezoelectric material. Materials that demonstrate this effect are known as piezoelectric materials.

Applications of ultrasonic waves are wide and varied. They include medical ultrasound (foetal imaging), deep sea sonars and condition monitoring applications to detect flaws and cracks. They all function based upon useful properties of ultrasonic waves that can be taken advantage of.

Many ultrasonic based applications depend on what is known as the TOF (Time of Flight) method. The basic premise is that the time of transit of an ultrasonic wave is measured as it travels through a medium. The time of transit can be used to obtain the speed of sound through a material if the distance travelled is known. The speed of sound can then be used to identify an unknown material since it is an intrinsic property of the material.

The ability to reflect from an interface is another useful property of ultrasonic waves. The reflection occurs as the ultrasonic pulse travels through an interface that is acoustically mismatched. An interface is said to be acoustically mismatched when the material on both sides of the interface has differing acoustic impedances given by

$$z = \rho c \tag{2.1}$$

Where ρ is the density of the material and c is the speed of sound in the material. By utilizing ultrasonic reflection, the sensors that are used in ultrasonic applications can be reduced to a single sensor operating in pulse-echo mode i.e. it simultaneously sends and receives the ultrasonic pulse. This reduces costs and in many applications, is the only feasible way of operating the sensors.
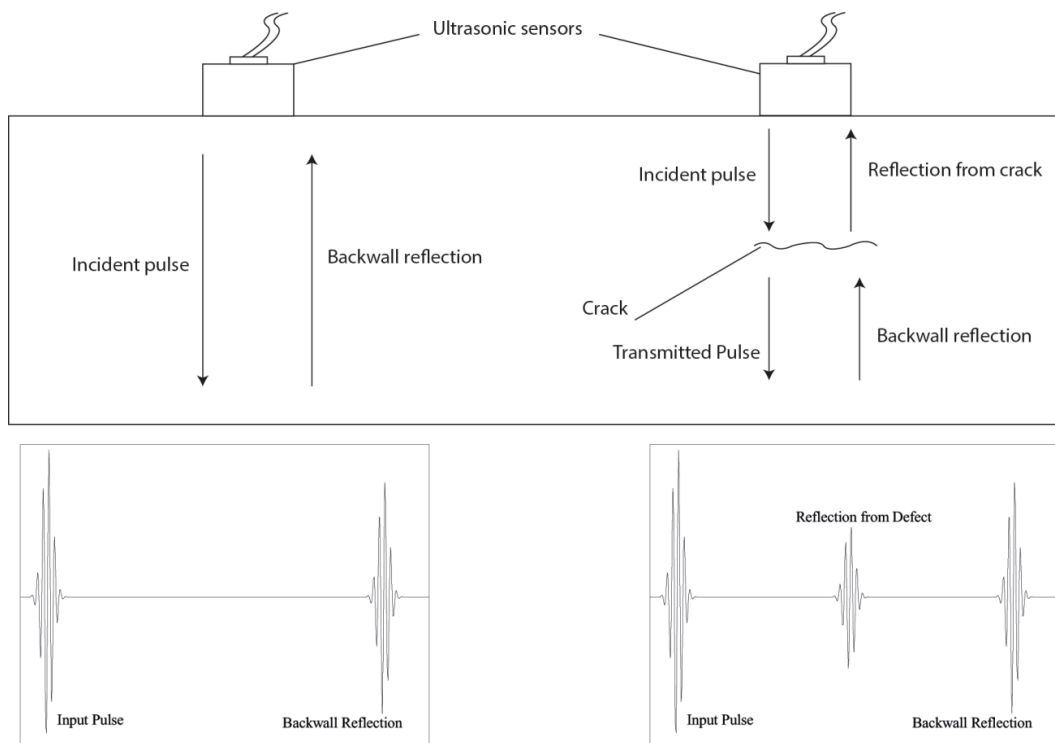
Fig. 2.3 Ultrasonic detection of cracks

Cracks and flaws in a medium can be detected via ultrasonic reflection, the concept of which is shown in Fig. 2.3. The cracks create and impedance mismatch in the material which creates a reflector embedded within the medium. As the sensor is passed along a segment of a material which contains the crack, additional reflections are detected.

A common application that arises out of a combination of TOF and ultrasonic reflection is distance measurements where an ultrasonic pulse is sent to an interface at which it is reflected. The TOF is measured and the distance between the sensor and the interface can be gauged as long as the speed of the wave through the medium is known.

Applications of ultrasound in tribology require a different approach. This is because in tribology, what is of interest is the nature of how the surfaces interact and this usually takes place at a scale that is too small for conventional ultrasonic methods to be useful. To illustrate, Fig. 2.4 shows the difficulties encountered as an increasingly thin oil film is being measured using longitudinal waves normally incident on the interface. Initially, while the film is still thick, reflections from interface A and B are discrete and hence distinguishable from one another. As the film becomes thinner, the pulses begin to merge. At a certain point, as the oil film becomes thinner, the discrete pulses reflecting from the front and back of the oil film overlaps, making thickness measurement via the TOF method impossible.
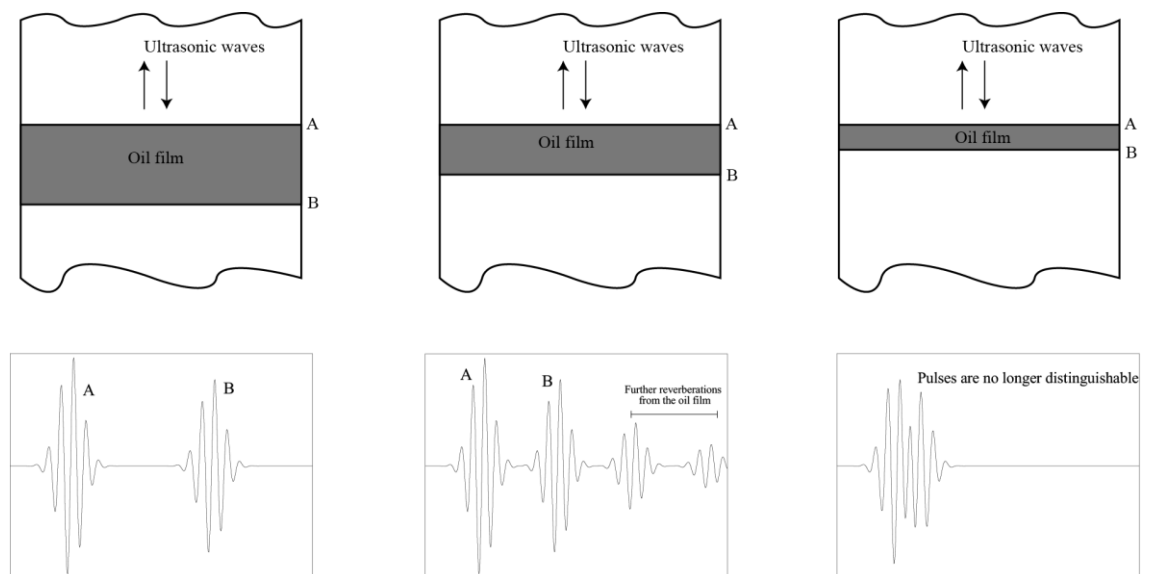
Fig. 2.4 Merging of ultrasonic pulses in a thinning layer

Specific methods have been developed in order to analyse tribological applications via the use of ultrasound. They rely on the ability to extract information from the reflected pulses regarding the contact interface. The next section discusses in further depth the development of these techniques and how they are applied in tribology.

2.4 Ultrasonic Applications in Tribology

When an ultrasonic pulse is sent to an interface, there will be scattering at the interface. As a result, both reflected and transmitted waves are produced and in certain cases, new wave modes are also generated. Since the nature of the scattering depends on properties at the interface, a way of probing interface properties presents itself through the analysis of the scattered waves.

Incident Wave

Transmitted Wave

Reflected Wave

Medium 1 | Medium 2
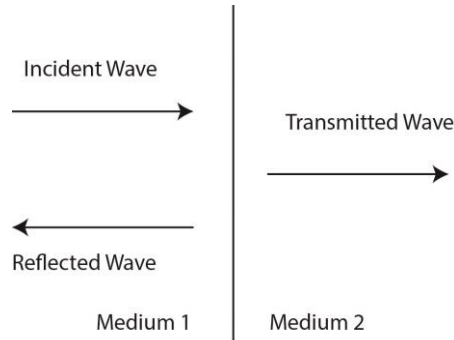
Fig. 2.5 Ultrasonic reflection from a perfect interface

For a perfect interface (Fig. 2.5), the governing equations have been derived using conventional ultrasonic theory and are given by the simple relationships below for a normally incident longitudinal wave

$$1 = T + R \tag{2.2}$$

$$R = \frac{z_1 - z_2}{z_1 + z_2} \tag{2.3}$$

Where T and R represents the displacement transmission and reflection coefficient and the subscripts in z denotes the medium to which it is attributed to.

Changes in the acoustic impedances, z_1 and z_2 cause part of the incident wave to be reflected. The greater the mismatch (the difference between z_1 and z_2), the greater the reflection.

All surfaces are to a certain degree, rough. Under magnification, all real surfaces are formed by a collection of surface asperities. When two surfaces come into contact, it is the asperities that come into contact. The rougher the surface, the more the interface deviates from a perfect contact assumption. As a result, equation (2.3) becomes increasingly erroneous as the contact interface strays away from its idealisations.

The seminal work by Kendall and Tabor (1971) attempted to evaluate how ultrasound passing through an incomplete interface would behave. Their studies related ultrasound transmission through the interface with the stiffness of the interface by pressing soft solder discs in between steel bars. The amount of solder disc as well as the spacing between the solder were changed to study how the different configurations changes the

stiffness. Ultrasonic transmissions through the interface were measured. In this way, Kendall and Tabor showed that the transmitted ultrasonic wave increases with an increase in the stiffness of contacts.

A natural progression from the stiffness concept is to represent the imperfect interface as springs in what is now known as the Spring Model (Fig. 2.6). This representation was first introduced by Tattersall (1973) to represent an interface with a layer of adhesive sandwiched in between. This was then extended to rough surfaces in contact by Drinkwater et al (1996) where stiffness measurements using ultrasonic techniques were obtained by applying a cyclic loading on an aluminium disc against a plate made out of the same material. The results (Fig. 2.7) are compared to existing theoretical models whereby agreement to within an order of magnitude was obtained. The differences were attributed to idealisations of the analytical models.
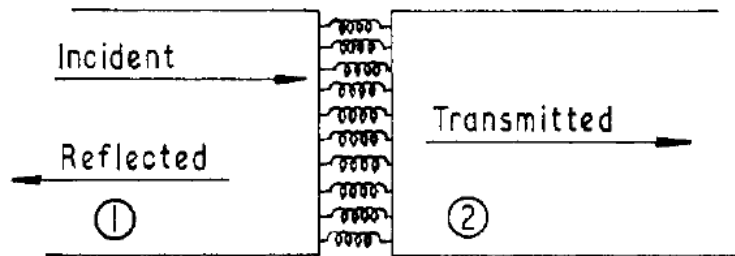
Fig. 2.6 The Spring Model (Tattersall 1973)

The concept of ultrasound being related to the stiffness of an interface is extended by Królikowski and Szczepek (1993) to include tangential stiffness. It was found that the ultrasonic prediction of both normal and tangential stiffness can be described by the Hertz-Mindlin theory whereby both stiffness are in proportion to each other. The results obtained here are further corroborated in experimental studies by Baltazar et al (2002), Biwa et al (2005) and Gonzalez et al (2010).
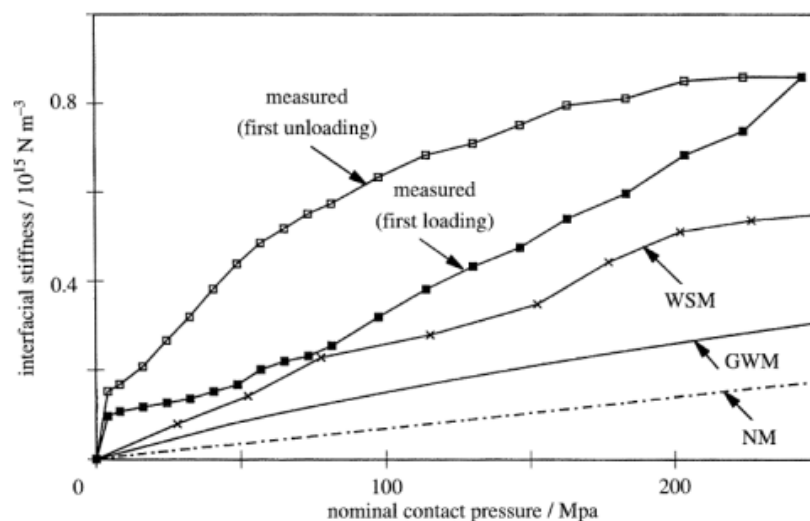
Fig. 2.7 Stiffness measurements of rough surfaces in contact under cyclic loading (Drinkwater et al. 1996)

Dwyer-Joyce et al (2003) applied the spring model to measurements of thin film layers in between an interface by using expression of stiffness for a thin liquid layer. In the study, experiments were conducted on both static and dynamic lubricant films (ball on flat) and it is shown that the spring model applies very well in both cases (Fig. 2.8). Using this principle, thin film thickness have been successfully measured in applications such as journal bearings (Dwyer-Joyce et al. 2004), rolling bearings (Drinkwater et al. 2009), piston rings (Avan et al. 2010; Mills et al. 2013) and mechanical seals (Reddyhoff et al. 2008). Section 2.4.1 explores the Spring Model in detail.

(a)

(b)
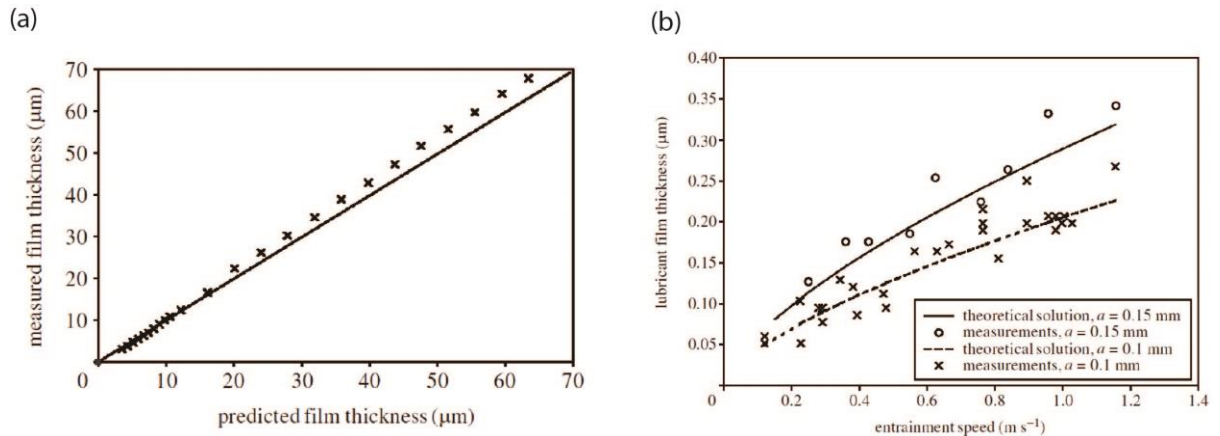
Fig. 2.8 Film thickness measurements using the Spring model (Dwyer-Joyce et al. 2003). (a) Results for a static film in the shape of a liquid wedge, (b) Results for a dynamic film formed using a steel ball sliding on glass.

An alternate approach of looking at an interface with a thin film is by looking at how ultrasound reflects from a multilayer system with an embedded layer of finite thickness, h. The interfaces connecting each layer are assumed to have continuity of both stresses and strain and are sometimes also known as the Continuum Model, illustrated in Fig. 2.9
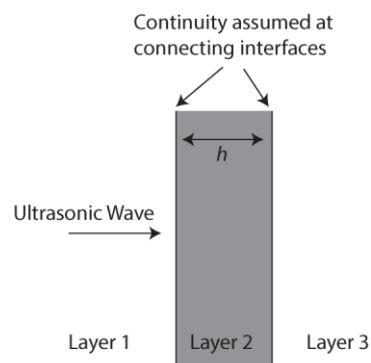
Fig. 2.9 A multilayer system representation for the Continuum Model

The normal incidence reflection coefficient for such a system has been developed analytically by Krautkramer (1969). For a layer of liquid sandwiched between two identical media:

$$|R|^2 = \frac{(\frac{z}{z_o} - \frac{z_o}{z})^2 \sin^2 \frac{2\pi f h}{c_o}}{4 + (\frac{z}{z_o} - \frac{z_o}{z})^2 \sin^2 \frac{2\pi f h}{c_o}} \qquad (2.4)$$

Where c_o and z_o are the speed of sound and acoustic impedance of the intermediate layer and f is the frequency of the wave.

Plots for equation (2.4) at various h is shown in Fig. 2.10. It can be seen that at higher frequencies, the appearances of sharp minima at regular intervals can be observed. This occurs due to destructive interference of the waves bouncing back and forth within the layer.

The intervals at which the 'dips' occur are dependent on h and is given by Pialucha and Cawley (1994) to be (note that this assumes that there exists a large enough impedance mismatch between layers 1 and 2 to cause reflections to occur):

$$f_i = \frac{c_o}{2h} \qquad (2.5)$$

Thus, the film thickness of an interface can also be determined by via detection of these 'dips'. At least two successive dips has to be detected to determine the interval between them which can then be converted to film thickness via equation (2.5)

It will be shown in section 2.4.1 that equation (2.4) can be reduced to obtain the spring model for the case of a liquid film. This shows that the continuum model is in fact a generalized form of the Spring Model.
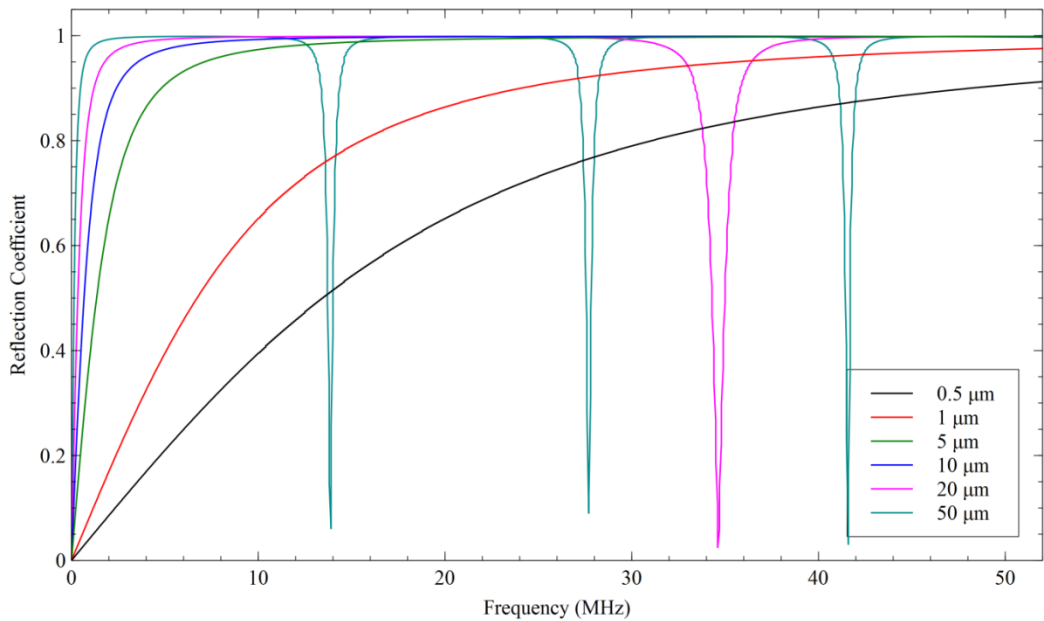
Fig. 2.10 Reflection coefficients from an interface with varying oil film thickness calculated using the continuum model.

2.4.1 Ultrasound Theory

The Spring Model

Equation (2.3) gives the reflection coefficient from a perfect interface. In practice, the interface deviates from the ideal case either through the presence of roughness or via a thin layer of foreign material (adhesives, lubricant etc). This deviation changes the way the interface responds to an incident pulse.

As alluded to in the previous section, Tattersall first approached the problem of an imperfect interface by modelling the interface as springs (Fig. 2.6). The reflection coefficient of the interface was related to the stiffness of the springs, K through equation (2.6).

$$|R| = \sqrt{\frac{(\omega z_1 z_2)^2 + K^2(z_1 - z_2)^2}{(\omega z_1 z_2)^2 + K^2(z_1 + z_2)^2}} \qquad (2.6)$$

Here, ω represents the angular frequency. If the materials on both sides of the interface are the same, $z_1 = z_2$, equation (2.6) can then be reduced to

$$|R| = \frac{1}{\sqrt{1 + \left(\frac{2K}{\omega z}\right)^2}} \qquad (2.7)$$

The spring model is applicable to both lubricated and dry contact scenarios so long as the correct expression for stiffness, K is used. In the case of a dry contact, the stiffness per unit area is generally defined as:

$$K_{dry} = \frac{dp_{nom}}{du} \qquad (2.8)$$

Where p is the nominal pressure and u is the approach of the surfaces.

Exact expressions for (2.8) are dependent on theories developed in the field of contact mechanics (e.g. Greenwood & Williamson 1966).

When a layer of oil is present at the interface, the stiffness takes the form of (Dwyer-Joyce et al. 2003):

$$K_{lubricated} = \frac{\rho c^2}{h} \qquad (2.9)$$

By substituting (2.9) into (2.7), the reflection coefficient for a lubricated contact is given by:

$$R = \cfrac{1}{\sqrt{1 + \left(\dfrac{2\rho c^2}{h\omega z}\right)^2}}$$

(2.10)

By rearranging for h, we obtain

$$h = \frac{2\rho c^2}{\omega z} \sqrt{\frac{R^2}{1 - R^2}}$$

(2.11)

Thus, the film thickness can be determined based on the reflection coefficient of the interface.

Reduction from the continuum model

Originally, the Spring Model was developed primarily based on the work of Tattersall (1973). It can be shown that the model is in fact a reduction of the continuum model equation given by Krautkramer for the case of a lubricated contact. The thickness of an oil film is usually small compared to the wavelength, thus if we assume that $h \ll \frac{c_o}{f}$, then, utilizing small angle approximations equation (2.4) then becomes:

$$|R|^2 = \frac{(\frac{z}{z_o} - \frac{z_o}{z})^2 \left(\frac{2\pi f h}{c_o}\right)^2}{4 + \left(\frac{z}{z_o} - \frac{z_o}{z}\right)^2 \left(\frac{2\pi f h}{c_o}\right)^2}$$

(2.12)

In most practical applications, the acoustic impedance of the solid space is generally several orders of magnitudes higher than the acoustic impedance of the lubricating layer. For this reason, we assume $z \gg z_o$ through which (2.12) reduces to

$$|R|^2 = \frac{1}{1 + \left(\dfrac{2c_o z_o}{z\omega h}\right)^2}$$

(2.13)

Which is identical to (2.10). Thus the continuum model can be viewed as the general case to the spring model without limitations of the preceding assumptions but at the cost of a more complex expression.

2.5 Practical Aspects of Ultrasonic Applications in Tribology

An ultrasonic wave is generated when an electrical input at ultrasonic frequencies is applied to a piezoelectric material. The piezoelectric material converts the electrical energy into mechanical vibrations via the piezoelectric effect. This causes the material to vibrate at the input frequencies. The vibrations are transferred to a different medium via solid contact. Used in this way, the piezoelectric material is termed a generator.

Because the piezoelectric effect works both ways, piezoelectric materials are also capable of capturing ultrasonic signals through vibrations imposed onto the piezoelectric material from the ultrasonic pulse which then generates an electrical charge.

The piezoelectric material, usually some variant of lead zirconium titanate also known as PZT is the main component of an ultrasonic transducer. The structure of a common commercial transducer is shown in Fig. 2.11. Features such as the damping plate and electronic tuning are added to produce a better conditioned pulse. The delicate electronics are then potted in epoxy and encased in a rugged casing for increased robustness.
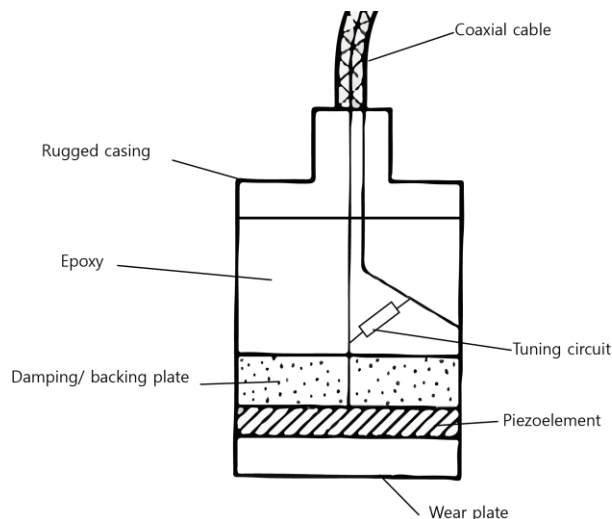
Fig. 2.11 Cross-section of a commercial transducer (Hull & John 1988)

Since air is a weak carrier of ultrasonic waves, in order for transmission to occur from a transducer to the work piece, a couplant is needed to eliminate the air gaps and bridge the transducer to the work piece. The couplants are usually in the form of a viscous fluid.

An alternative to using commercial transducers is to directly bond the piezoelectric element (Fig. 2.12) onto the work piece. The bonding is achieved by using adhesive glue (cyanoacrylate). The adhesive doubles as a couplant between the piezoelectric element and the work piece. Wires are soldered directly onto the piezoelectric element which can then be encased in epoxy to protect the soldered terminals and the piezoelectric element.
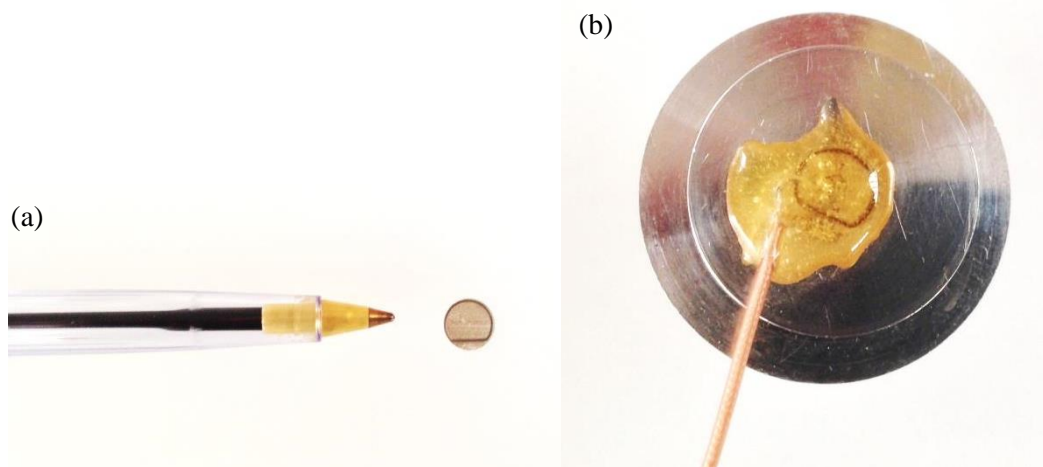
Fig. 2.12 Piezoelectric elements (a) Size comparison with a pen, (b) Bonded directly onto the surface in various form of applications.

The main advantage that is brought by using the bare elements is the greatly reduced costs. The piezoelectric elements can cost as little as £1 each compared to commercial transducers which are normally in the range of £100 upwards. This allows the piezoelectric elements to be used as consumables whereby it can be replaced easily if required since the cost of replacement is low.

Due to its smaller size, the piezoelectric element can be used in applications where space is tight. They can be permanently embedded into suitable applications without requiring much modification to the said application to accommodate them. Therefore, they are particularly suitable to be used as an online monitoring device whereby an interface can continuously be probed without affecting the original ecosystem of the application of which the elements are applied to.

A downside of using the bare elements is that the user has to have proper training in handling the installation and pre-testing of the bare piezoelectric elements in addition to existing knowledge of interpreting conventional ultrasound data. This is particularly true given that the elements are fragile materials and can easily fracture without proper handling.

The selection of the frequencies is an important caveat. This is limited, in part by the cost of a transducer at a specified frequency and the capability of a manufacturer to produce them. Off the shelf transducers and piezo-elements are always cheaper than built to order items. The other limiting factor is that as frequencies are increased, the thickness of the PZT decreases. This adds cost and reduces reliability of the PZT so it is usually desirable to keep the frequencies at nominal ranges.

Another factor in deciding the frequencies is to consider the response of the interface to the ultrasonic wave. This can be done by referencing the continuum model plots (Fig. 2.10). At a low frequency (assuming 2MHz), the film thickness can be easily distinguished based on the magnitude of the reflection coefficient. As frequency increase, the curves tend asymptotically to unity. At higher frequencies (say 20 MHz), curves for thicker films overlap, thus making it impossible to distinguish them based on the reflection coefficient. This is also true for thinner films provided that the frequencies are further increased.

Whilst it may seem beneficial to then use low frequency transducers to allow for measurement of larger film thickness, this option has to be considered carefully. The first issue is that as the frequency of the transducer reduces, the reflection coefficient rapidly drops to a point that the reflected pulse is too weak to be detected by the transducer.

Another consideration is the physical size of the work piece being tested. Lower frequency waves have larger wavelengths, increasing the size of the pulse train. This causes an issue in applications with thin cross sections as the low frequency transducers will still be pulsing when the reflected waves returns. This causes the reflected waves to be masked by the pulsing of the transducer.

Therefore, selecting the right ultrasonic probe (either conventional or bare elements) at the right frequency is not a straightforward matter and requires full consideration of the available space and size of the application as well as the ultrasonic response at the measured interface.

2.6 Conclusions

The basic workings of ultrasonic waves have been discussed. Useful properties of ultrasound have been highlighted and their applications demonstrated through some common applications.

Application of the ultrasonic method in tribology requires novel methods. This comes in the form of representing contact interfaces as interconnecting springs. This is also known as the spring model. A separate approach, known as the continuum model is also discussed. It is shown that both methods converge and that the spring model can be deduced from the continuum model.

Also discussed are completed studies applying the spring model in tribological applications. Lubricant film thickness and contact stiffness of an interface have been measured successfully.

Finally, the practicalities of using ultrasound in tribology are discussed. Conventional means of generating ultrasonic waves is through the use of commercial transducer. However, great savings can be attained if the bare piezoelectric elements are used instead. Selecting the right frequencies of the ultrasonic probes requires careful consideration of the intended application.

3 Background of Rayleigh Waves

In this chapter, the background of Rayleigh waves is detailed. First, a brief introduction covering the essential physical nature of Rayleigh waves is given. This is then followed by an explanation of the various generation methods available to generate Rayleigh waves. The practicalities of using Rayleigh wave are discussed next, with the chapter closing with a final section discussing the various applications of Rayleigh waves.

3.1 Introduction

In contrast to bulk waves, surface waves propagate on the boundaries of a material instead of through the body of the material (Fig. 3.1). Different types of surface waves can exist. Of interest in the study undertaken here is that of Rayleigh waves, first proven to exist by Lord Rayleigh in 1885 (Rayleigh 1885) through analytical means.
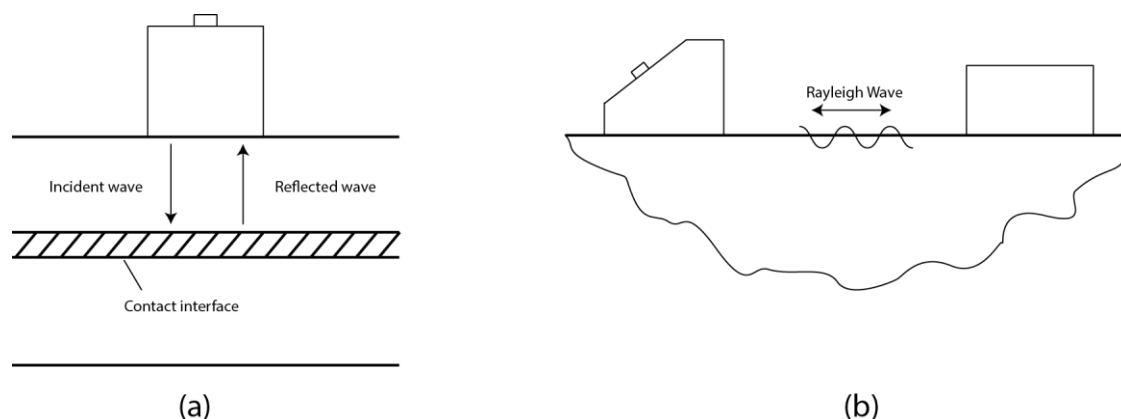
Fig. 3.1 Different wave types (a) Bulk waves and (b) Rayleigh waves

Rayleigh waves exists at a wide range of frequencies, with the lower end frequencies being that of seismic wave frequencies (order of magnitude of one Hertz) and the higher end at the GHz region, commonly found in telecommunication sensors. The frequency range for surface waves is illustrated in Fig. 3.2.

Most of the energy from Rayleigh waves is confined to only about one wavelength from the surface and for this reason; it is usually used to probe surface and near-surface phenomenon.
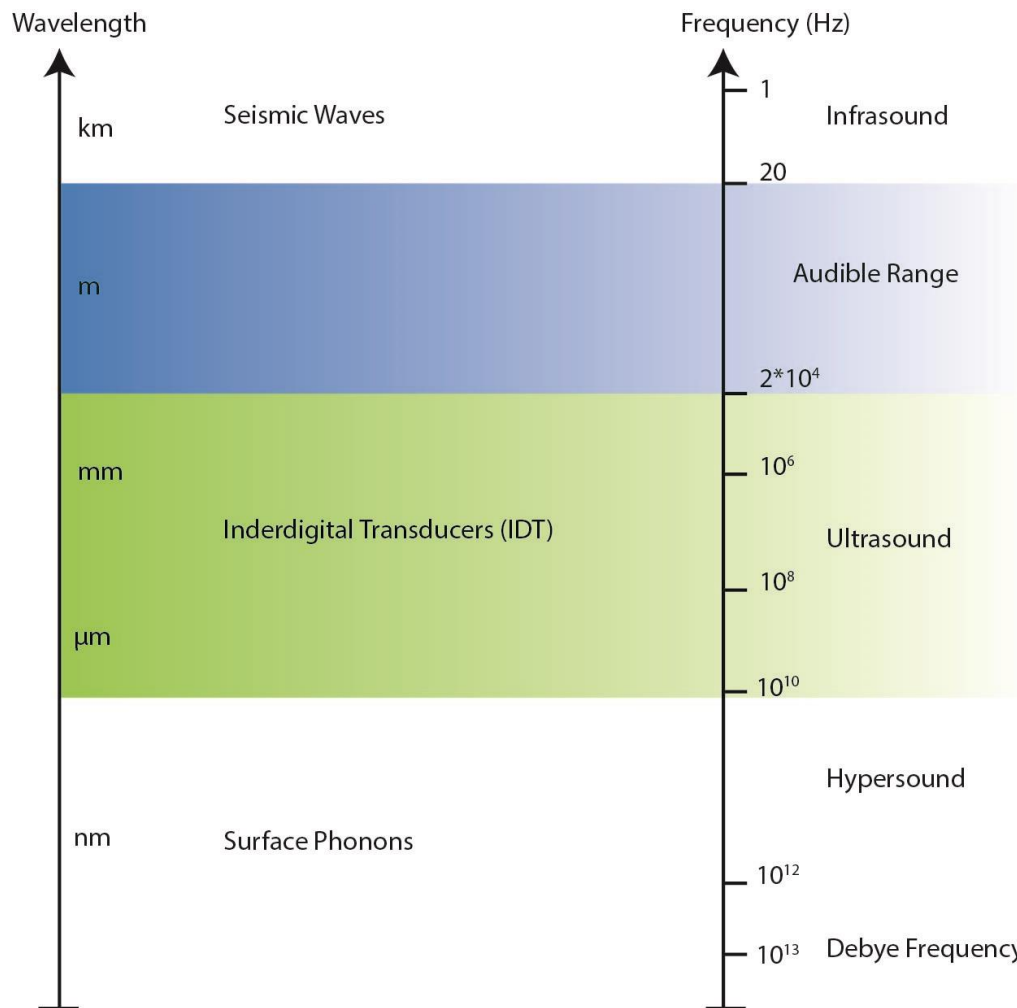
Fig. 3.2 Frequency range of surface waves that are known to exist. (Diagram reproduced from (Hess 2002))

Before further discussions are made on Rayleigh waves, it is necessary to first be exact in the definition of Rayleigh waves in this thesis. They are listed below:

- Rayleigh wave exists on the free boundary of a solid medium. That is to say that the medium bordering the solid is that of vacuum. A relaxation to this rule can be made to include atmospheric gas if the density of the atmosphere are orders of magnitude smaller than the solid medium.
- The solid medium is an elastic isotropic medium
- The medium is that of a half space i.e. it has infinite depth. In practice all material has finite dimensions. This issue is further addressed in section 3.5 of this chapter.

The mechanism through which Rayleigh waves propagate along the surface of a medium is the same as conventional ultrasonic waves. Propagation occurs due to the elastic restoring forces of the medium.

Fig. 3.3a shows the deformed state of a material as Rayleigh wave travels through it. The motion of Rayleigh waves through a material can be viewed as a combination of both longitudinal and transverse motions, hence causing the particles to vibrate in an elliptical motion as Rayleigh wave passes over the particles.
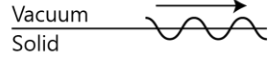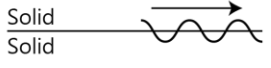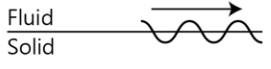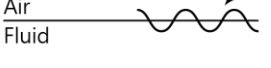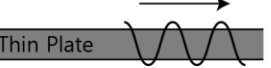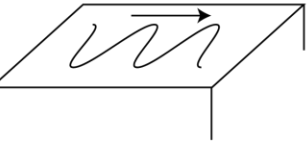
The energy of Rayleigh waves are contained near the surface at which it propagates. This extends to a depth of around one wavelength beneath the surface. This is illustrated in Fig. 3.3b where the displacements from Rayleigh wave motion drops exponentially from the surface.

(a)   (b)
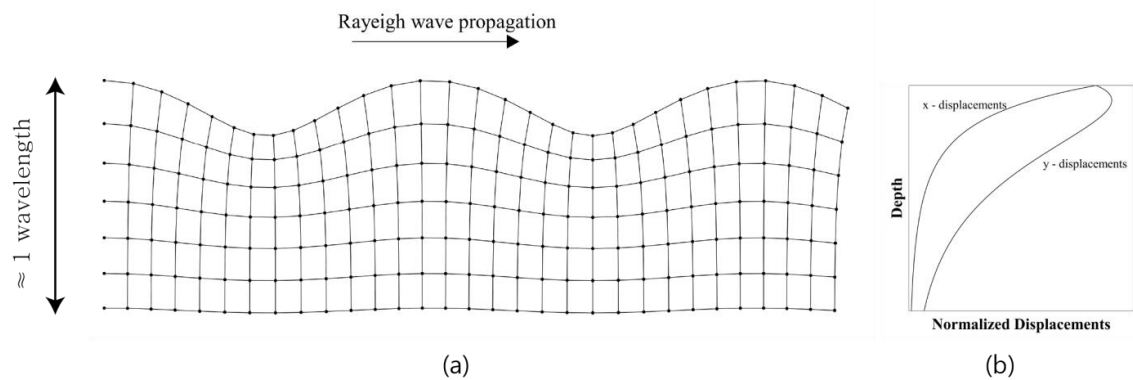
Fig. 3.3 (a) Elastic deformation caused by Rayleigh wave propagation (b) Decay of amplitude with increasing depth

While by no means an exhaustive list, Fig. 3.4 shows some of the most commonly encountered types of surface waves. In the section that follows, the term 'surface waves' shall refer to the general class of waves that has its energy localized near the surface of a material while the term 'Rayleigh waves' refers to the type of waves that fulfil the definition outlined in the bullet points above.

Emphasis is placed on the distinction between the two terms to avoid confusion since they have been used interchangeably in literature.

Type of surface and guided wave	Illustration	Description
Rayleigh wave SAW (Surface Acoustic Wave)	Vacuum / Solid	A mode of surface wave that travels along a solid bordering a vacuum. Although both Rayleigh and SAW terms have been interchangebly used, usage of Rayleigh waves are more common in seismology while SAW terms are more common in the field of electronics e.g. interdigital transducers and resonant devices.
Stoneley wave	Solid / Solid	A type of interface wave that travels along the interface of two solids.
Scholte wave	Fluid / Solid	A type of interface wave that travels along a fluid-solid interface
Water/ gravity waves	Air / Fluid	A wave mode that travels along the surface of a fluid medium
Lamb waves	Thin Plate	Lamb waves exist in thin plates and have two distinct modes - symmetric and antisymmetric and are dispersive.
Love waves		Love waves are horizontally polarized surface waves that travels along the surface of a solid medium

Fig. 3.4 Different modes of surface and guided waves

3.2 Rayleigh Wave Generation

There are several ways by which Rayleigh waves can be generated. Viktorov (1967) gives an extensive list into the methods through which Rayleigh waves are generated. The simplest case is shown in Fig. 3.5b whereby a piezoelectric element bonded onto the surface of a material generates Rayleigh waves in addition to bulk waves. This is analogous to the phenomena of ripples forming on the surface of a pond as a disturbance is introduced at a point (e.g. throwing a pebble into a calm pond).
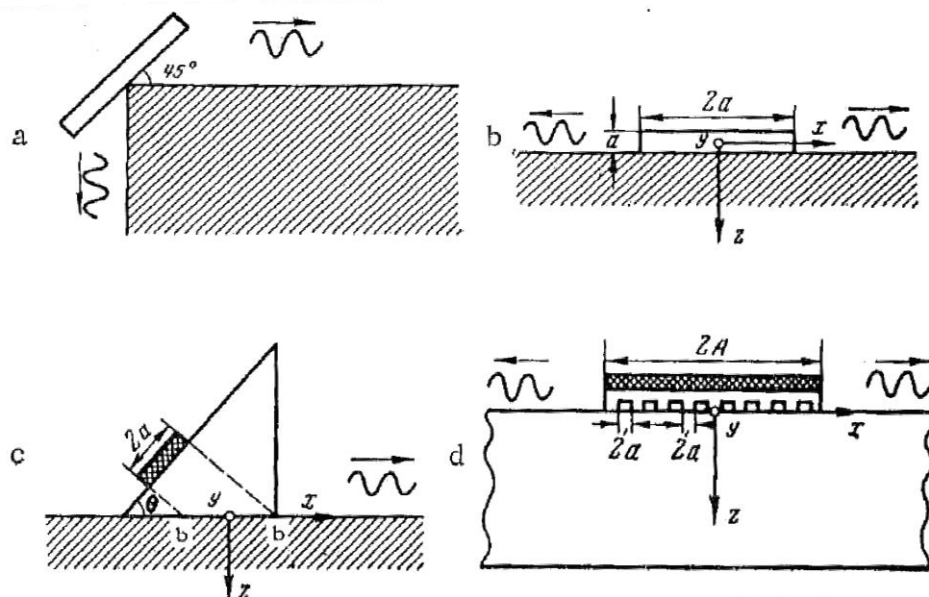
Fig. 3.5 Different methods of generating surface waves (Viktorov 1967) (a) X-cut quartz plate (b) Y-cut quartz plate (c) Angled wedge method (d) Using 'comb-like' structure with and X-cut crystal resting on top

Efficiency of the Rayleigh wave generation can be improved by introducing a comb-like structure (Fig. 3.5d) between the piezoelectric elements and the surface. Maximum efficiency is achieved when the spatial period is the same length as the wavelength of the Rayleigh wave.

The most common way by which Rayleigh waves are generated, and a method that is widely used in the area of flaw detection is the use of an angled wedge to generate Rayleigh waves Fig. 3.5c. The main advantage of this method is that waves can be generated in a preferred direction. In addition, lesser bulk waves are generated, eliminating spurious signals which can lead to confusion when interpreting data. In terms of efficiency, the wedge method has about half the efficiency of Rayleigh wave generation by using metallic gratings (Viktorov 1967).

Aside from the methods described above, Rayleigh waves can also be generated using contactless methods. One of the ways is by using lasers which generates the movement of the wave through localized thermoelastic expansion on the surface caused by heating from the lasers (Royer & Chenu 2000; Murfin et al. 2000).

EMATs (Electromagnetic transducers), shown in Fig. 3.6 are widely used to generate ultrasonic waves without requiring contact with the surface of the material. By using a magnet together with an electric coil connected to a circuit, different types of ultrasonic waves can be generated depending on the design of the coil. Thus with the right coil design, Rayleigh waves can be generated using EMATs (Dixon & Palmer 2004).
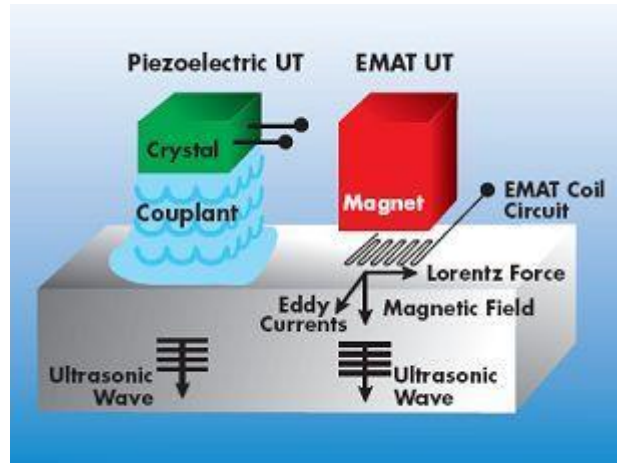
Fig. 3.6 Schematic of an electromagnetic transducer (Innerspec n.d.)

For the experiments conducted throughout this study, the wedge method was chosen due to its simplicity and ease of setting up. A thorough explanation of the method is given in the next section.

Rayleigh Wave generation using an angled wedge

This method works on the principle that when a wave hits an interface at an angle other 90°, refraction (i.e. change in travel path) of the wave takes place. This phenomenon can be conveniently summarized by Snell's Law (illustrated in Fig. 3.7a) which states:

$$\frac{\sin \theta_1}{\sin \theta_2} = \frac{c_{l1}}{c_2} \qquad\qquad (3.1)$$

Where c_{l1} is the longitudinal wave velocity in medium 1 and c_2 can either be the longitudinal or shear wave velocity in medium 2.

——— Bulk longitudinal wave generation
——— 1st critical angle
——— Bulk shear wave generation
——— 2nd critical angle
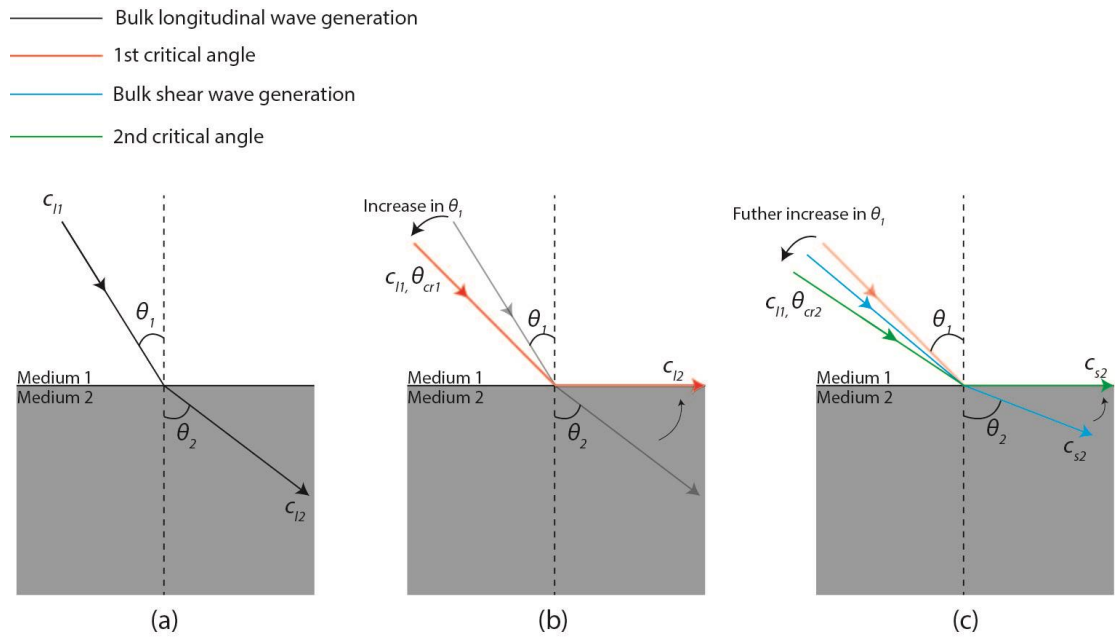
Fig. 3.7 Rayleigh wave generation using angled incidence (a) Generating only longitudinal bulk waves (b) 1st critical angle (c) 2nd critical angle

As the angle θ_1 is continuously increased (Fig. 3.7b), θ_2 increases until it reaches 90°, i.e. parallel to the surface. The angle of θ_1 that causes this to happen is termed the first critical angle, θ_{cr1}. Further increasing θ_1 (Fig. 3.7c) will result in the generation of shear waves (c_{s2}) in medium 2 while the longitudinal waves are fully reflected (i.e. total internal reflection).

In the same way as before, the second critical angle, θ_{cr2} is reached as θ_1 continues to increase (Fig. 3.7c). When this happens, the shear waves are refracted parallel to the interface. A further increase of θ_1 past θ_{cr2} will generate Rayleigh waves at the Rayleigh angle, θ_R travelling at the Rayleigh wave velocity, c_r. The critical angles and the Rayleigh angle can be described using the equations below:

$$\theta_{cr1} = \sin^{-1}\frac{c_{l1}}{c_{l2}} \tag{3.2}$$

$$\theta_{cr2} = \sin^{-1}\frac{c_{l1}}{c_{s2}} \tag{3.3}$$

$$\theta_R = \sin^{-1}\frac{c_{l1}}{c_R} \tag{3.4}$$

The relative amplitudes between the different wave modes as the angle of incidence is increased in shown in Fig. 3.8.

RELATIVE AMPLITUDE OF WAVE MODES
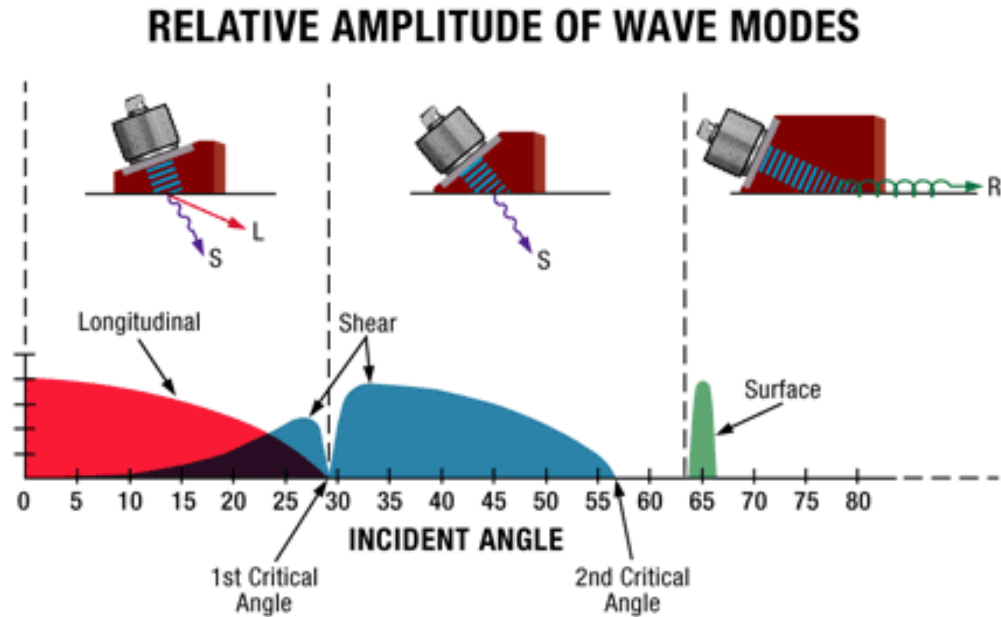
Fig. 3.8 Amplitudes of different wave modes as the incidence angle is increased
(Olympus n.d.)

In order to generate Rayleigh wave, the longitudinal and Rayleigh wave velocity in the medium must be known. Data for longitudinal waves in most common materials are readily available.

To obtain Rayleigh wave speed, an approximation based on the Poisson's ratio and shear wave speed of the solid through which the Rayleigh wave is travelling is used (Viktorov 1967):

$$c_R = \frac{0.87 + 1.12\nu}{1 + \nu} c_s \qquad (3.5)$$

Another caveat of (3.4) is that c_{l1} has to be smaller than c_R in order for Rayleigh waves to be generated. This restricts the range of suitable materials for the wedge. For this reason, the most commonly used material is that of Perspex where c_{l1} for Perspex is approximately 2720m/s, a quantity that is lower than c_R in common metallic materials such as steel or aluminium.

Table 3.1 summarizes the critical and Rayleigh angles for some common materials generated using a Perspex wedge. The material data are obtained from Onda (2003) and Callister and Rethwisch (2011). The Rayleigh wave speeds were calculated from (3.5).

Table 3.1 Critical angles for some common materials

	ν	c_l (m/s)	c_s (m/s)	c_R (m/s)	θ_{cr1}	θ_{cr2}	θ_R
Mild Steel	0.3	5900	3200	2969	26.26°	54.65°	61.53°
Aluminum	0.33	6420	3040	2833	24.15°	59.15°	67.11°
Brass	0.34	4700	2100	1960	33.73°	N/A	N/A
Copper	0.34	5010	2270	2119	31.40°	N/A	N/A

3.3 Properties of Rayleigh Waves

3.3.1 Attenuation Due to Absorption and Scattering

As ultrasonic waves travel through a medium, the energy of the waves are lost in the medium due to scattering and absorption within the medium, the degree of which is dependent on the material and the frequency of the travelling wave.

Attenuation is usually specified in terms of an attenuation factor, α (measured in nepers per unit distance) that quantifies the loss of amplitude in the equation below (McMaster 1959)

$$A_l = A_o e^{-\alpha l_t} \tag{3.6}$$

Where A_o is the initial amplitude of the wave and A_l is the amplitude of the wave after it has travelled a distance of l_t from where A_o is measured. α is commonly used to denote longitudinal wave attenuation coefficient. The equivalent for transverse waves and Rayleigh waves are β and γ respectively. Further, it is proposed by Viktorov (1967) that γ has a linear relation to both α and β and is given by

$$\gamma \lambda_R = \varsigma \alpha \lambda_l + (1 - \varsigma) \beta \lambda_s \tag{3.7}$$

Where ς is a dimensionless coefficient that depends only on the Poisson's ratio of the material and $\lambda_{R,l,s}$ are the wavelengths of the Rayleigh, longitudinal and shear waves. The expression for ς is rather cumbersome and hence is most conveniently expressed in graphical form shown in Fig. 3.9.
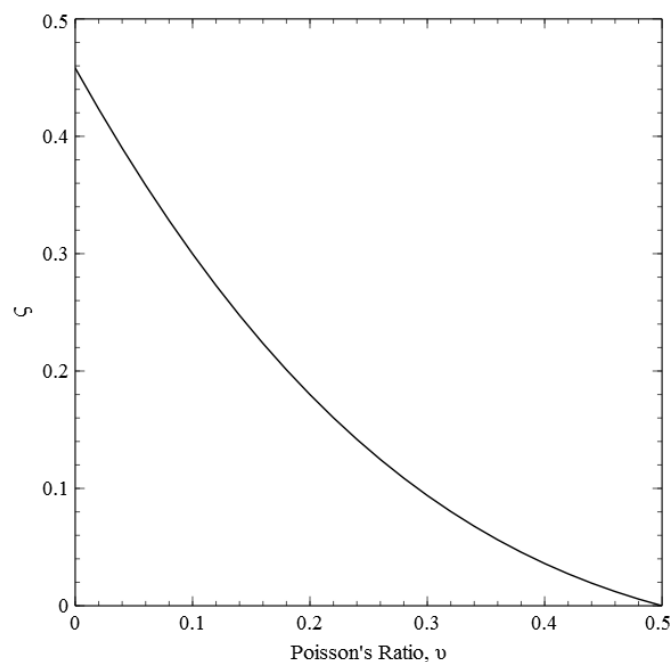
Fig. 3.9 Relationship between coefficient ς against Poisson's ratio v

Experiments performed by Viktrov on plexiglass samples using ultrasound ranging from 20 kHz to 180 kHz are in good agreement with (3.7). Thus, the attenuation of Rayleigh waves can be approximated through the attenuation coefficients of both longitudinal and transverse waves.

3.3.2 Attenuation Due to Geometric Spreading

Spreading is a phenomenon that happens when the wavefront of an ultrasonic wave diverges as it moves away from its source. This spreads the energy of the initial beam into a larger area, reducing energy density which results in an apparent energy loss.

The spreading of Rayleigh waves, quantified as a decay in amplitude with distance is given by Viktorov (1967) to be

$$Wave\ amplitude\ at\ distance, l_t\ from\ source = \frac{A_o}{\sqrt{k_R l_t}} \qquad (3.8)$$

Where k_R is the wavenumber of the Rayleigh wave.

3.4 Rayleigh Waves in Practice

Theoretically, Rayleigh waves are defined to exist only on an elastic half space. However in practice, no medium can possibly have infinite thickness. For a thin plate, Lamb waves are usually generated in the place of Rayleigh waves. Lamb wave is another type of surface wave. They are dispersive and have different modes of propagation depending on the thickness and wavelength of the waves. As the thickness of the plate increases, under the right conditions, the Lamb waves will behave like Rayleigh waves. For a given plate thickness and frequency, the plate can carry multiple modes of Lamb waves governed by the relationship given in equations (3.9) and (3.10) (Lamb 1917).

$$\frac{\tan\left(\frac{\beta d}{2}\right)}{\tan\left(\frac{\alpha d}{2}\right)} = -\frac{4\alpha\beta k^2}{(k^2 - \beta^2)^2} \text{ , Symmetrical or S mode} \qquad (3.9)$$

$$\frac{\tan\left(\frac{\beta d}{2}\right)}{\tan\left(\frac{\alpha d}{2}\right)} = -\frac{(k^2 - \beta^2)^2}{4\alpha\beta k^2} \text{ , Assymetrical or A mode} \qquad (3.10)$$

Where d is the thickness of the plate or substrate, $\beta = \sqrt{k_t^2 - k^2}$, $\alpha = \sqrt{k_l^2 - k^2}$, k_t and k_l are the wave numbers for tangential and longitudinal waves respectively and k is the wavenumber of the wave mode to be solved for by evaluating the roots of equations (3.9) and (3.10).

Fig. 3.10 is a typical Lamb wave dispersion curve showing the different wave modes that exists. Calculations were performed using parameters from Table 7.1. It can be seen that as thickness increases, the phase velocity of the modes A_o and S_o tends

asymptotically to the Rayleigh wave velocity, c_R. The rest of the modes generated tend to the shear wave velocity, c_s.
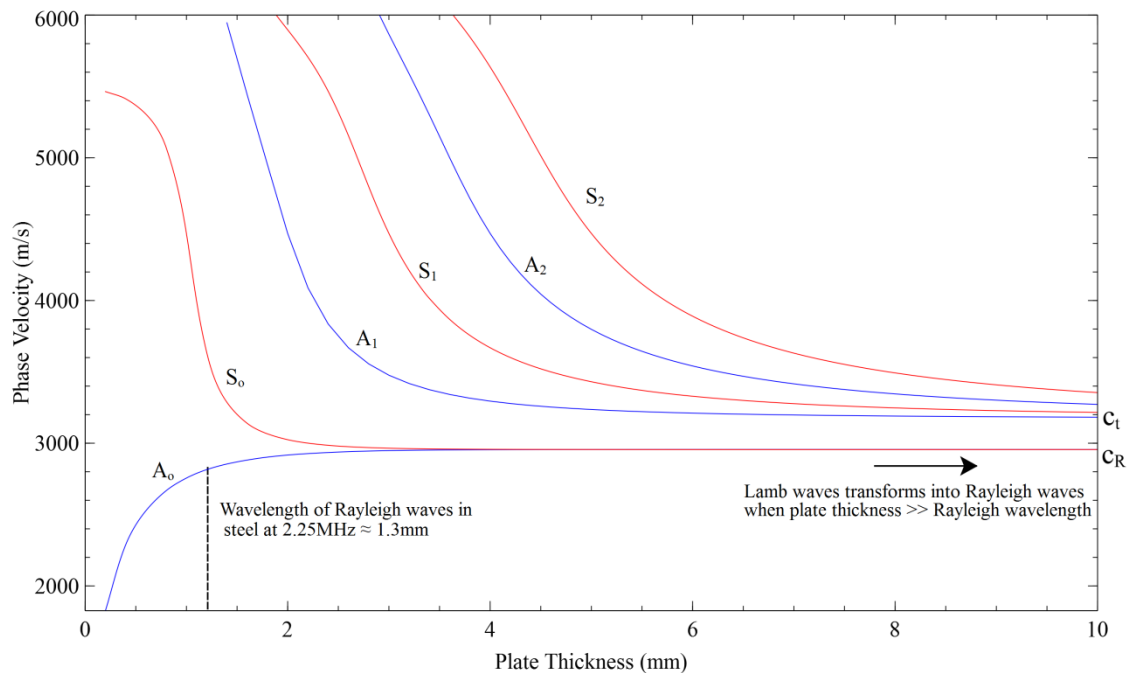
Fig. 3.10 Lamb wave dispersion curves for waves at 2.25MHz

Thus, in order to generate Rayleigh waves in finite dimension geometry, the first step is to determine the sufficient amount of thickness required to allow both A_o and S_o to transform into Rayleigh wave. This can easily be done by referring to the dispersion curves that are specific to the case studied. For example, in Fig. 3.10, both A_o and S_o achieves the Rayleigh wave velocity at 2mm. Thus, any thickness greater than 2mm will generate the A_o and S_o modes that have the same velocity of Rayleigh waves. For this reason, they are sometimes also known as quasi Rayleigh waves.

Once the minimum thickness is determined, it is desirable to preferentially generate only both the A_o and S_o modes to ensure that only the quasi Rayleigh waves are generated in the medium. This can be done, in the same way as how Rayleigh wave is generated: by using the wedge method (Snell's Law) (Ditri & Rajana 1995). The angle of incidence required to preferentially generate a specific mode of Lamb wave is given by:

$$\theta = \sin^{-1}\frac{c_l}{c} \tag{3.11}$$

Where c_l is the longitudinal wave velocity in the wedge and c is the speed of the specific wave mode that is to be generated. Thus, in the case of generating quasi Rayleigh waves, the speeds of both A_o and S_o are identical to that of Rayleigh waves, making (3.11) identical to (3.4).

Viktorov provides another way to distinguish between Rayleigh wave and Lamb wave in a finite dimension geometry. When a Rayleigh wave emitter (e.g. a wedge at the Rayleigh angle) excites a wave in a material with sufficient thickness (approximately twice the wavelength of the Rayleigh wave), the principal waves excited in this manner is that of the zero order wave modes, A_o and S_o.
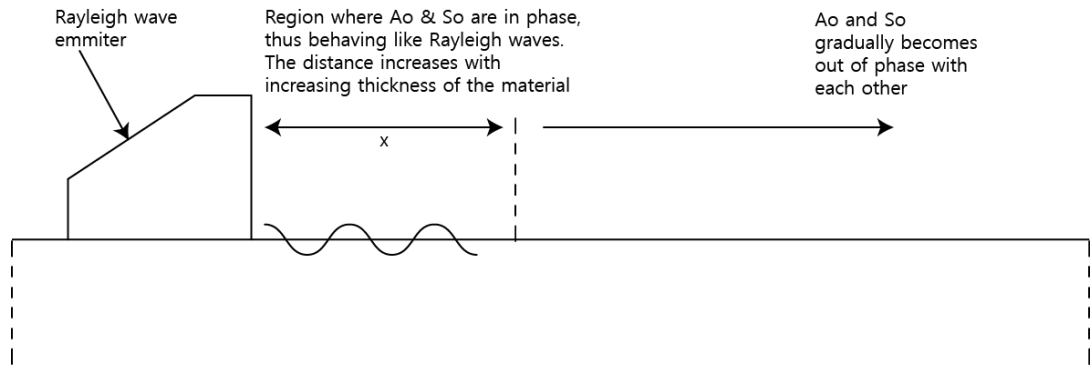
Fig. 3.11 Relationship between A_o and S_o wave modes with Rayleigh wave

At regions close to the emitter, both A_o and S_o are in phase with each other and are indistinguishable from Rayleigh waves. This similarity with Rayleigh wave decreases when the phase difference between A_o and S_o increases as the waves travel further away from the source. This behaviour is illustrated in Fig. 3.11. The distance, x from the emitter where A_o and S_o behaves like Rayleigh waves are given by the condition

$$x \ll M\lambda_R$$

Where M is a coefficient whose magnitude increases with increasing thickness of the substrate on which the surface wave travels. M and the layer thickness, d is related approximately (within 10% accuracy) by (Viktorov 1967).

$$M = \left[\frac{1}{4} + \frac{1}{8(1 - \eta_R^2)} + \frac{1}{8(1 - \eta_R^2 \xi^2)} - \frac{1}{2 - \eta_R^2} \right] e^{2k_R d} \sqrt{1 - \eta_R^2} \qquad (3.12)$$

Where $\xi = \frac{c_s}{c_l}$ and $\eta = \frac{c_r}{c_s}$.

Thus, the region required for A_o and S_o to be generated as quasi Rayleigh waves can be approximated from (3.12).

3.5 Engineering Applications of Rayleigh Waves

The study of Rayleigh waves is important in the field of seismology. Rayleigh waves become dispersive when travelling along the surface of the earth due to changing properties of the earth with increasing depth. This property allows for characterisation of the velocity and seismic attenuation at different depths (Keary et al. 1990).

Like conventional ultrasound, ultrasonic Rayleigh waves are commonly used in NDT to examine surface and near-surface cracks (Hull & John 1988). The working principles remain the same i.e. the defects on the surface generates an echo which is picked up by a receiver unit. Rayleigh waves suffers very little attenuation across long distances, hence a large area of a workpiece can be rapidly inspected using Rayleigh waves. In cases where thin cross sections are to be inspected, Lamb waves are used. One such application is the inspection of pipes shown in Fig. 3.12.
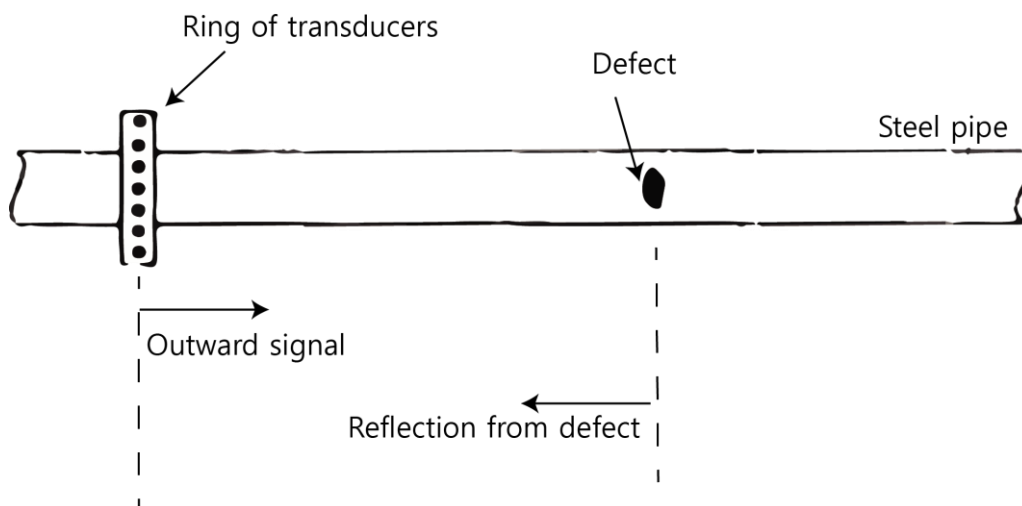
Fig. 3.12 Inspection of pipes using Lamb waves (Lowe et al. 1998)

More generally, surface waves have found uses in electronics and telecommunications in the form of an IDT (Interdigital Transducer) in SAW devices (Datta & Papanikolaou 1986). A typical construction of an IDT is shown in Fig. 3.13. Unlike conventional Rayleigh wave generation method, IDT directly energizes the substrate which is made out of piezoelectric material by applying a voltage across the metallic gratings which then generates SAW. SAW devices reduces costs and have been used as bandpass filters and resonators.
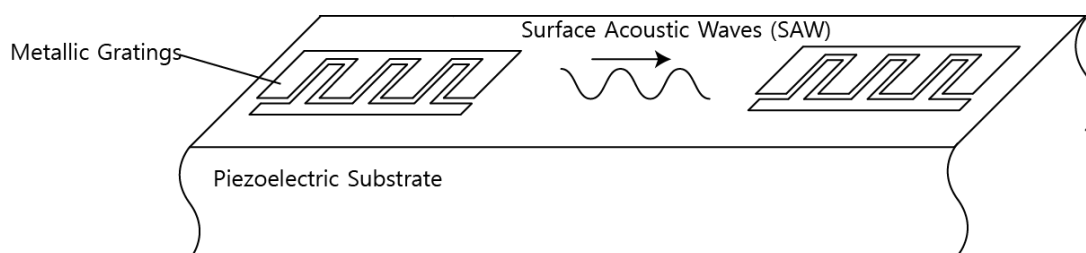
Fig. 3.13 Interdigital Transducer

In recent times, the usage of surface waves has gained attention in the area of microfluidics whereby surface waves are used to actuate droplets in order to study them. Some of the advantages that surface waves bring to this have been cited to be cheaper costs, simple in its application, compact as well as having good compatibility with the testing parameters (Ding et al. 2013).

3.6 Conclusions

Rayleigh waves are a subset of surface waves. This chapter discussed the general aspects regarding Rayleigh waves. Unlike bulk waves, Rayleigh waves propagates along the surface of a material with most of the disturbances taking place at a depth of only one wavelength of the Rayleigh waves. Methods for generating Rayleigh waves were discussed. Particular attention was given to Rayleigh wave generation via a Perspex wedge since it is this technique that is employed in the experimental work conducted for this thesis.

Aspects such as attenuation, beam spreading and the close link between Rayleigh and Lamb waves were considered. Consideration has to be given to the minimum thickness of the material that will generate Rayleigh waves instead of Lamb waves.

Finally, the applications of Rayleigh waves were discussed. Rayleigh waves have been studied extensively in the field of seismology and used as a method of detecting surface flaws. From a broader perspective, surface waves have found applications in electronics in the form of SAW devices as well as applications in microfluidics.

4 Rayleigh Wave Reflection – Literature Review

This chapter consists of a literature review on work previously performed in the study of Rayleigh wave reflection. Sources of Rayleigh wave reflections are first introduced, followed by a systematic review on the existing literature.

4.1 Introduction

When the path through which an ultrasonic wave travels is disturbed, scattering of the waves occurs. The initial trajectory of the ultrasonic wave may change depending on the direction of approach. The manner in which the waves scatter varies greatly depending on the form of the disturbances that takes places.

Certain situations allow for simplification of the matter to pure reflected or transmitted waves. For example, in the case of a bulk (longitudinal) wave normally incident (Fig. 3.1a) on the boundary of a material, the waves are both reflected and transmitted without any change in parallelism.

For bulk waves, it is the difference of acoustic impedances that dictates the normal reflection of the waves. In the case of Rayleigh waves, an 'interface' in the manner defined for bulk waves does not exist. Thus, to analyse Rayleigh wave reflection, different approaches have to be employed.

This chapter is dedicated to the literature review of work previously done on Rayleigh wave reflection upon which a novel solution is employed in describing the response of a Rayleigh wave from a loaded interface.

4.2 Sources of Rayleigh Wave Reflection

In the same way as bulk waves, scattering of Rayleigh waves occurs as disturbances are formed along the path of the Rayleigh waves. These can be divided into two categories:

1. Disturbances formed as a result of change in the material topography and
2. Disturbances formed as a result of change at the surface of the material.

Fig. 4.1 illustrates some of the sources of disturbances that have been studied by various researchers. The studies performed have been a mixture of experimental, analytical, numerical and through the use of finite element software packages.
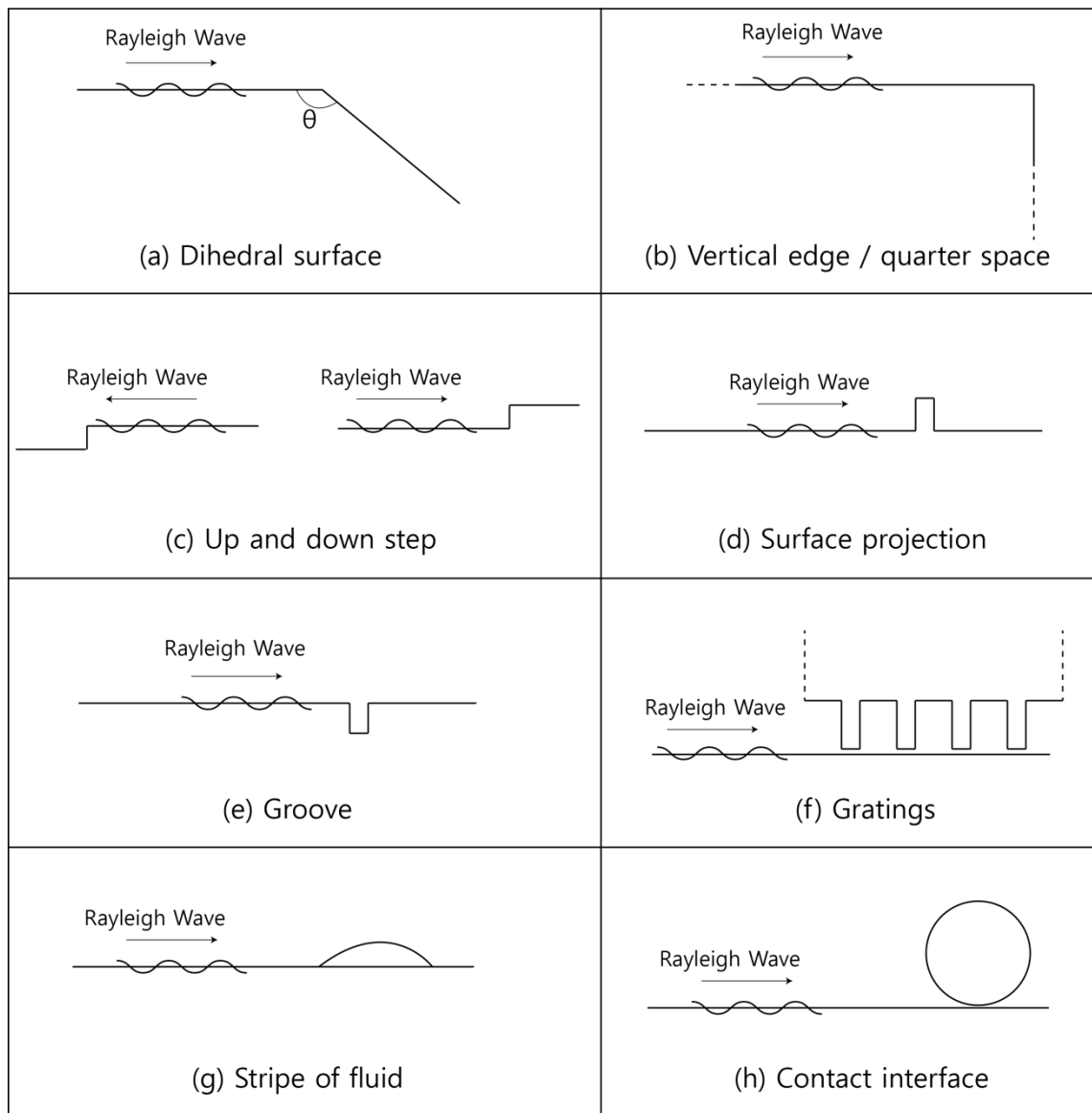
Fig. 4.1 Different surface features that are sources of Rayleigh wave reflection

4.2.1 Reflections Due to Changes in Material Topography

There are many ways in which the topography of a medium can be changed. They can either be through immediate dimensional variations such as an abrupt increase or decrease in height, the appearance of a crack on the surface or subsurface or the effects of chemical interactions such as local formation of rust.

Viktorov (1967) is one of the earliest contributors in this area of work by studying experimentally the effects of Rayleigh wave on an edge as the angle of the edge is varied. The work was conducted on dural specimens between angles of 12° to 170° at a frequency of 2.7MHz. The results are shown in Fig. 4.2.

Two main conclusions were drawn. First, the sum of the surface wave energy that is either transmitted or reflected are always less than 100%. Viktorov attributed this to the conversion of Rayleigh waves to bulk wave in both longitudinal and transverse modes. Secondly, the angle of the edge greatly affects the manner in which the Rayleigh waves are transmitted or reflected as evidenced by abrupt changes in both reflection and transmission coefficient over small angle changes. This is particularly true for small angles.
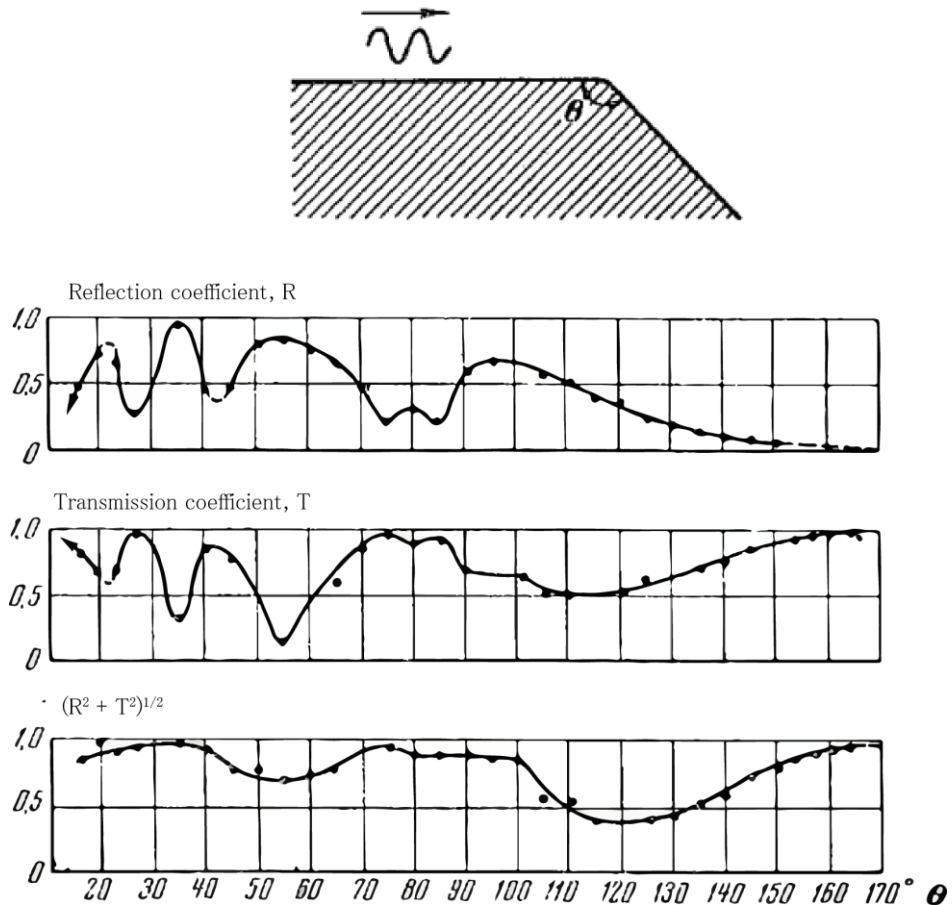
Fig. 4.2 Experimental results for Rayleigh wave incident on an angled edge (Viktorov 1967)

Gautesen (2002) conducted a numerical study of Rayleigh waves incident on a vertical edge of a quarter space of an elastic material. Reflection and transmission coefficients were found to be dependent only on the Poisson's ratio of the quarter space, Fig. 4.3. A comparison made between the work of Viktorov and Gautesen reveals that the reflection coefficients predicted by Viktorov is approximately 15% to 20% higher than that predicted by Gautesen.
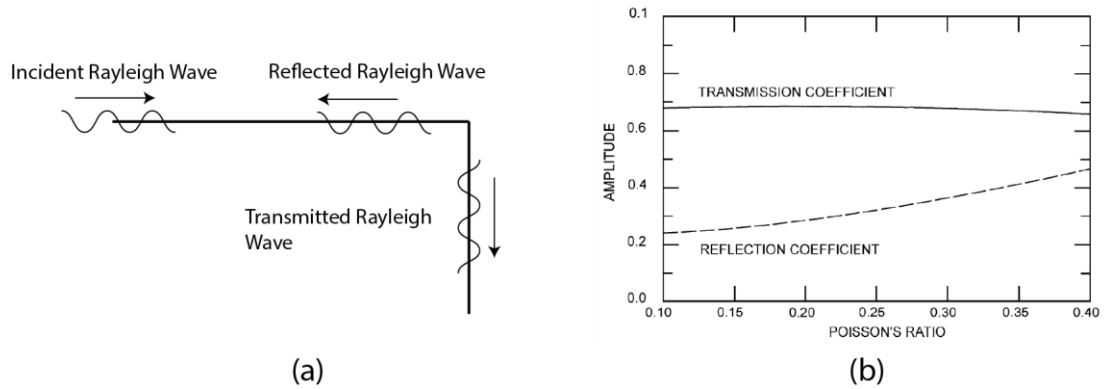
Fig. 4.3 (a) Reflection from a quarter space (b) Accompanying results (Gautesen 2002)

Graczykowski (2012) performed studies of Rayleigh wave reflection from a downward and upward step and a groove of isotropic silicon using finite element methods (Fig. 4.1c,e). It is found that the reflection coefficient varies with the dimensions of the steps and groove. Optimum reflection coefficients were found to occur at height of 0.2λ for an upward step and 0.5λ for a downward step (Fig. 4.4) with a high percentage of the waves being transformed into bulk waves. (note that λ refers to the wavelength of the Rayleigh wave)
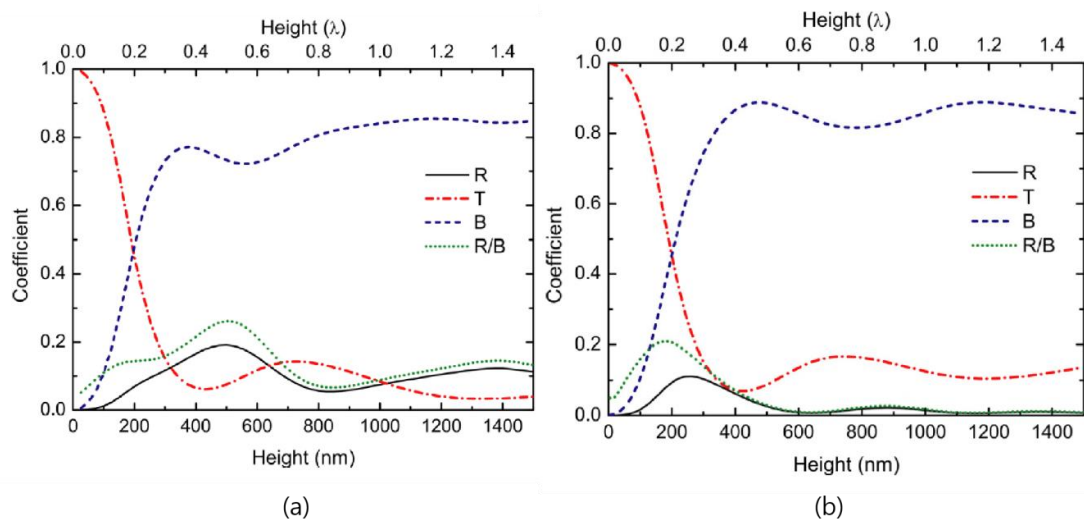
Fig. 4.4 FE simulation results of reflection (R) and transmission (T) coefficient together with bulk wave (B) losses (Graczykowski 2012). (a) Results for a downward step (b) Results for an upward step

In a study to evaluate crack detection in concrete, Hévin et al (1998) produced a numerical model based on IBEM (Indirect Boundary Element Method) to evaluate surface cracks modelled as grooves at different sizes. This is done by analysing the spectral ratios of the reflected pulse which changes as the depth of the crack is varied. The numerical model was compared to experimental results with cracks of 5 mm width and a depth of up to 16 cm by matching numerical and experimental spectral ratios. The agreement was good with an error of less than 15%. Similarly, surface breaking cracks were studied numerically by Angel and Achenbach (1984) where the angle of incidence

of Rayleigh waves on the cracks were varied and a critical angle was found. Numerical methods were also employed by Zhang and Achenbach (1988) to study how Rayleigh wave scatters from a crack that is inclined.

Cook and Berthelot (2001) showed experimentally that it is possible to detect surface cracks caused by fatigue in a steel sample. A set of 5MHz piezo elements were used in rectangular steel bars which are fatigued in tension using a servo-hydraulic machine. Cracks as small as 80 μm in length were detected. Interestingly, when the roughness of the steel bar was increased, no serious degradation on the minimum size of the cracks were encountered. Using Rayleigh waves, the cracks were detected sooner than the use of optical methods.
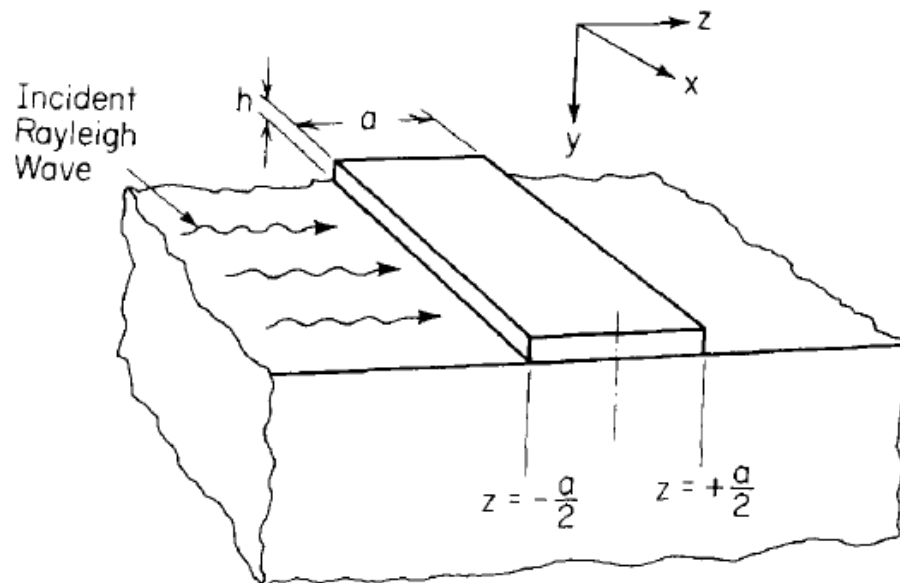
Fig. 4.5 SAW reflection from a thin strip overlay (Datta & Hunsinger 1979)

The study of SAW[1] (surface acoustic wave) reflections has a strong presence in the field of electronics due to the prevalence of applications that takes advantage of SAWs. In most cases, the applications makes use an IDT (interdigital transducer), shown in Fig. 3.13.

In electronic devices, it is often the case that SAW reflects from a thin metallic strip overlaid on to the piezoelectric substrate of an IDT. Datta and Hunsinger (1979) approached the problem of SAW reflection from a thin strip overlaid on and anisotropic substrate (Fig. 4.5) through analytical means. By assuming continuity of particle velocities between the thin strip and the substrate the Datta and Hunsinger derived an expression for SAW reflection given by the expression below:

---

[1] Note the difference between SAW and Rayleigh waves as highlighted in Fig. 3.4. For applications in electronics, the surface waves tend to travel on anisotropic surfaces.

$$r = i(\sin\beta a)(\beta h)\left[\rho' C_s^2 \left(\frac{Z_x + Z_y + Z_z}{\omega}\right) + \left(\frac{\alpha_z' Z_x + \alpha_x' Z_z}{\omega}\right)\right] \qquad (4.1)$$

Where (Note that the manner in which the symbols are defined below applies only to the expression above. Some of the symbols carry a different definition in the rest of the text, in which case they are defined in the nomenclature section)

r	SAW reflection
β	Wavenumber
a	Width of the strip
h	Height of the strip
ρ'	Density of the strip
ω	Wave frequency
$Z_{x,y,z}$	Particle velocites in the x,y and z directions normalized against power per unit beamwidth
C_s	Surface wave velocity
$\alpha'_{x,z}$	Strip stiffness coefficient in the x and z directions

An involved way of analysing SAW reflection from metallic gratings through the use of the variational principle was used by Chen and Haus (1985). The mathematics involved is complex in nature but computations by the authors have yielded good agreement with experimental results, agreeing in both the amplitude and phase of the reflection coefficient.
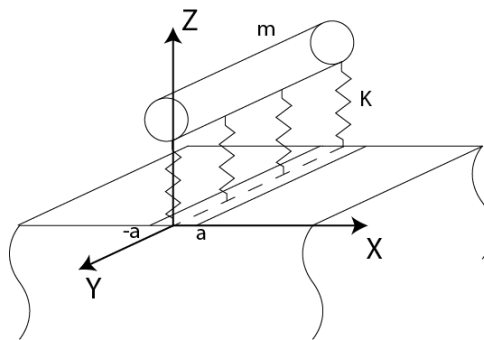
Fig. 4.6 The resonant model (Plessky & Simonian 1991)

Plessky and Simonian (1991) developed an analytical model that models the reflecting elements as a resonator i.e. a single degree of freedom spring system with a mass, *m* and stiffness, *K*. Two different types of resonators were modelled, a vertical and a horizontal resonator. Dependencies between the reflection and transmission coefficient to the resonant frequencies of the resonators were studied and it is shown that a single vertical resonator is capable of producing a reflection coefficient as high as 0.5.

4.2.2 Reflections Due to Surface Changes of the Medium

This section discusses literature regarding Rayleigh wave reflection caused by changes at the surface of a medium. Examples of situations where this might arise are shown in Fig. 4.1f,g,h.

The presence of a liquid obstructing the path of a Rayleigh wave will cause reflections; the manner of which is highly dependent on the shape, size and properties of the liquid. McHale et al (1999) studied the interaction of Rayleigh waves with a stripe of highly viscous liquid (10000 cSt) modelled as a spherical cap. Resonances in the reflected waves were observed as the liquid spreads (an increase in the contact width across time).

Billy and Quentin (1983) performed experiments to study the changes that occurs as a Rayleigh wave passes from a solid-air interface to a solid-liquid interface. This was done by generating Rayleigh waves in a solid that is partially immersed in the liquid (Fig. 4.7a) and observing changes to the reflected waves from the reflector.
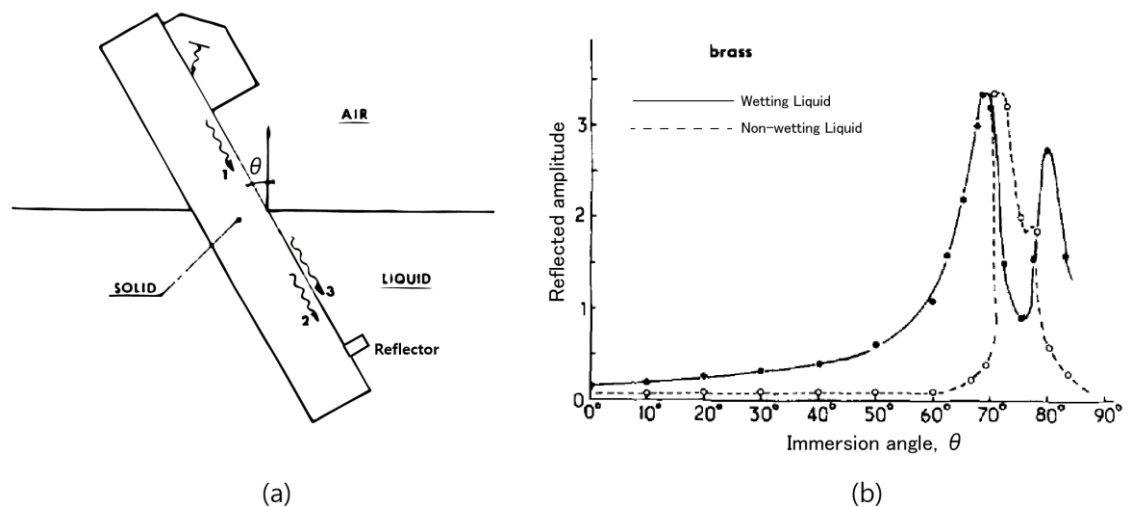
Fig. 4.7 Influence of immersion angle on Rayleigh wave reflection (De Billy & Quentin 1983) (a) Setup (b) Experimental results

Tests were conducted by varying the angle of immersion and changing the wettability of the contact through the usage of additives in the liquid (water). The results show that a liquid that wets the surface increases the reflection coefficient whilst increasing the angle of immersion increases the amount of waves reflected until a critical angle is reached whereby the reflected waves behaves in an erratic fashion (Fig. 4.7b). It is unclear if any reflections were recorded from the liquid-solid-air boundary since it is not reported in the study.

When a solid comes into contact with the surface of the half-space to obstruct the path of the Rayleigh wave, it is expected that there will be reflections arising from the contact interface. Rudy (1967) demonstrated this by applying Rayleigh wave to examine the contact between a piston ring and a bore. Rayleigh wave reflections were recorded along the circumference of the contact and the echoes recorded. It is suggested that the strength of the echoes represents the quality of the contact, with stronger echoes resulting from a contact with greater compliance. Multiple piston-ring to bore samples were tested, both before and after engine testing with the data being represented as a circumferential plot in Fig. 4.8. Comparisons between the before and

after data reveals imperfections produced during engine operation such as the appearance of scuff as indicated by high amplitude reflected waves in Fig. 4.8.

EVIDENCE OF SCUFF
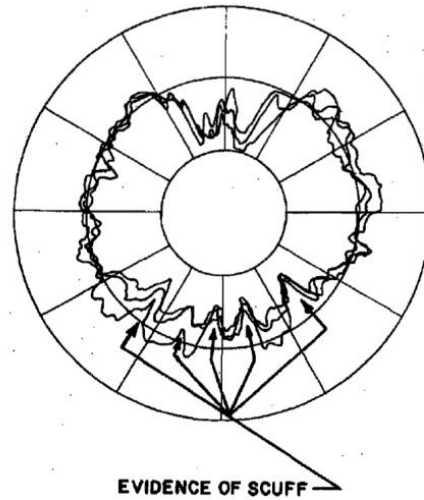
Fig. 4.8 Rayleigh wave reflection along the circumference of a piston ring and bore contact (Rudy 1967)

4.3 Conclusions

In this chapter, available literature pertaining to Rayleigh wave reflection has been reviewed. Broadly speaking, the reflections occur because of an abrupt change in the path of the Rayleigh wave. These changes were grouped into two classes: changes of the topography of the medium itself and changes that occur at the surface.

While studies of Rayleigh wave reflection from the first class yielded meaningful results, most studies performed on the latter class have merely produced, at best a qualitative understanding of Rayleigh wave reflection.

The following chapter details a novel method of analysing Rayleigh wave reflection from a loaded interface – a scenario common in the field of tribology.

5 An Analytical Model of Rayleigh Wave Reflection from an Interface

While a good number of scenarios were analysed by previous works reviewed in Chapter 4, none have provided an analysis on the reflection of Rayleigh wave from an interface formed by Fig 4.1h. This chapter documents the development of a novel model that describes the reflection of Rayleigh wave from a loaded interface.

The direction taken in the development of this new model is to develop an expression that is cast in a form that is a function of important tribology parameters (surface roughness, contact stresses, etc). In this way, the problem is made relevant to the field of interest and the influence of each of the parameter to Rayleigh wave reflection can be studied independently.
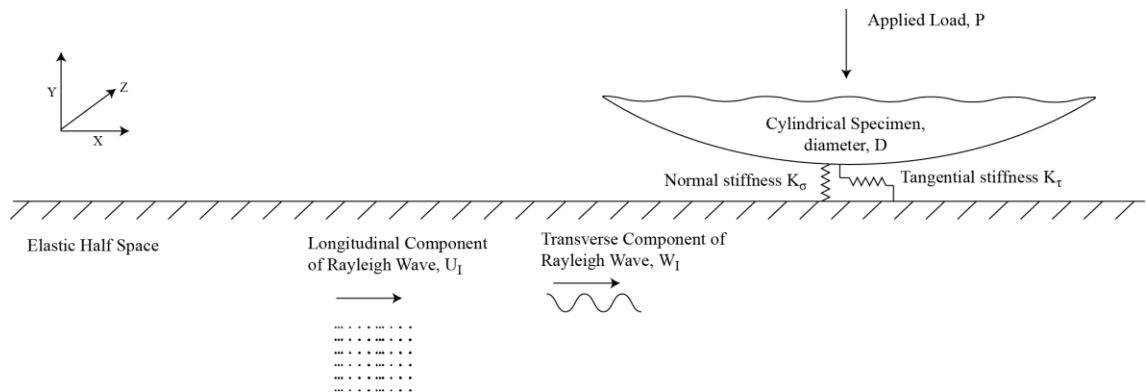
Fig. 5.1 Model of the contact interface

Fig. 5.1 illustrates how the contact interface is modelled together with components of the Rayleigh wave. A contact is formed by a cylinder that comes into contact with the half space. The surfaces that form the contact interface are assumed to be coupled together through their stiffness components, represented as springs. The main assumptions here are

- The model is a 2-dimensional planar model
- Full elastic conditions takes place
- The contact interface appears discrete to the Rayleigh wave. This means that the contact width of the interface has to be much smaller than the wavelength of the Rayleigh wave.

5.1 Fundamental Rayleigh Wave Equations

First, the governing equations of the incident wave approaching the contact interface are described. To do this, the text by Viktorov (1967) is used as the reference text from which fundamental Rayleigh wave equations are described.

The development of the model here is limited to a two dimensional planar problem with the coordinate system shown in Fig. 5.1. Equations describing the motion of Rayleigh waves can be described by the displacements in the x and y axes which are given by Viktorov to be:

$$W_I = Bq_r \left(1 - \frac{2k_r^2}{k_r^2 + s_r^2} \right) \cos(k_r x - \omega t) \tag{5.1}$$

$$U_I = Bk_r \left(1 - \frac{2q_r s_r}{k_r^2 + s_r^2} \right) \sin(k_r x - \omega t) \tag{5.2}$$

Where B is an amplitude coefficient, and ω is the wave frequency. k_r, k_l, and k_t are the wavenumbers of the Rayleigh, longitudinal, and transverse waves respectively, and:

$$q_r = \sqrt{k_r^2 - k_l^2} \qquad s_r = \sqrt{k_r^2 - k_t^2}$$

W_I represents the displacements that take place in the vertical (y) direction while U_I represents the displacements taking place in the horizontal (x) direction. The direction of travel for the Rayleigh wave is in the positive-x direction.

The Rayleigh wave will impinge on the contact interface and excite the modelled springs. The excitation of the springs will in turn create a reaction through the elastic half space which appears as a combination of bulk and Rayleigh waves. The next section discusses the response of the springs due the excitation of the Rayleigh waves.

5.2 Response of the Interface Due to Incident Wave Components W_I and U_I

(a) Vertical Excitation   (b) Horizontal Excitation
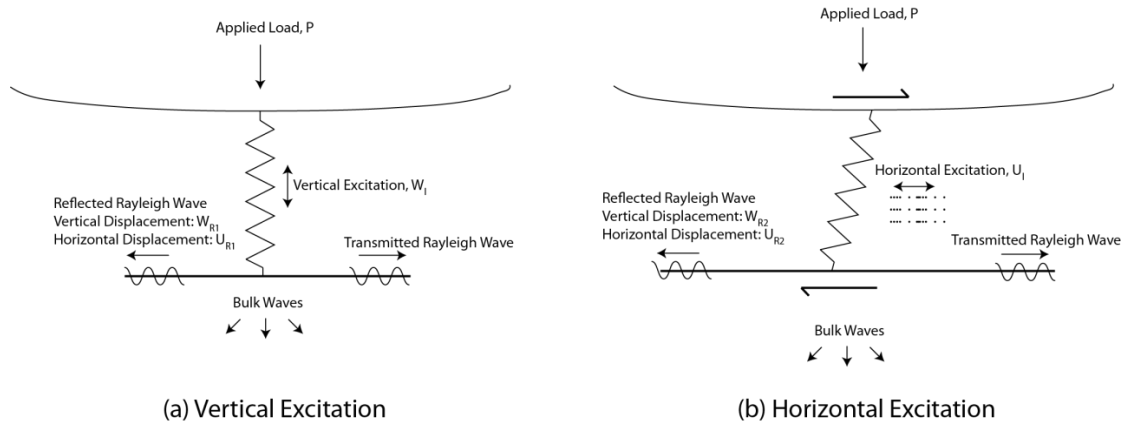
Fig. 5.2 Response of the interface to both vertical and horizontal excitations

Fig. 5.2 illustrates the different form of wave modes generated as the interface is excited by both W_I and U_I. As the incident Rayleigh wave impinges on the interface, the vertical components of Rayleigh wave (W_I) excites the modelled spring in the vertical direction in a periodic fashion.

This excitation causes the spring to vibrate and some of the vibrations from the spring are then transferred back into the half space, producing transmitted and reflected Rayleigh waves and bulk waves. The action of the spring in generating the wave field in the half space can be viewed as a line source that oscillates vertically at the surface which then generates the wave field.

The displacements that occur due to the reflected Rayleigh waves caused by W_I are separated into the vertical and horizontal components, denoted as W_{RI} and U_{RI} respectively (Fig. 5.2a). The expressions for the wave fields generated in this way have been derived by Lamb (1904). At large distances on the surface of the material away from the line source, the Rayleigh wave generated is given by

$$W_{R1} = -i\frac{\delta F_1}{2lG}\psi e^{i(k_r x - \omega t)} \tag{5.3}$$

$$U_{R1} = -\frac{\delta F_1}{2lG}\varphi e^{i(k_r x - \omega t)} \tag{5.4}$$

Here, δF_I is the periodic force due to vertical spring excitation, G is the shear modulus, l is the length of line contact (extending into the y-x plane) formed by the line source and ψ, φ are constants that is a function of the half-space Poisson's ratio.

The case for the response due to the horizontal excitation shown in Fig. 5.2b takes place in exactly the same way. Thus, the analogous expressions for Rayleigh wave due to the horizontal excitation, U_I can be expressed as

$$W_{R2} = \frac{\delta F_2}{2lG}\psi' e^{i(k_r x - \omega t)} \tag{5.5}$$

$$U_{R2} = -i\frac{\delta F_2}{2lG}\varphi' e^{i(k_r x - \omega t)} \tag{5.6}$$

Where δF_2 is the periodic force due to horizontal spring excitation and ψ', φ' are constants that are functions of the half-space Poisson's ratio. The constants ψ, φ, ψ' and φ' are dependent only on Poisson's ratio, ν. The exact expressions for these constants are cumbersome and hence left in Appendix A. It is more convenient to graphically represent the values of these constant within the range of Poisson's ratio that most common materials lie. Fig. 5.3 shows the range of values for the constants.
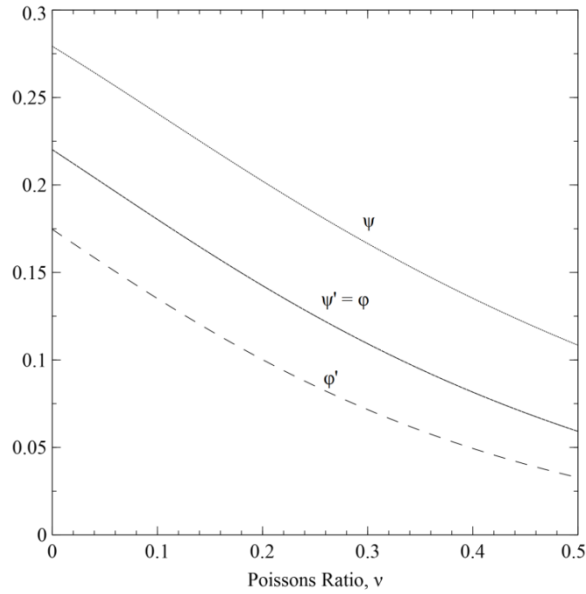
Fig. 5.3 Values of constants $\varphi, \varphi', \psi, \psi'$ as Poisson's ratio, v is varied

5.3 Deriving Reflection Coefficient

Having defined the incident and reflected wave functions in sections 5.1 and 5.2 respectively, it is now possible to define the reflection coefficient of the Rayleigh wave. In the x-direction, the reflection coefficient is defined as the ratio of reflected horizontal displacements to incident horizontal displacements[2].

$$R_x = \frac{Reflected\ horizontal\ displacements}{Incident\ horizontal\ displacements} = \frac{U_{R1} + U_{R2}}{U_I}$$

Substituting equations (5.2), (5.4) and (5.6) yields

$$R_x = \frac{-1}{2lG}\left[\frac{\delta F_1 \varphi + i\ \delta F_2 \varphi'}{U_I}\right] \tag{5.7}$$

Similarly, the reflection coefficient in the y-direction can be defined as

$$R_y = \frac{Reflected\ vertical\ displacements}{Incident\ vertical\ displacements} = \frac{W_{R1} + W_{R2}}{W_I}$$

Substituting equations (5.1), (5.3) and (5.5) yields

$$R_y = \frac{1}{2lG}\left[\frac{-i\delta F_1 \psi + \ \delta F_2 \psi'}{W_I}\right] \tag{5.8}$$

---

[2] This follows the traditional definition of a reflection coefficient which is a ratio of reflected to incident displacements. Note that this derivation is not mathematically rigorous and, therefore, require further investigation.

Equations (5.7) and (5.8) can be simplified by recognizing that the stiffness of an interface (Fig. 5.1) in the normal and tangential directions, K_σ and K_τ respectively, are given by:

$$K_\sigma = \frac{\delta F_1}{W_I} \tag{5.9}$$

$$K_\tau = \frac{\delta F_2}{U_I} \tag{5.10}$$

The derivation of (5.9) and (5.10) is detailed in the next section (c.f. (5.14) and (5.15)). By substituting (5.9) and (5.10) into (5.7) and (5.8):

$$R_Y = \frac{1}{2lG}\left[-i\psi K_\sigma + \frac{\psi' U_I}{W_I} K_\tau\right] \tag{5.11}$$

$$R_x = \frac{-1}{2lG}\left[\frac{\varphi W_I}{U_I} K_\sigma + i\varphi' K_\tau\right] \tag{5.12}$$

The total reflection can then be defined as

$$R = \sqrt{R_x^2 + R_y^2} \tag{5.13}$$

5.4 Interface Stiffness

Although the interface is modelled as a spring, the manner in which the stiffness of the spring behaves is unknown. Fig. 5.4 illustrates how the spring might respond to an applied periodic force in the vertical direction. The case for a horizontal excitation takes place in exactly the same manner.

The insert in Fig. 5.4 shows a load-displacement graph with the stiffness of the modelled spring represented as an arbitrary gradient. It is intuitive that the there is no stiffness when no load is applied (i.e. the case where there is no contact at the interface) and the stiffness gradually increases as load is applied. This behaviour is reflected in the arbitrary gradient that represents the stiffness.
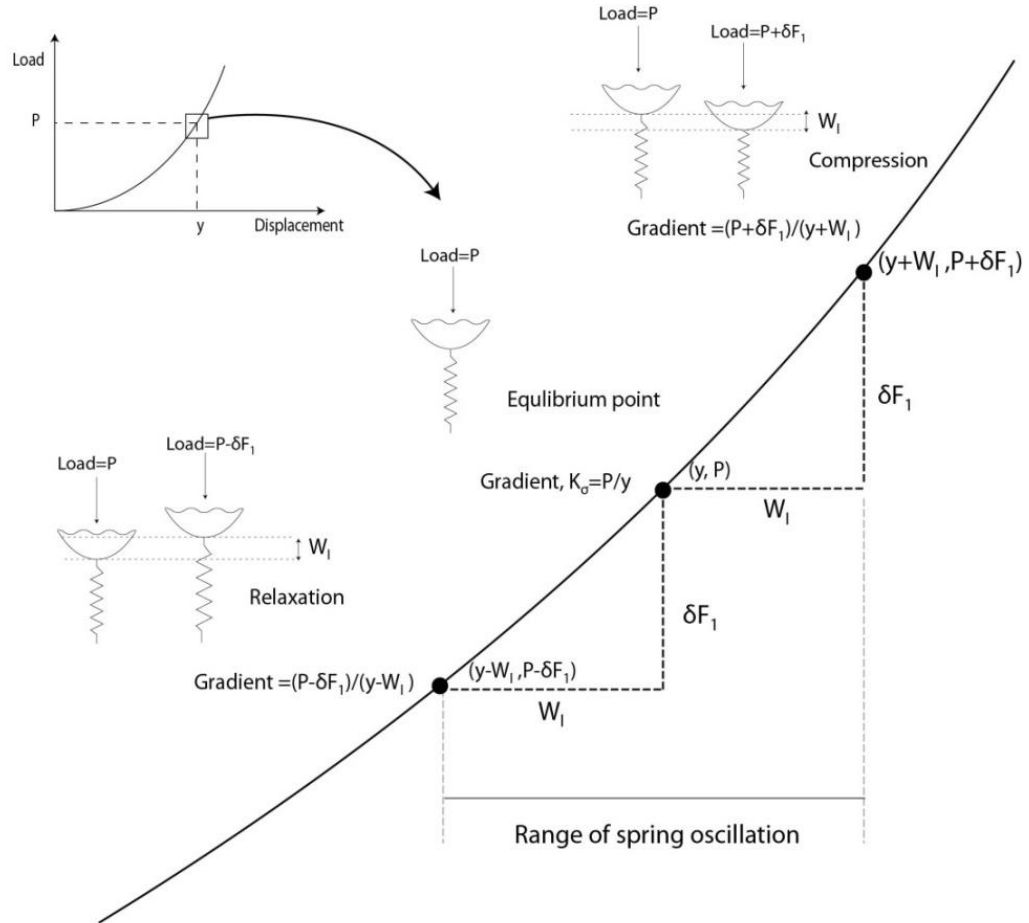
Fig. 5.4 Graphical representation of changes in normal stiffness

When a static load, *P* is applied, the spring undergoes a deformation until it reaches an equilibrium point, (*y,P*). When the spring is excited by the incident components of the Rayleigh wave, oscillation of the spring takes place about the equilibrium point. This results in a periodic change between a relaxation and a further compression of the spring as shown in Fig. 5.4. In practice, W_I is a very small value so it is reasonable to define the normal stiffness as:

$$K_\sigma = \text{Gradient at } (y, P) \approx \text{Gradient at } (y \pm W_I, P \pm \delta F_1) = \frac{\delta F_1}{W_I} \qquad (5.14)$$

Analogously, the tangential can also be defined as:

$$K_\tau \approx \frac{\delta F_2}{U_I} \qquad (5.15)$$

Therefore, although the exact behaviour of the stiffness is unknown, the changes to the stiffness that occur at the equilibrium point due to oscillations induced by W_I and U_I are small such that they can be ignored.

Next, the exact expression for stiffness is required. Physically, the stiffness arises due the elastic forces within the material that acts in reaction to the applied loading. For real surfaces in contact, the surfaces are rough and are composed of a collection of asperities. Because of this, the contact stiffness arises from two mechanisms (Johnson 1985) , elastic deformation and interaction of surface asperities and bulk deformation of the body as a whole.
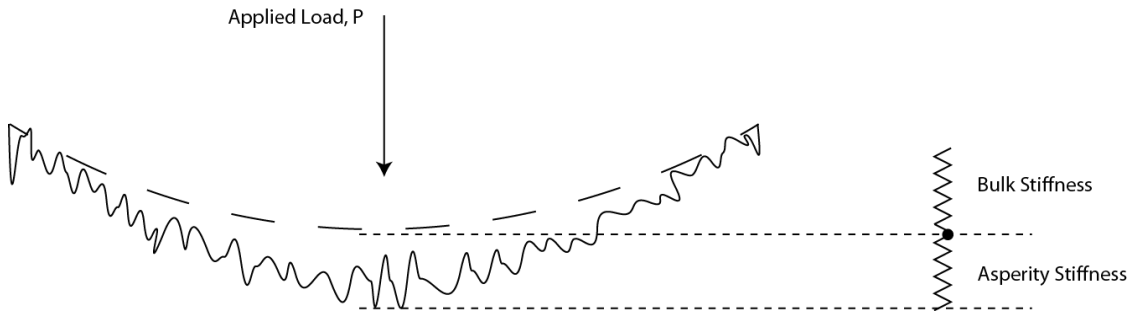
Fig. 5.5 Multi-scale stiffness in a line contact

Fig. 5.5 shows how the two mechanisms take place. The bulk deformation manifests itself as bulk stiffness and likewise for the interaction of the asperities. The two components act in series and thus can be defined (for both normal and shear stiffness) as:

$$\frac{1}{K_\sigma} = \frac{1}{K_{\sigma-asperity}} + \frac{1}{K_{\sigma-bulk}} \tag{5.16}$$

$$\frac{1}{K_\tau} = \frac{1}{K_{\tau-asperity}} + \frac{1}{K_{\tau-bulk}} \tag{5.17}$$

5.4.1 Stiffness Due to Asperity Interactions

Studies, both analytical and experimental on rough line contacts are comparatively scarce as opposed to those performed on flat contacts. Seminal work by Lo (1969), followed by further improvements by Gelinck and Schipper (1999) provide a framework through which the asperity stiffness of a line contact can be approximated.
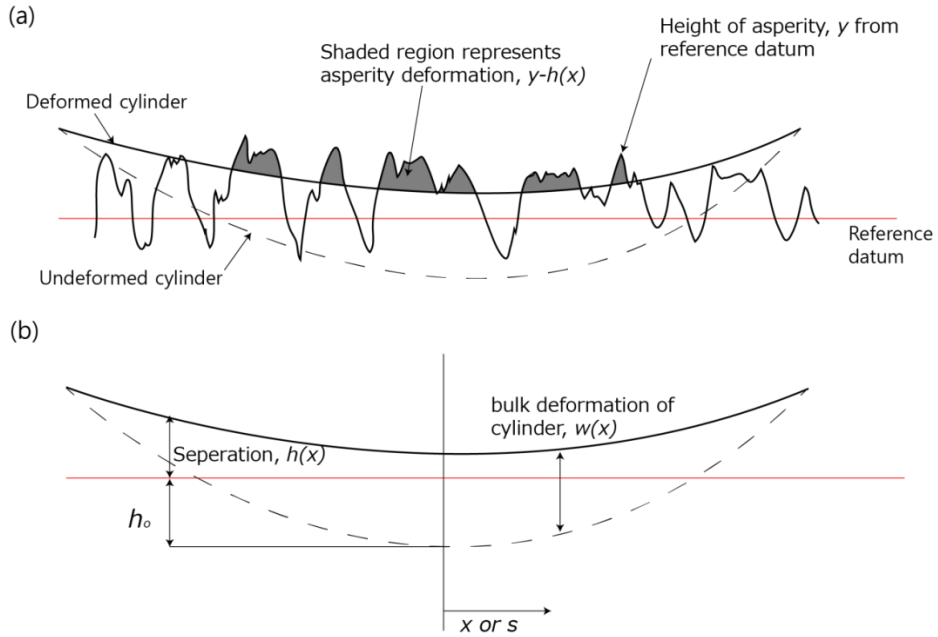
Fig. 5.6 Asperity deformation in a line contact (a) With roughness overlay (b) without roughness overlay showing defined parameters

Fig. 5.6 shows the general model used in studies performed on line contacts. The basis of the work performed by both Lo and Gelinck and Schipper relies on extending the Greenwood and Williamson model (Greenwood & Williamson 1966) for a contact of flat rough surfaces to that of line contacts where the asperities are assumed to have Gaussian height distribution and constant asperity radius in addition to the contact being fully elastic. This is done by assuming that the asperities lie along a profile that is a function of the x-axis due to the curvature of the surface. The governing equations, based on Fig. 5.6 are given below:

$$p(y, x) = \frac{8}{3} l\eta E' \beta^{1/2} \int_h^\infty (y - h)^{3/2} \frac{\exp(\frac{-y^2}{2\sigma^2})}{\sigma\sqrt{2\pi}} \, dy \tag{5.18}$$

$$h(x) = h_o + \frac{x^2}{D} + w(x) \tag{5.19}$$

Where
$p(y,x)$ = pressure profile at the contact

$h(x)$ = nominal separation between the interface

h_o= central separation

l = half length of line contact

η = Asperity density
β = Radius of asperity tip
$$E' = \left(\frac{1 - v_1^2}{E_1} + \frac{1 - v_2^2}{E_2}\right)^{-1}$$

The solution to the problem requires a simultaneous solution of both (5.18) and (5.19). This is a difficult task, requiring complex solution procedures which are beyond the scope of this thesis. To render the problem amenable to a straightforward solution, the assumption that the cylinder is much stiffer than the asperities is assumed. As a result, the bulk deformation, $w(x)$ takes on a negligible value (≈ 0) as it is pressed into the asperities. This assumption is approximately true when the surfaces are rough as the asperities are considered to deform readily as opposed to the bulk of the cylinder. However, the assumption becomes increasingly erroneous as load is increased and bulk deformation becomes significant. This result in

$$h(x) = h_o + \frac{x^2}{D} \tag{5.20}$$

Where the central separation, h_o can be approximated as a function of the total load, P. The process of doing so is detailed in Appendix B.

Due to the added curvature, the stiffness at the interface is expressed as a distribution along the contact width, as shown in Fig. 5.7.
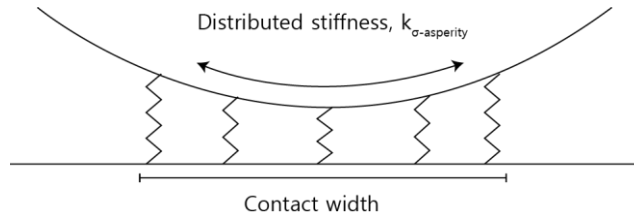
Fig. 5.7 Representation of distributed stiffness in a line contact

The load on a single asperity can be defined as (Greenwood & Williamson 1966):

$$P_i = \frac{4}{3}E'\beta^{\frac{1}{2}}(y-h)^{\frac{3}{2}} \tag{5.21}$$

Where P_i represents the force on a single asperity, i. The stiffness on a single asperity can therefore be calculated by differentiating (5.21) with respect to $(y\text{-}h)$ which is the asperity displacement and is expressed as

$$k_i = 2E'\beta^{1/2}(y-h)^{1/2} \tag{5.22}$$

Where k_i represents the stiffness of a single asperity, i. Not all the asperities at the interface come into contact and the numbers that do make contact are quantified by assuming that the height of the asperities follows a Gaussian distribution. Thus, the probability that an asperity will make contact is given by the condition below:

$$Probability\ that\ height\ of\ asperity, y > seperation, h = \int_h^\infty \frac{\exp(\frac{-y}{2\sigma^2})}{\sigma\sqrt{2\pi}}\ dy \tag{5.23}$$

If N represents the total amount of asperity at the interface, then the number of actual asperities in contact, n can be expressed as

$$n = N \int_h^\infty \frac{\exp(\frac{-y}{2\sigma^2})}{\sigma\sqrt{2\pi}} \, dy \tag{5.24}$$

The distributed stiffness can thus be obtained by applying Gaussian distribution (5.24) to equation (5.22)

$$k_{\sigma-asperity} = 4l\eta E'\beta^{1/2} \int_h^\infty (y-h)^{1/2} \frac{\exp(\frac{-y}{2\sigma^2})}{\sigma\sqrt{2\pi}} \, dy \tag{5.25}$$

Where in this case, N has been replaced with $2l\eta$ to represent the total asperity distributed along the z-axis (Fig. 5.1). To obtain the total stiffness, (5.25) is to be integrated along the x-coordinate to obtain

$$K_{\sigma-asperity} = \int_{-\infty}^\infty k_{\sigma-asperity} \, dx \tag{5.26}$$

In order to evaluate (5.26), the roughness parameters, σ, β, η are required. This can be obtained readily from profilometer measurements for the surfaces involved. For an interface where both surfaces are rough, the composite for the roughness parameters can be expressed as (Beheshti & Khonsari 2012)

$$\sigma = \sqrt{\sigma_1^2 + \sigma_2^2} \tag{5.27}$$

$$\frac{1}{\beta} = \sqrt{\frac{1}{\beta_1^2} + \frac{1}{\beta_2^2}} \tag{5.28}$$

$$\frac{1}{\eta} = \frac{1}{\eta_1}\left(\frac{\beta}{\beta_1}\right)^2 + \frac{1}{\eta_2}\left(\frac{\beta}{\beta_2}\right)^2 \tag{5.29}$$

Where the subscripts 1 and 2 denotes parameters measured for interfaces 1 and 2 respectively. The calculations involved in determining the asperity stiffness for a particular case is detailed in Appendix B.

5.4.2 Stiffness Due to Bulk Deformation

For stiffness due to bulk deformation, the contact is assumed to be perfectly smooth to remove the effects of the asperity interactions. The case of a smooth cylinder pressed onto a rigid flat has been analytically studied by Puttock and Thwaite (Puttock & Thwaite 1969). The total elastic compression i.e. the approach of the bodies, measured along the line of the applied force is given as

$$\alpha = \frac{P}{2l}\left(\frac{1-v_1^2}{\pi E_1} + \frac{1-v_2^2}{\pi E_2}\right)\left[1 + \ln\left(\frac{16l^3}{\left(\frac{1-v_1^2}{\pi E_1} + \frac{1-v_2^2}{\pi E_2}\right)PD}\right)\right]$$

(5.30)

Differentiating (5.30) with respect to P and inverting the equation yields the normal bulk stiffness,

$$K_{\sigma-bulk} = \frac{dP}{d\alpha} = \frac{2\pi E_1 E_2 l}{ln\left(-\frac{16l^3 \pi E_1 E_2}{(E_1 v_2^2 + E_2 v_1^2 - E_1 - E_2)PD}\right)(E_1 v_2^2 + E_2 v_1^2 - E_1 - E_2)}$$

(5.31)

If the contacting bodies are the same, (5.31) reduces to

$$K_{\sigma-bulk} = \frac{l\pi E}{(1-v^2)\ln\left[\frac{8l^3 \pi E}{(1-v^2)PD}\right]}$$

(5.32)

5.4.3 Tangential Stiffness

So far, the derivation for normal stiffness has been made for both bulk and asperity stiffness. Although some studies on the tangential loading applied onto a line contact have been done, mathematical difficulties prevent the evaluation of a closed form solution for the tangential stiffness. Experimental results of stiffness ratios (Królikowski & Szczepek 1993; Biwa et al. 2005; Gonzalez-Valadez et al. 2010) strongly suggest that the normal and tangential stiffness have an almost constant proportionality between them. Therefore it is assumed that

$$\frac{K_\tau}{K_\sigma} = C$$

(5.33)

Where the stiffness ratio, C is a constant that has differing values depending on the distribution and shape of asperity peaks assumed. A summary for the values of C is given by Gonzalez et al (2010) where, C ranges from 0.282 to 0.825.

When the two surfaces forming the interface are made of the same material, analytical studies (Baltazar et al. 2002; Mindlin 1949) have shown that the stiffness ratio can be approximated by

$$\frac{K_\tau}{K_\sigma} = \frac{A(1-v)}{(2-v)}$$

(5.34)

Where A is a constant that takes the value between 0.7 to 2 for a steel-steel interface (Gonzalez-Valadez et al. 2010).

5.4.4 Prediction of R from $K_{\sigma, \tau}$

Having established that the stiffness ratio, C is a constant, the reflection coefficient, R can be predicted from either K_σ or K_τ by substituting (5.33) into (5.13) and arranging for the necessary parameters. This yield a simplified version of (5.13) and is given as

$$R = \frac{K_\sigma}{2lG}\sqrt{\left(\frac{\varphi W_I}{U_I} + i\varphi'C\right)^2 + \left(-i\psi + \frac{\psi'U_I}{W_I}C\right)^2} \tag{5.35}$$

$$R = \frac{K_\tau}{2lG}\sqrt{\left(\frac{\varphi W_I}{CU_I} + i\varphi'\right)^2 + \left(-i\frac{\psi}{C} + \frac{\psi'U_I}{W_I}\right)^2} \tag{5.36}$$

5.5 Analytical Results

In this section, sample calculations were performed in order to exhibit the properties of the analytical model. In all cases, the diameter, D of the cylinder was assumed to be 10mm with a contact length, l of 46mm. Both the radius of asperity tip, β and asperity density, η were assumed to be 20µm and 10^9 m^{-2} respectively. The properties for the various materials used in the calculations are given in Table 5.1.

Table 5.1 Properties of various materials used in sample calculations

	Steel	Aluminum	Brass
Young's Modulus, E	210 GPa	69 GPa	97 GPa
Shear Modulus, G	80.7 GPa	26 GPa	36.2 GPa
Poisson's Ratio, v	0.3	0.33	0.34
Density, ρ	7850 kg/m^3	2685 kg/m^3	8470 kg/m^3
ψ	0.167	0.157	0.153
φ'	0.072	0.064	0.062
ψ', φ	0.109	0.010	0.0095

5.5.1 Stiffness and Reflection Coefficient

Fig. 5.8 shows the stiffness calculated for a steel-steel contact using parameters given in Table 5.1. Here, it is assumed that the stiffness ratio, $C = 0.288$ (the effect of varying stiffness ratio is covered in section 5.5.2).
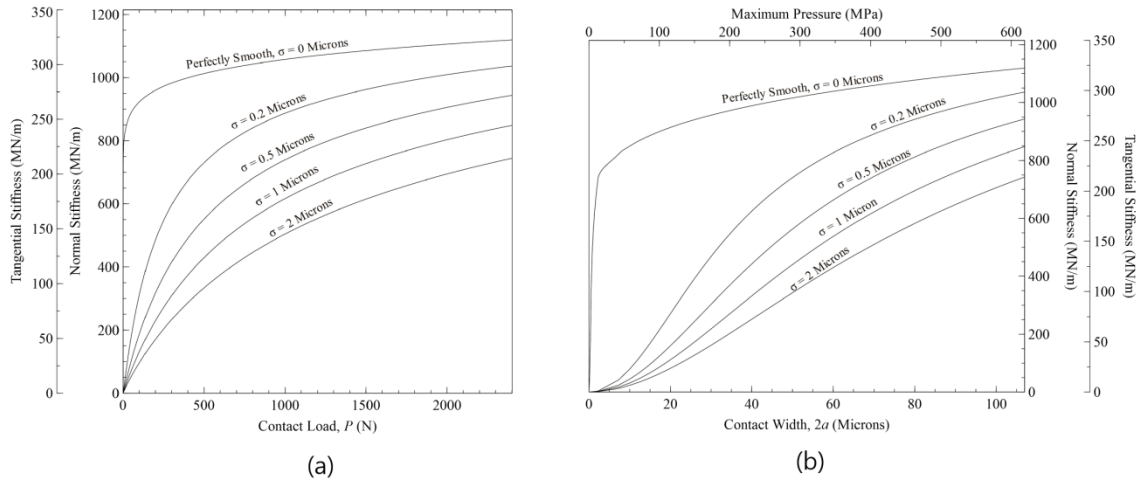
Fig. 5.8 Analytical plots of the absolute values of K_σ and K_τ as they vary with (a) contact load, P and (b) contact width $2a$.

Since both K_σ and K_τ are in direct proportion, both can be expressed as separate axes on the same graph. The results are plotted against both contact load, P (Fig. 5.8a), Hertzian contact width and Hertzian maximum pressure (Fig. 5.8b).

It can be seen that the effect of increasing roughness results in a drop in the overall stiffness. Results in Fig. 5.8 are then applied to equations (5.11), (5.12) and (5.13) to evaluate R. The results are shown in Fig. 5.9.
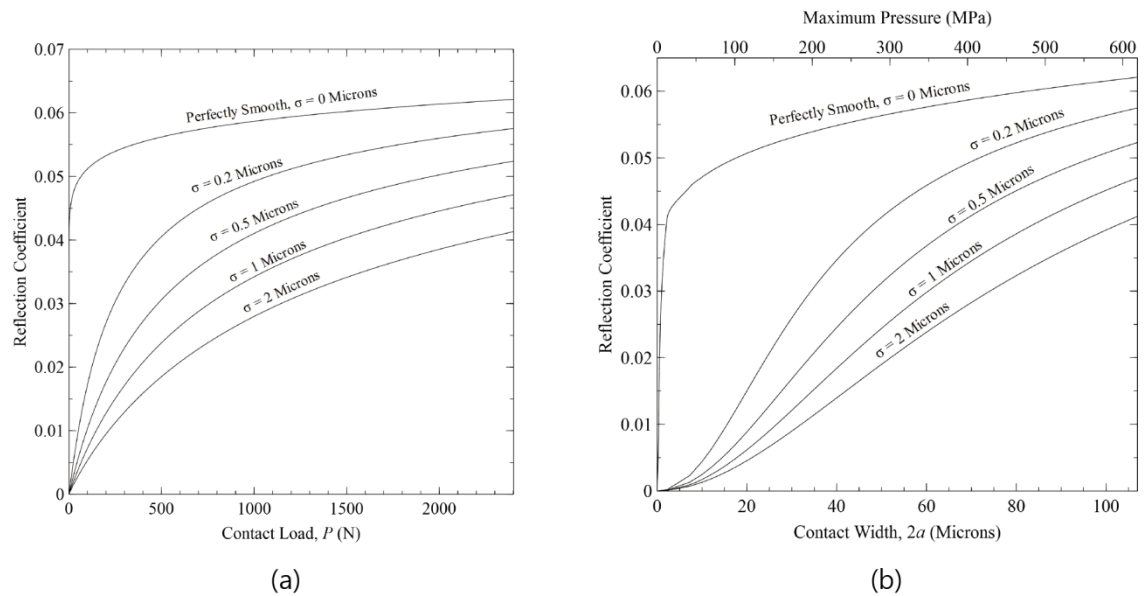
Fig. 5.9 Analytical plots of absolute values reflection coefficient as it varies with (a) contact load, P and (b) contact width $2a$.

Thus it can be seen that R behaves in a similar fashion to both K_σ and K_τ. This is expected as equations (5.35) and (5.36) have shown that R is proportional to both K_σ and K_τ. Also shown is the upper limit of reflection coefficient where the interface is assumed to be perfectly smooth. This gives an indication of the maximum value of reflection coefficient that can be obtained from a given case.

To examine effects of different material combinations, analytical results were calculated for different contact pairs by varying the material of the cylinder. The calculations were performed using the same stiffness ratio (0.288) at $\sigma = 0.2\mu m$. The results are illustrated in Fig. 5.10 for a steel, brass and aluminium cylinder in contact with a steel half space.

Varying the contact pairs has the effect of reducing E' of the interface if a material with lower stiffness is used. The result of having pairs of material with lesser E' is to reduce the overall stiffness at the interface and hence a lower reflection coefficient.
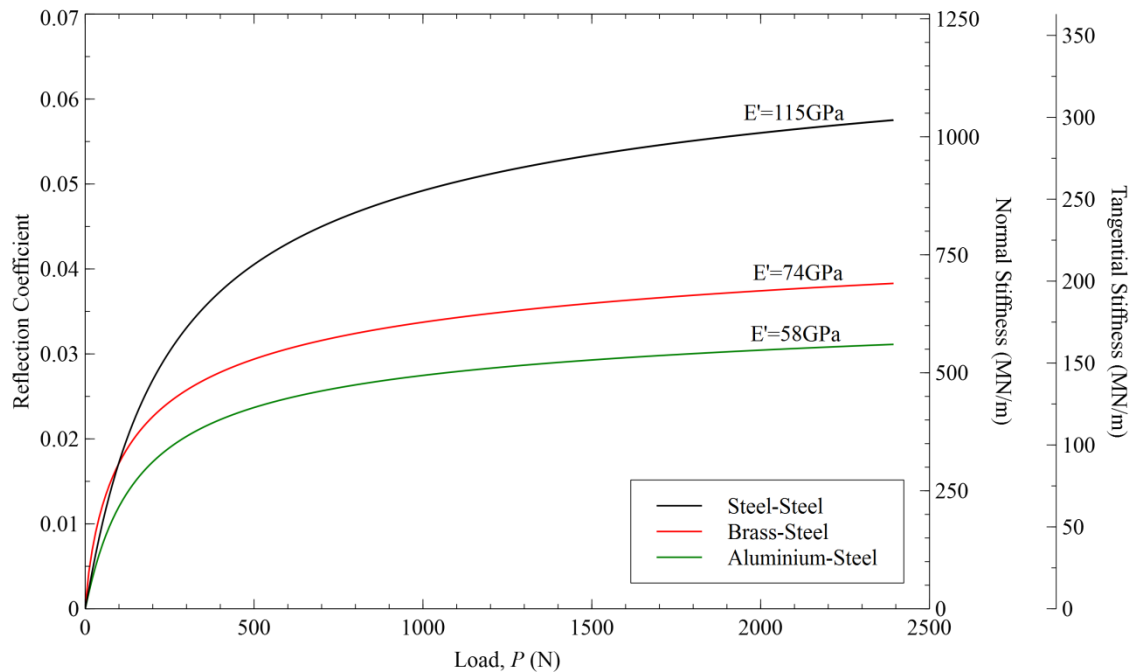
Fig. 5.10 Analytical plots for interface with varying material combinations. Absolute values for R and stiffness were plotted.

5.5.2 Relationship between Reflection Coefficient and Stiffness.

Fig. 5.11 shows data calculated using (5.35) and (5.36) for both reflection coefficient and stiffness plotted against each other. The proportional relationship between R and $K_{\sigma,\tau}$ is clearly displayed.

To demonstrate the effect of varying the stiffness ratios, the plots were generated for the upper and lower limit of the stiffness ratios i.e. at $C = 0.823$ and $C = 0.288$, obtained from literature (c.f. section 5.4.3). As expected, the effect of increasing stiffness ratio is to reduce relative difference between K_σ and K_τ, illustrated in Fig. 5.11where the lines of K_σ and K_τ approaches each other as C is increased. . For intermediate values of C, the plots for K_σ and K_τ will fall in their respective shaded regions.

It is observed that an increase in stiffness ratio reduces the reflection coefficient from the interface (i.e. an increase in K_τ reduces R). This is counter-intuitive and contrary to the case of K_σ where increasing K_σ results in an increase in R.
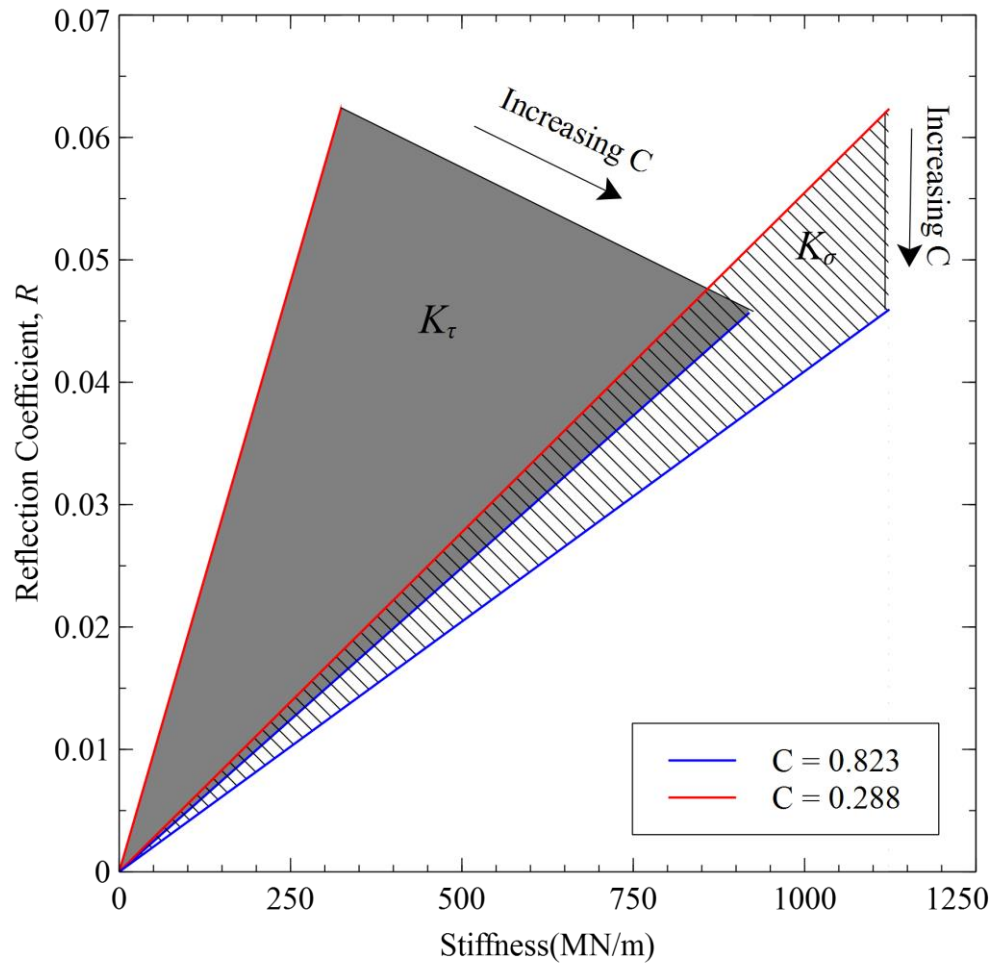
Fig. 5.11 R vs stiffness for a steel-steel contact at varying stiffness ratio. Absolute values for R are plotted

5.6 Discussion

The analytical model predicts a drop in reflection coefficient with increasing roughness (i.e. σ). Physically, a rough contact interface has lesser contact points (for instance, it is well known that the true area of contact for a rough surface is much smaller compared to that of the apparent area of contact). This results in more gaps through which the surface waves are able to pass through, hence reducing overall R.

In addition, rougher surfaces are inherently bad specular reflectors, causing the incident wave to reflect at various angles, diffusing the signal. This is analogous to the reflection of bulk waves from a rough surface where the rougher the surface, the less reflection is obtained as sound is scattered in many different directions.

The analytical model developed here requires proper prediction of both K_σ and K_τ. For an idealized case such as that of a Hertzian contact, the expression for stiffness can be readily determined from contact mechanics since the problem is one that is well defined.

However in the case where the contacts are rough, the analytical predictions are never exact since they rely on an approximate description of the true surface features (e.g. Greenwood and Williamson (Greenwood & Williamson 1966) uses a statistical approach) in addition to idealizations made. Thus, the accuracy of the analytical predictions can only be as accurate as the expressions derived for stiffnesses.

The spring model for bulk waves (Tattersall 1973; Drinkwater et al. 1996; Dwyer-Joyce et al. 2003) predicts a drop in reflection coefficient with an increase in stiffness while for Rayleigh waves, the analytical model presented here predicts the opposite. The difference arises from the physical nature of both waves. In the case of bulk waves, an increase in stiffness increases the compliance of a contact, allowing more waves to pass through while the remaining air gaps reflects the sound waves. In the case of Rayleigh waves, it is the increase in compliance that creates more points of contact that serves as reflectors to the Rayleigh waves while the air gaps allows unhindered passage of the Rayleigh waves through the interface. It should be noted however that in both cases of bulk and Rayleigh waves, the prediction of stiffness remains the same i.e. increase in contact pressure or overall load increases stiffness.

Although the development of the model has been focused on a line contact, the model can be easily generalized to accommodate different contact cases, as long as the assumptions outlined at the beginning of the chapter is adhered to. For example, suppose that the contact is flat, this merely requires that K_σ and K_τ be expressed using expressions derived for flat contacts.

The case where the contact is perfectly smooth provides an upper limit for the magnitude of reflection coefficient that a particular interface is capable of reflecting. This is useful as a way to gauge hardware limitations to decide if a contact can be interrogated using a particular device or if a higher specification device is needed.

5.7 Conclusions

In this chapter, a novel model describing the interaction of Rayleigh waves with a loaded interface was developed. The interface is modelled as a series of springs with the stiffness of the springs governing the amount of energy being reflected from the interface whereby as stiffness increases, so does the reflection coefficient of Rayleigh waves.

Sample calculations were performed to exhibit the behaviour of the model. It is shown that rougher interfaces reduces the overall stiffness at the interface and thus reduces reflection coefficient. Similar results were obtained when contact pairs made out of materials with lesser stiffness (Young's modulus) causes a drop in reflection coefficient.

6 A Finite Element Study of Rayleigh Wave Reflection from an Interface

In this chapter, Finite Element Analysis (FEA) is used to model the response of Rayleigh waves incident on a line contact. This was done through the use of COMSOL Multiphysics, a FEA software package. The results obtained are compared to the analytical solutions from Chapter 5 and discussed.

6.1 Background

FEA is a method of solving complex problems by dividing the geometry of a problem into smaller interconnecting elements. The elements are numerically solved in an iterative manner and the total solutions from all elements are combined to give a representation of the full solution to the complex problem. Due to the amount of computation required in even the simplest of problems, FEA is usually performed using a computer via software packages with FEA capabilities. The work here was performed using COMSOL Multiphysics.

Stage 1: Modelling	Stage 2: Setup	Stage 3: Solution	Stage 4: Data Analysis
- Model appropriate geometry to fit the physical scenario - Assign materials and physical properties.	**Assigning boundary conditions** - Excitation force - Stiffness -Low reflecting boundaries **Meshing** Mesh refinement study	**Finalize simulation parameters** - Initial conditions - Time stepping and range **Parametric sweeps** - Repetition of simulation with different stiffnesses	- Extract reflection coefficient from simulation results -Check that correct physics are applied by observing characteristics of the generated pulse - Comparison with analytical solutions

Fig. 6.1 Workflow of the finite element simulation employed

Fig. 6.1 illustrates the workflow involved in the finite element studies performed here. First, the geometry of the problem is built. This can be done either directly through the software or imported from other CAD (Computer Aided Design) software. This is then followed by assigning the materials to the finished geometry. Boundary and initial conditions are then applied to the problem, followed by meshing of the geometry.

The problem is then solved as a time dependent model whereby discrete solutions are calculated at set intervals across a specified time range to simulate the process of wave

generation and propagation. This is then followed by the post processing stage where relevant quantities are extracted from the stored solution and analysed.

6.2 Geometry of the Model

Fig. 6.2 shows the model built in COMSOL that was used in the simulations together with the appropriate dimensions. The model was solved as a two dimensional, linear elastic problem using plane strain assumptions. The governing equation for the elastic body is given as:

$$\rho \frac{\partial^2 \boldsymbol{u}}{\partial t^2} - \nabla \cdot \boldsymbol{s} = \boldsymbol{g} \tag{6.1}$$

Where ρ is the density of the material, $\boldsymbol{u}$ is the displacement vector, $\boldsymbol{s}$ is the stress tensor and $\boldsymbol{g}$ represents the body forces.

The applied boundary conditions are indicated with their respective colour coded lines in Fig. 6.2. The upper surface of the geometry is left as a free boundary to allow propagation of Rayleigh wave along the surface of the geometry. This assumes that the bordering medium is that of vacuum.
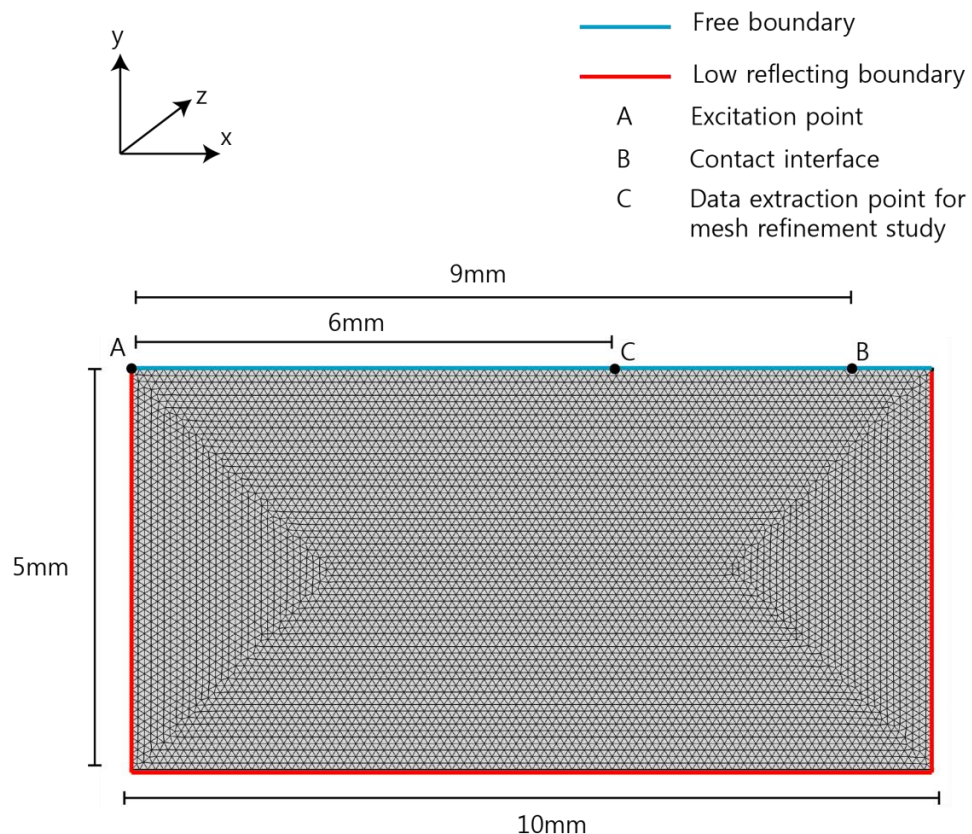
Fig. 6.2 Geometry of the simulation

Low reflecting boundaries applied to the remaining sides of the geometry were used to allow waves to pass through the boundaries. This is done by creating a perfectly

matching interface, hence reducing acoustic impedance mismatch. This attenuates any spurious reflections that might occur in the simulations. Therefore, the boundaries of where a low reflecting boundary condition is applied to can be viewed as a cut-out from a larger body, hence approximating the elastic half space on which the Rayleigh wave travels.

Point A was defined as the excitation point whereby the excitation force defined in Table 6.1 was applied. The contact interface was modelled as a discrete point located at point B. A spring foundation boundary condition (equation (6.2)) was applied to point B, allowing point B to be defined by both K_σ and K_τ.

$$F = -k_p(u - u_o) \qquad\qquad (6.2)$$

Where F is the spring force, k_p is the stiffness vector containing both K_σ and K_τ of the spring and u_o is the initial spring displacement.

When there is no contact, both K_σ and K_τ at B takes the value of 0. The material assigned is Steel AISI 4340. Essential simulation parameters are given in Table 6.1.

Table 6.1 Simulation parameters of steel

Parameter	Values
Density, ρ	7850 kg/m^3
Young's modulus, E	210 GPa
Poissons's ratio, v	0.3
Rayleigh wave speed	2953 m/s
Excitation load per unit length applied at A	$F_y = exp^{-(i\omega t)}$ N/m where F_y = Force applied in the y-direction
Radial frequency, ω	$2\pi f$ rad/s
Frequency, f	2.25 MHz

6.3 Meshing

Meshing is a process whereby mesh elements are added to the model to be solved for. The mesh elements can be viewed as sampling points applied to the geometry where relevant parameters are solved for.

There is always a trade-off in deciding what mesh sizes are appropriate. The smaller the mesh sizes, the more accurate the solutions are since more points are solved for and the problem approaches the exact scenario. However, small mesh sizes increases solution time and can pose hardware issues as it increases demands on the hardware. This is illustrated in Fig. 6.3.

(a)

(b)

Mesh size = 0.1mm
Solution time = 6 minutes

Mesh size = 0.05mm
Solution time = 29 minutes
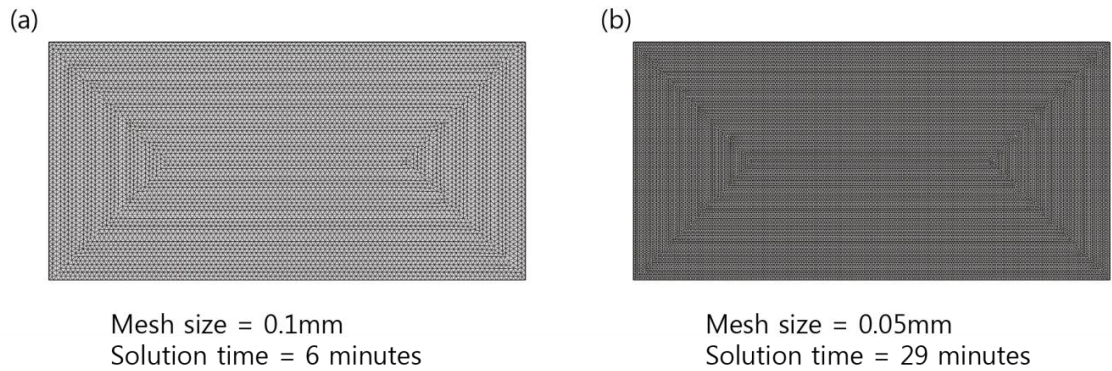
Fig. 6.3 Mesh size comparison (a) 0.1mm mesh (b) 0.05mm mesh

The strategy then is to strike a balance between accuracy and computational cost. As a starting point, it is first necessary to decide the maximum allowable element size for the model. A mesh size that is too large causes aliasing, an effect that causes high frequency waves to appear differently due to insufficient sampling frequency (known also as undersampling). This is illustrated in Fig. 6.4. The Nyquist theorem states that in order to prevent aliasing, a sampling rate of at least twice the frequency is required. It can be seen in Fig. 6.4 that a sampling frequency of $2f$ manages to capture the rough shape of the original waveform.

Sampling at 1f

Sampling at 1.5f

Sampling at 2f

Sampling at 4f

Sampling at 10f
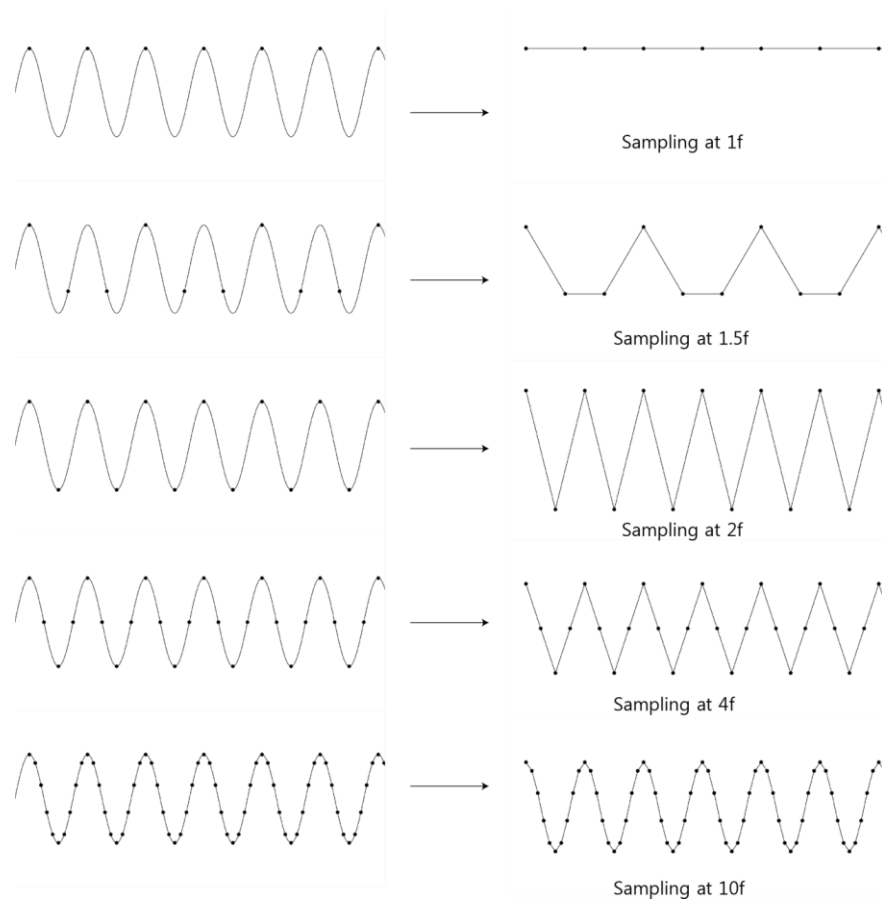
Fig. 6.4 Aliasing effects

Since the mesh is applied in space domain instead of time domain, the analogous to frequency is that of the wavelength of the wave. Thus, a mesh size that is at the very least half the size of the wavelength is required in order to prevent aliasing in the space domain. For the studies performed here, the wavelength of the Rayleigh wave is approximately 1.3 mm. Therefore, the upper bound of the mesh size, according to the Nyquist theorem is 0.75 mm.

Having set the upper limit for the mesh size according to the Nyquist theorem, a mesh refinement study was performed in order to determine the optimum mesh sizes.

6.3.1 Mesh Refinement Study

A mesh refinement study was performed in order to determine the best mesh size that would give the optimum solution time without a significant sacrifice in accuracy of the solutions.

The mesh refinement study was carried out by repeating the simulations on the model shown in Fig. 6.2 with different mesh sizes. An arbitrary parameter was chosen to allow comparison between each repeat from which the errors are deduced. In this study, the total displacement was chosen as the parameter that was used to track the errors.

The solutions from each repeat were then compared to the 'ideal' solution (the finest mesh is chosen as the 'ideal' solution since it is closest to the exact solution) to check for errors. This was done by calculating the percentage error of each repetition. Here, mesh sizes ranging from 1.5 mm to 0.05mm are used. Point C in Fig. 6.2 was chosen arbitrarily from which the total displacements (i.e. vector sum of both x and y displacements) can be extracted. The simulations were performed using values from Table 6.1.

Fig. 6.5 shows how the error for the mesh size evolves as mesh size was varied. The errors were calculated by evaluating the percentage difference in total displacements at point C between each mesh sizes with the finest mesh (0.05mm). It can be seen that a rapid drop in error occurs as the maximum mesh size is decreased from 0.75mm to 0.1mm, reducing from approximately 35% to 1%. Beyond 0.1mm, no significant decrease of error is obtained. Thus, the optimum mesh size chosen for the standard mesh size is that of 0.1mm.
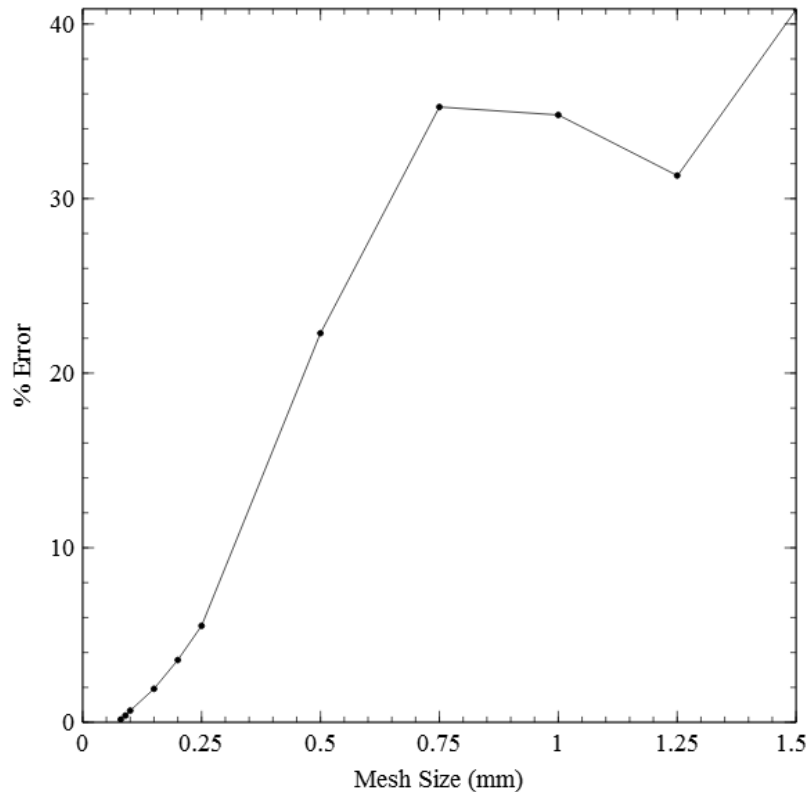
Fig. 6.5 Percentage error in total displacements at C as the standard mesh size is reduced

The optimum mesh size obtained was thus 0.1 mm. The maximum allowable mesh size, according to the Nyquist theorem was calculated to be approximately 0.65 mm. Therefore, the optimum mesh size fulfils the Nyquist theorem as well.

6.4 Simulation Methodology

6.4.1 Initial Conditions
Once the geometry has been built and the mesh added, the next step is to set the model up for solution. First, initial values have to be specified to define the state that the model is in at the beginning of the simulation. Here, the model was assumed to be in stationary equilibrium at the start, hence, the initial values used are:

$$Displacement\ field\ (all\ directions) = 0$$

$$Velocity\ field\ (all\ directions) = \ 0$$

This implies that the stress state is zero at all points at the beginning of the simulation.

6.4.2 Determining Time Range and Step
The simulation was carried out as a time dependent model. This means that all parameters were solved with respect to time, with each time step acting as a single iteration. For example, if a range of 10s with a time step of 1s is solved, this means that the simulation will generate solutions starting from 0s. The solutions from the first

iteration (0s) were used for the next iteration (1s). This carries on until the specified range (10s) is reached. The initial values specified in section 6.4.1 were used for the first iteration.

To determine the time range required, it is necessary to determine when the model reaches steady state conditions as it is in this region where the reflections will be measured. This was done via trial and error, by slowly increasing the time range until steady state conditions become apparent (i.e. when the oscillation stabilizes).

Fig. 6.6 shows a plot of vertical (y) displacements taken from point C showing both the transient and steady state regions. For the study performed here, it was determined that a time range of 40µs is sufficient to allow the model to reach stable conditions.
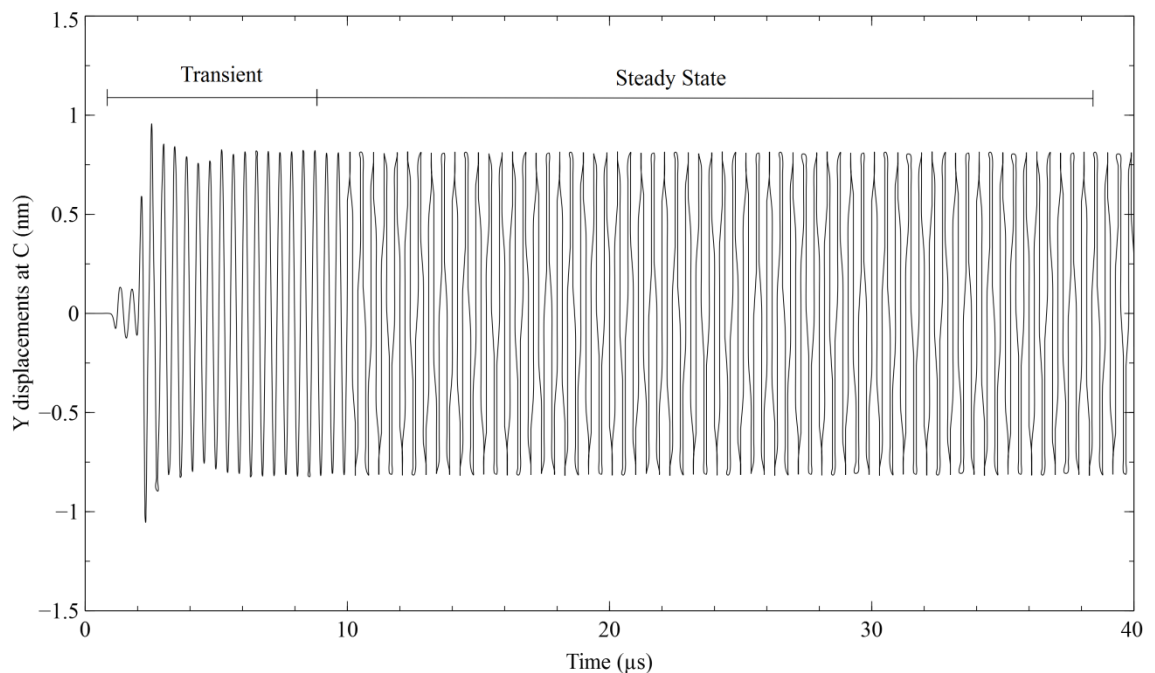
Fig. 6.6 Transient and steady state regions of the simulation

Since the solutions used were carried over from previous iterations, large time steps can cause significant errors by stepping over events that may occur in the time interval, effectively causing aliasing to occur in the time domain. Thus the time steps have to be small enough to avoid such errors.

The frequency of the waves used in the simulations was 2.25MHz. This implies that to prevent aliasing in the time domain according to the Nyquist criteria, a sampling frequency of at least 4.5MHz is required. The time step used was 20ns, this corresponds to a sampling frequency of 50MHz, providing approximately 20 sampling points for each period that takes place and at the same time, fulfilling the sampling criteria laid out by the Nyquist theorem.

6.4.3 Sample Simulation

To illustrate the process of running a simulation and extraction of the required data, a sample is presented here. The parameters and excitation force used in this sample simulation are those from Table 6.1 using a mesh size of 0.1 mm, as determined from the mesh refinement study. The time range used was 40µs with a time step of 20ns.

Reference simulation

First, a simulation for the reference was performed to obtain the reference signal. This was done by running the simulation with a decoupled interface by setting the stiffness at point B to 0.

Fig. 6.7 shows the resulting contour plot of the total displacements of the reference simulation at different time steps. The Rayleigh waves can clearly be seen to travel along the surface as time elapses. Some of the waves were generated as bulk waves. However, the bulk waves were absorbed by the boundaries due to the low reflecting boundary condition that was used, thus preventing bulk reflections from the edges of the geometry.
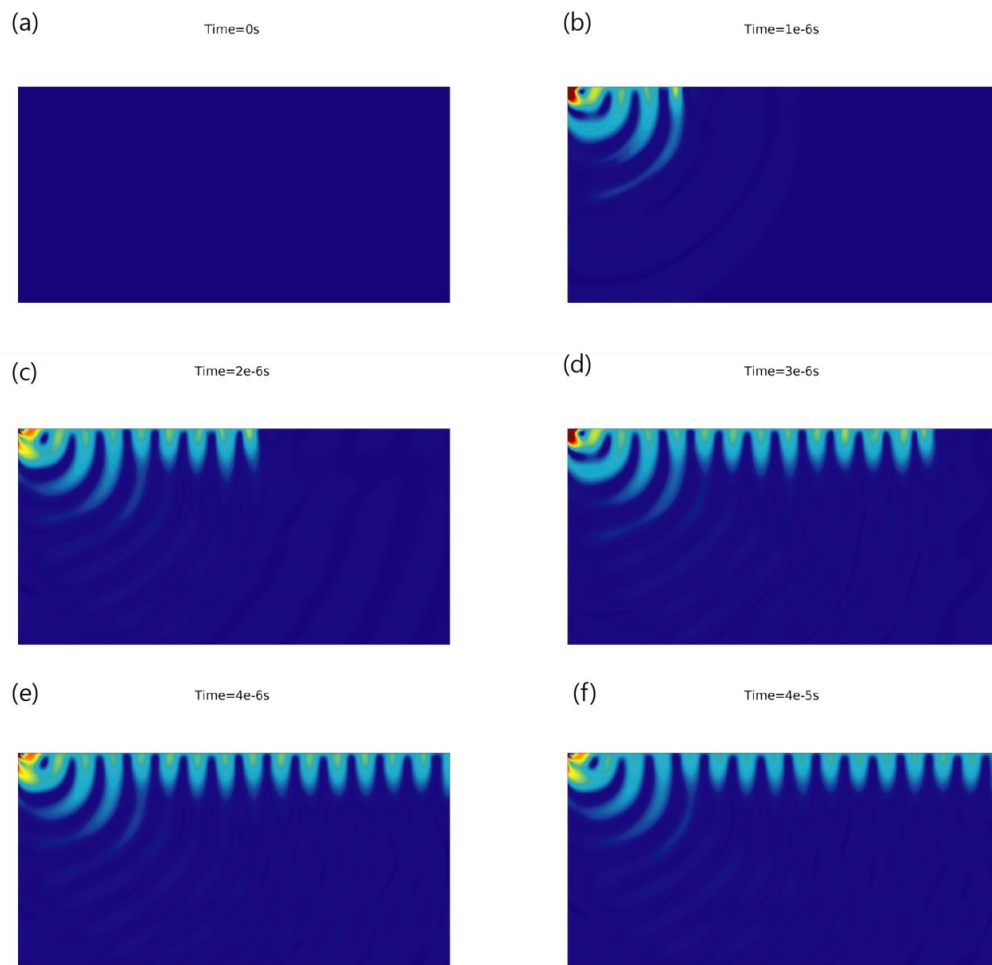
Fig. 6.7 Total displacements of the reference case at different time steps (a) 0s (b) 1µs (c) 2µs (d) 3 µs (e) 4 µs (f) 40 µs, steady state condition

A check was made to confirm that Rayleigh waves are indeed being generated by measuring the wavelength, λ of the wave. This was done by plotting the vertical displacements of the data instead of the total displacement in order to distinguish between the negative and positive amplitudes of displacements.

Fig. 6.8 shows a detailed view of the Rayleigh wave, plotted as vertical displacements. Both the wavelength and depth of penetration are measured to be approximately equal to the expected Rayleigh wave wavelength (approximately 1.3mm for the case simulated) agreeing with the characteristic of a Rayleigh wave.

Displacements along the free surface were recorded for further processing. A plot of the recorded data is shown in Fig. 6.9.
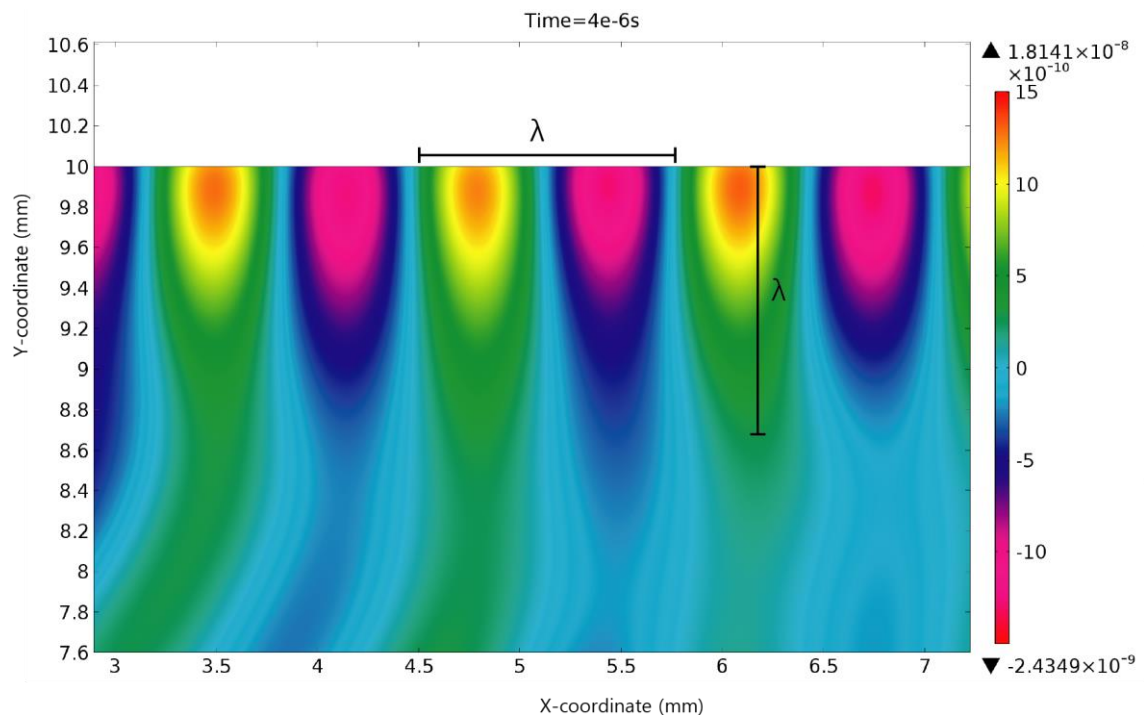
Fig. 6.8 Surface plots of Y-displacement of Rayleigh waves.

Simulation of the loaded case

Next, the loaded case was simulated by ascribing values of K_σ and K_τ to point B and repeating the simulations. In the sample case shown here, K_σ and K_τ were taken to be 1118 MN/m and 322.3MN/m respectively.

Displacements that occur at the free boundary (c.f. Fig. 6.2) were extracted and plotted. Shown in Fig. 6.9 are Y-displacements plotted along the surface of the geometry taken at 40µs (i.e. at steady state conditions). Note that the plots in Fig. 6.9 were plotted against distance in the x-axis instead of the more conventional plots against time (Fig. 6.6).

It can be seen that it is difficult to make a distinction between the reference (i.e. decoupled interface) and the loaded waveforms since the reflected waves are small.

Subtraction of the two sets of data however will clearly reveal the reflected waveforms due to loading that are picked up.
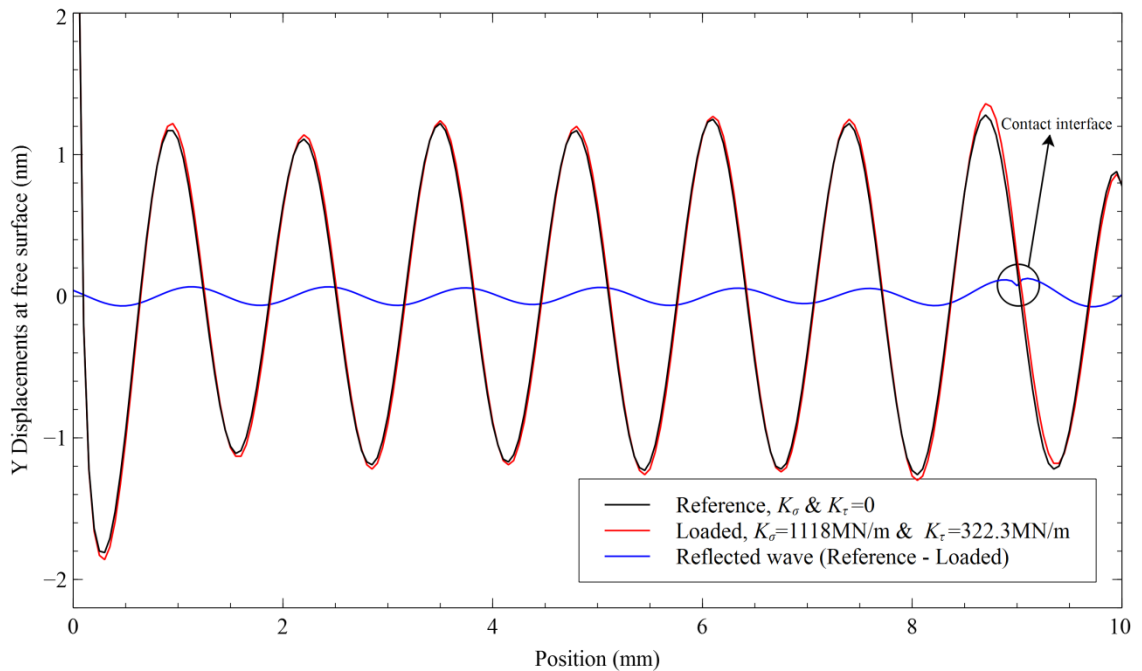
Fig. 6.9 Y-displacements at the free surface for the loaded and reference case at 40µs.

To determine the reflection coefficients, the absolute of the Y-displacements between x = 2mm and x = 7mm in Fig. 6.9 were averaged. Doing so reduces any effects of generated bulk waves (illustrated in Fig. 6.10) that might result from both points A and B.
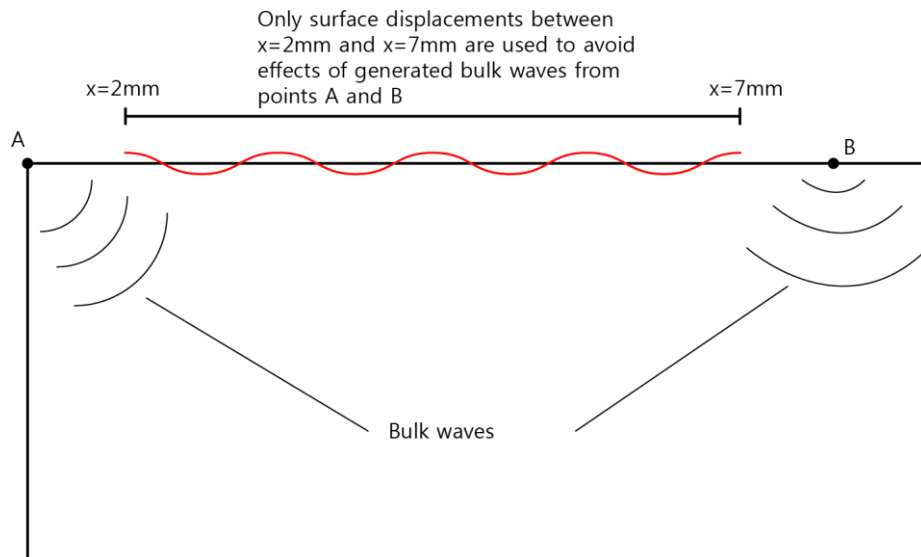
Fig. 6.10 Effects of generated bulk waves

In this way the average amplitudes for both the reference and reflected waveforms can be determined. The same procedure was repeated to evaluate the amplitudes for X-displacements. Table 6.2 summarizes the results.

Table 6.2 Simulated results for the sample case at 40 μs

	Average Reference Amplitudes (nm)	Average Reflected Amplitudes (nm)	Reflection Coefficient
X-displacements	0.498	0.0262	0.0526
Y-displacements	0.765	0.0387	0.0507

The total reflection can thus be calculated using equation (5.13) to be 0.073.

The data shown in Fig. 6.9 and Table 6.2 were calculated for a single time step at 40 μs. The process was repeated for a range of time step from 39.95 μs to 40 μs and the reflection coefficients obtained were plotted in Fig. 6.11. It can be seen that the reflection coefficients oscillate about a median value as time elapses. The median value is used as a representation of the average reflection coefficient obtained from this sample scenario.
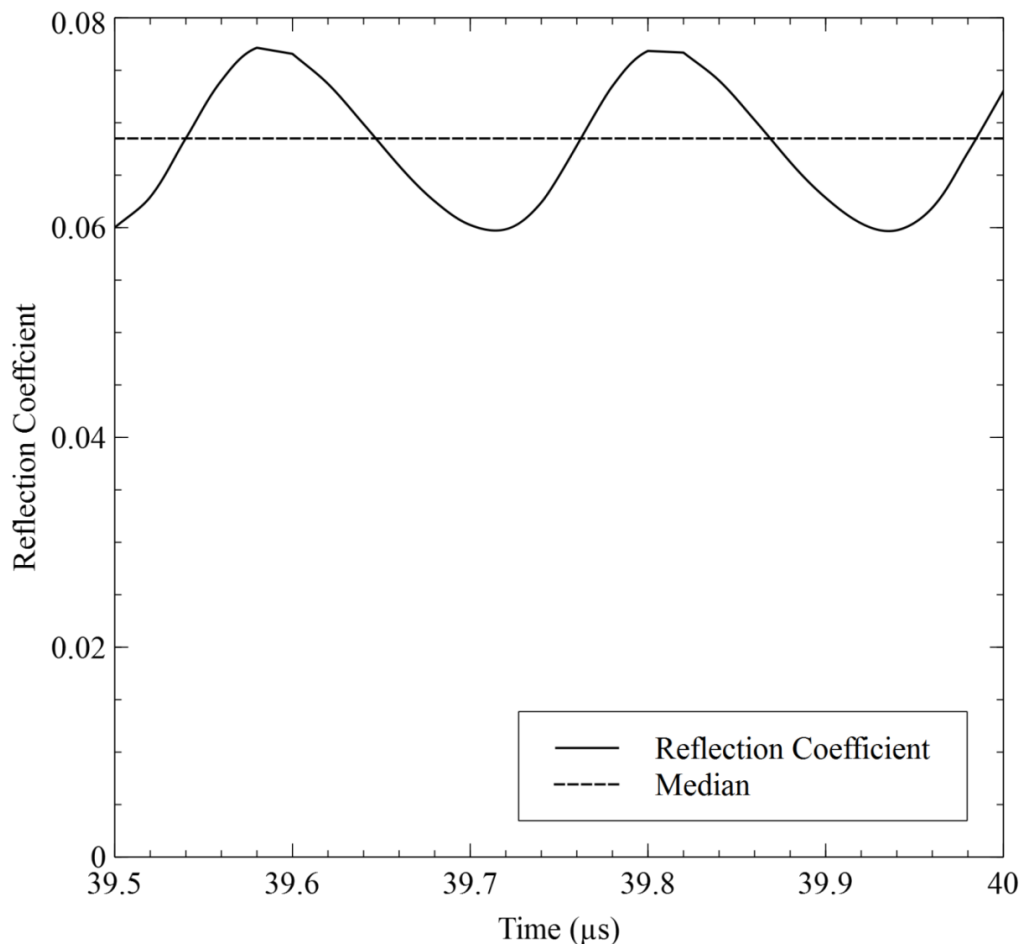
Fig. 6.11 R oscillation across time

The procedure outlined in this section can then be repeated for differing values of K_σ and K_τ to obtain the required reflection coefficient.

65

6.5 Simulation Results

The preceding section showed the sample calculation for a specific case. The same procedures were repeated in order to simulate results for different contact cases. Each contact condition is represented uniquely by both K_σ and K_τ and thus, the simulations are repeated with differing K_σ and K_τ, calculated from section 5.4 for different loading conditions.

First, simulations were performed on the case where contact is perfectly smooth. To investigate the effects of varying stiffness ratio, the simulations were performed at the upper and lower limits of the stiffness ratio, C as defined in equation (5.29). This was then followed by simulations performed on rough contacts. In all cases, the simulations were performed to match the contact conditions that are used in the analytical predictions. This allows a direct comparison to be made between both finite element and analytical results. The simulations were performed using the parameters quoted in Table 6.1.

6.5.1 Perfectly Smooth Contact

For a perfectly smooth contact, the stiffness was evaluated from equation (5.31). Table 6.3 shows the stiffnesses that were used for each simulated case studied in this section. The applied load in Table 6.3 is not to be confused with the excitation load. The applied load represents the equivalent load applied onto the contact interface that would produce the stiffness listed in Table 6.3 e.g. Fig. 5.5. Here, the contact is assumed to have a length, l of 46 mm (along the z axis in Fig. 6.2), the same as that used in the analytical model.

Table 6.3 Simulation scenarios for a perfectly smooth contact

K_σ (MN/m)	K_τ, $C = 0.288$ (MN/m)	K_τ, $C = 0.823$ (MN/m)	Applied load, P (N)
846.1	243.9	696.3	19.48
910.1	262.3	749.0	77.94
952.2	274.5	783.7	175.4
984.6	283.8	810.3	311.7
1011	291.5	832.2	487.1
1034	298.1	851.1	701.4
1054	303.9	867.7	954.7
1072	309.1	882.6	1247
1089	313.8	896.1	1578
1104	318.2	908.6	1948
1118	322.3	920.3	2357

Fig. 6.12 shows both R_x and R_y plotted against load at the upper and lower limits of stiffness ratio, C. The qualitative agreement is excellent in both cases. Both techniques predict that R_x and R_y are similar in terms of magnitude. This can be observed by the lines of both R_x and R_y being almost identical to each other.

(a)   (b)
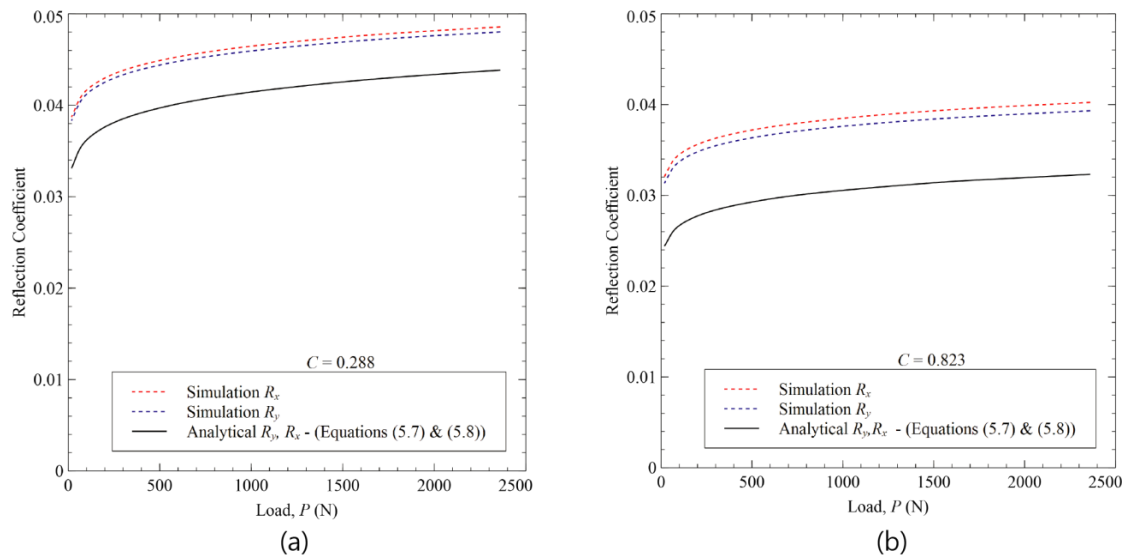
Fig. 6.12 Simulation results for R_x and R_y plotted with analytical results (a) at $C = 0.288$ (b) at $C = 0.823$

The main difference observed between both techniques is that the simulations appear to predict a higher reflection coefficient as opposed to that predicted using analytical methods. Because R is a vector sum of both R_x and R_y, it follows that finite element predictions for R will also be higher than that of analytical predictions. This can be seen in Fig. 6.13a for both the upper and lower limits of C.

To quantify the errors between both methods (analytical and FEA), the percentage differences (normalized against the finite element results) in the curves for each data set were calculated. The results are shown in Fig. 6.13b. It is evident that predictions at $C = 0.288$ produces much less errors, approximately 10% lower as opposed to predictions at $C = 0.823$. The errors decreases as load and hence stiffness is increased, decreasing by approximately 4% to 5% for all the curves shown in Fig. 6.13b.

(a)   (b)
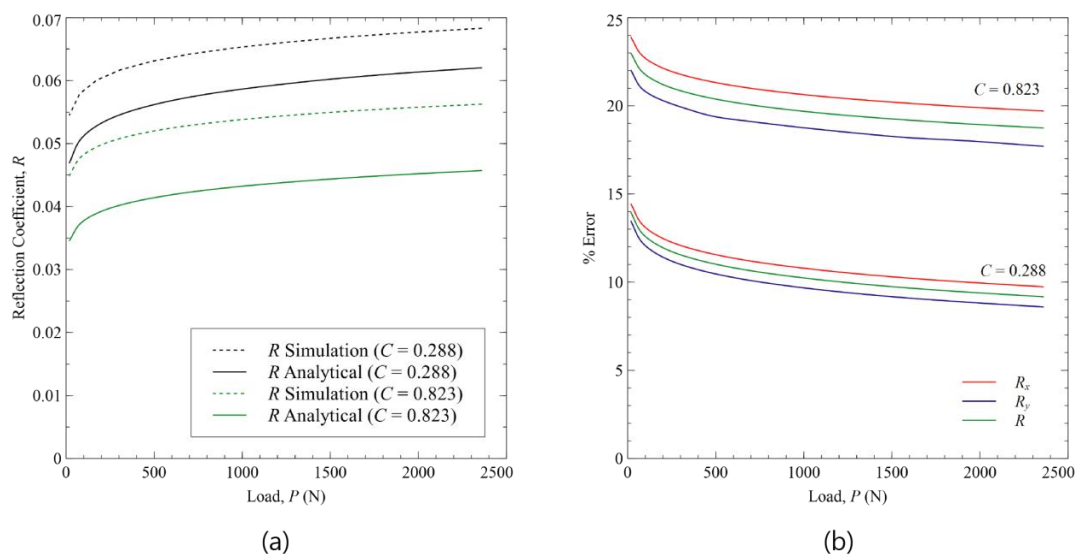
Fig. 6.13 (a) Comparison of simulated and analytical reflection coefficients (b) Errors between analytical and simulated results

6.5.2 Rough Contacts

For the case where contacts are rough, two representative cases from the analytical model were simulated; the high roughness case ($\sigma = 2\mu$m) and the low roughness case ($\sigma = 0.5\mu$m). The stiffnesses used in the simulations of rough contacts are given in Table 6.4. Note that the stiffnesses are calculated at $C = 0.288$ to ensure consistency with the analytical model.

Table 6.4 Simulation scenarios for rough contacts at $C = 0.288$

K_σ ($\sigma = 2\mu$m) (MN/m)	K_τ, ($\sigma = 2\mu$m) (MN/m)	K_σ ($\sigma = 0.5\mu$m) (MN/m)	K_τ, ($\sigma = 0.5\mu$m) (MN/m)	Applied load, P (N)
21.92	6.310	41.69	12.00	19.48
72.27	22.25	151.0	43.50	77.94
123.5	44.21	288.9	83.12	175.4
239.7	69.00	424.7	122.3	311.7
327.8	94.40	544.3	156.8	487.1
412.7	118.9	644.6	185.6	701.4
491.8	141.6	727.3	209.5	954.7
563.9	162.4	765.6	229.1	1247
628.9	181.1	852.2	245.4	1578
687.0	197.9	899.8	259.2	1948
739.5	213.0	940.3	270.8	2357

Fig. 6.14a shows the reflection coefficient, R obtained via FEA compared against analytical predictions. As with smooth contacts, the qualitative agreement remains excellent .The simulations once again predict higher reflection coefficients at both low and high roughness scenarios. The errors were calculated and plotted in Fig. 6.14b, and, similar to smooth contacts, the errors that arise between the two predictions decreases when load is increased.
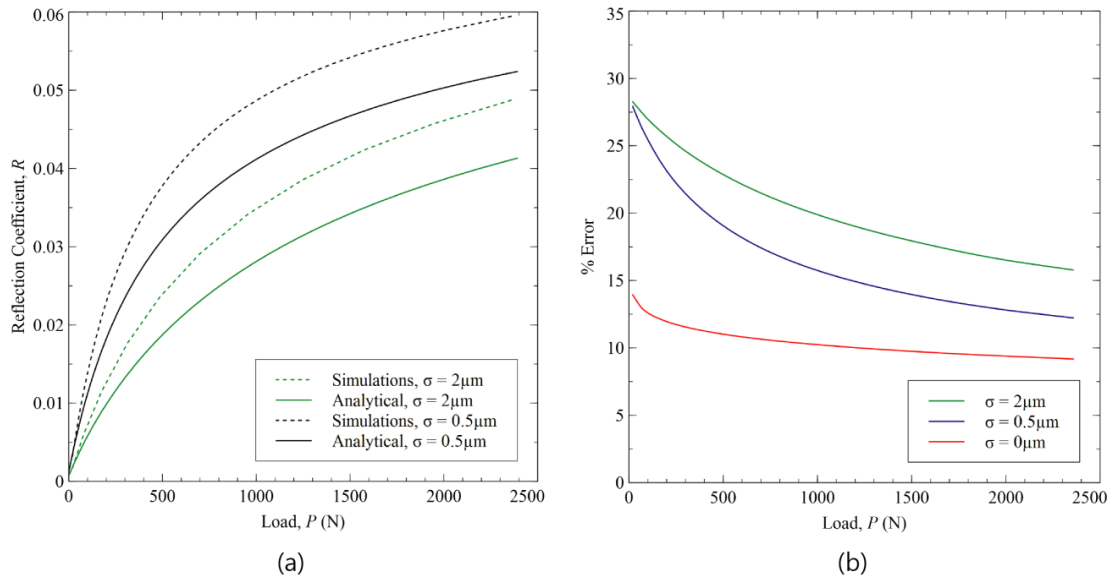
Fig. 6.14 Simulations of rough contacts (a) compared against the analytical model (b) errors between the two predictions

It can also be seen from Fig. 6.14b that the errors decrease as the interface becomes smoother. At the highest load, $P = 2357$N, the errors reduces from roughly 16% for the case where $\sigma = 2$μm to approximately 9% when the contact is perfectly smooth i.e. $\sigma = 0$μm.

6.5.3 Relationship between R and K_σ and K_τ

Having examined the various cases of contact, this section examines in detail how reflection coefficient, R changes with both K_σ and K_τ. Fig. 6.15 shows the analytical model, plotted using equation (5.35) and (5.36) compared to the equivalent simulations at stiffness ratios of 0.288 (Fig. 6.15a) and 0.823 (Fig. 6.15b).
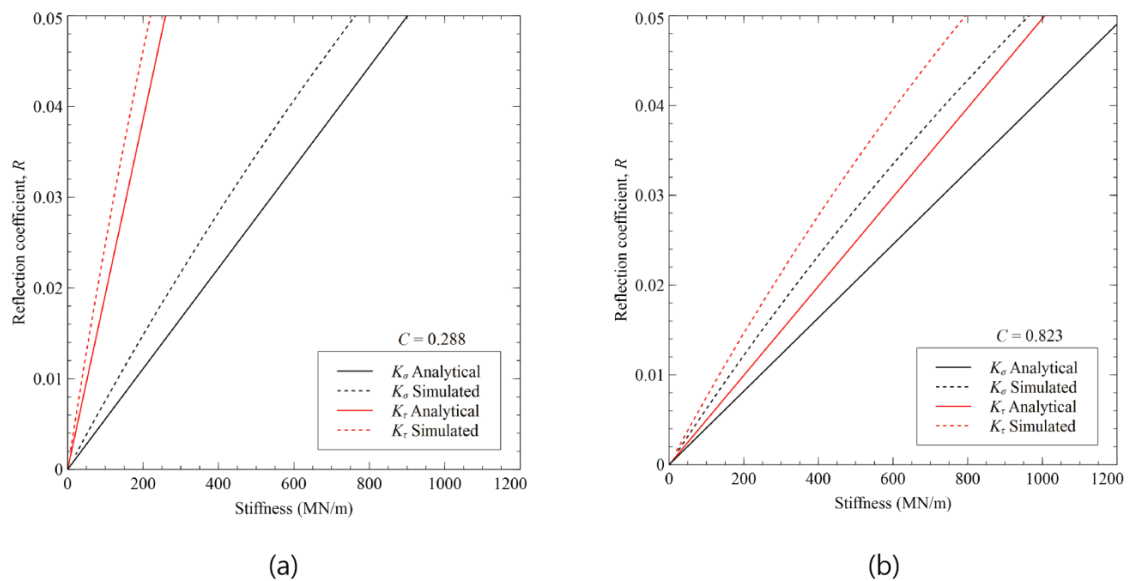
Fig. 6.15 R vs stiffness comparison between analytical model and simulations at (a) $C = 0.288$ (b) $C = 0.823$

It can be seen once again that the qualitative behaviour observed here is excellent, with the simulations showing that reflection coefficients and stiffness are directly proportional to each other. However, the gradient of the straight line predicted by the simulations are always steeper, resulting in a higher R predicted at a specified stiffness.

Fig. 6.16 shows the errors calculated for the plots in Fig. 6.15. The errors appear to be a linear function of stiffness, decreasing linearly as stiffness increases. Also, it can be seen that the errors are higher at C=0.823, agreeing with observations of Fig. 6.13b.
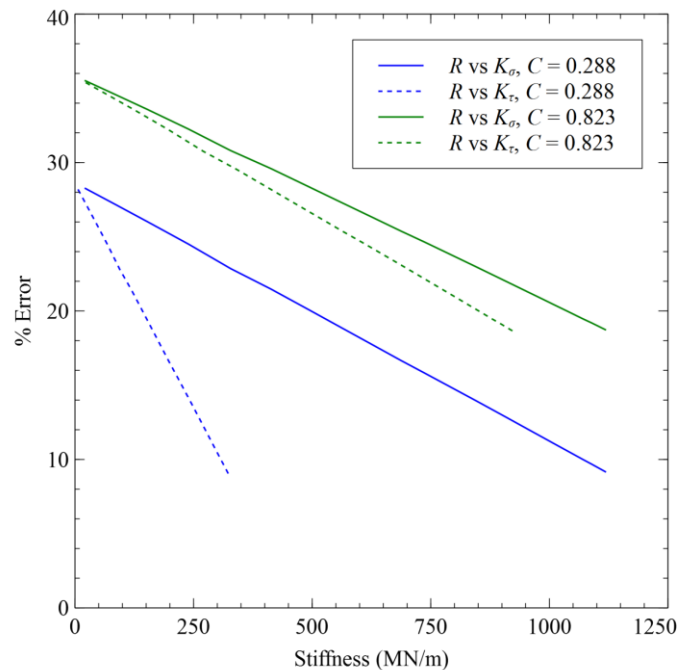
Fig. 6.16 Errors as a function of stiffness at different C

6.6 Discussion

Comparisons between all cases of simulated and analytical predictions have consistently shown that both methods have similar qualitative behaviour for every parameter compared at different contact conditions. However, in all cases, the FE simulations result in a higher predicted reflection coefficient.

Quantifying the differences in predictions in the form of percentage errors have revealed that the errors are influenced primarily by stiffness (K_σ and K_τ) and stiffness ratio (C). The errors decreases as stiffness was increased and stiffness ratio was decreased (Fig. 6.16). An implication of this is that interfaces where the stiffness is low such as that of rougher contacts experience a greater discrepancy in the predicted reflection coefficients.

The oscillations that occur when calculating R (Fig. 6.11) is a feature that has not been observed both in the analytical model or in the experiments performed in the next chapter, implying that it could be an error caused by simplifications used when modelling the contact interface in COMSOL. This may also explain the quantitative

differences seen in the results between the two methods (analytical and simulations). For example, in the interest of having an optimized solution time with good accuracy, the dimensions of the geometry were downsized. This could potentially lead to near field effects resulting from points A and B in Fig. 6.10. One way to overcome this is to perform the simulations on a model with a much larger distance between A and B. However, doing so increases computational time, even for the simplest of cases unless the capabilities of the hardware are improved upon.

Although the case where different contact pairs (e.g. aluminium-steel contact) have not been examined here, it is clear that changing the material of the contacting cylinder results only in a change of contact stiffness which can then be used to determine resulting reflection coefficient by using Fig. 6.15. More generally, the plots in Fig. 6.15 represent a convenient way from which either R or $K_{\sigma, \tau}$ can be determined so long as either one of them is known.

Note however that the results shown in Fig. 6.15 apply only to a steel half-space. Similar plots can be generated for a half space made out of different materials by performing calculations on a half space with the corresponding materials.

6.7 Conclusions

In this chapter, a finite element study of the interaction of Rayleigh waves with a contact interface was performed. A simple 2D linear elastic model was used to represent the geometry of the problem. The contact interface was modelled as a discrete point on the free surface of the geometry characterised by both K_σ and K_τ. A continuous sinusoidal input was applied in order to excite Rayleigh waves in the model. Both perfectly smooth and rough cases were studied by varying K_σ and K_τ at the interface.

The results were compared with the analytical model proposed in Chapter 5. In all cases studied, both simulation and analytical results have been shown to agree well qualitatively. Quantitatively, the simulations predicts a higher reflection coefficient, with errors ranging from approximately 9% to 36%.The errors are found to be a function of both stiffness and stiffness ratio, with errors decreasing with an increase in stiffness and decrease in stiffness ratio.

7 Experimental Measurements of Rayleigh Wave Reflections

The interaction of Rayleigh waves with a contact interface has been studied both analytically in Chapter 5 and by finite element simulations in Chapter 6. In this chapter, the experimental work conducted to verify results from the preceding chapters are detailed.

7.1 Experimental Layout

Fig. 7.1 shows how a line contact was generated by pressing a cylindrical rod onto a flat surface. A wedge transducer is used in generating the Rayleigh wave. The transducer was positioned so that the beam of Rayleigh wave is normally incident to the line contact, with the angle, θ_1 set at the Rayleigh angle for a Perspex-steel interface at 61.53^o (c.f. Table 3.1). A detailed documentation on the ultrasonic instrumentation involved is given in section 7.4.
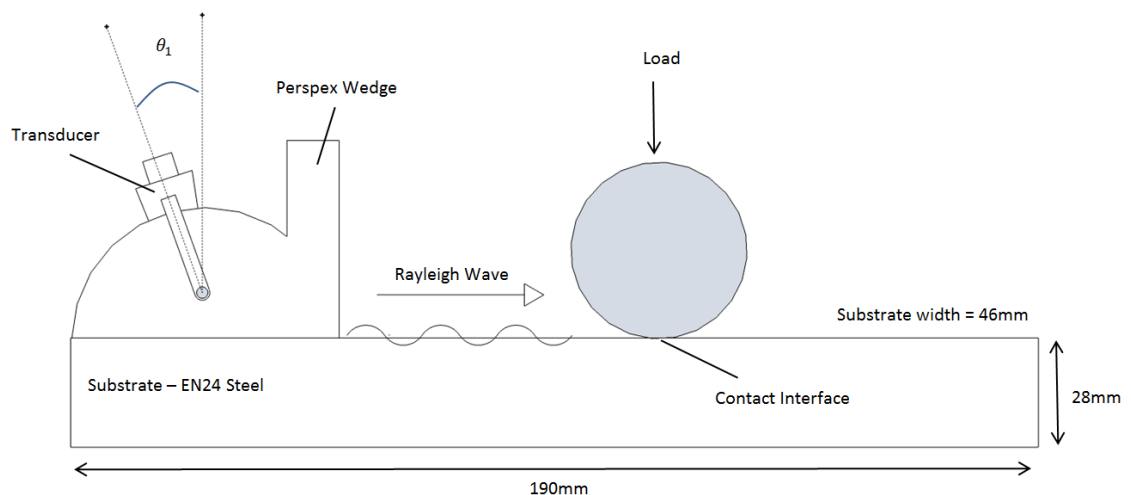
Fig. 7.1 Layout of the experiment

A cylindrical specimen was loaded on to the steel block to generate the line contact. The diameter of the cylindrical specimen was chosen such that the maximum contact width generated will be small compared to the wavelength of the incident Rayleigh wave. In the tests conducted, the diameters of the specimens vary between 9.5 mm to 10 mm.

Although no specific criterion were set for the half-space outside of the assumptions outlined in section 3.1, it is practical to use a common engineering material that is well understood with established mechanical properties. For this, EN24 steel was chosen as the material used to approximate the half space.

7.1.1 Determining the Minimum Thickness of the Half Space

As pointed out in section 3.5, the thickness of the EN24 steel used to approximate the half space has to be sufficiently thick to prevent the generation of Lamb waves. The thickness sufficient to unambiguously generate Rayleigh waves can either be determined using either the Lamb wave dispersion curves or equation (3.12).

Lamb wave dispersion curves specific to the experiments conducted here were calculated based on Rayleigh waves at 2.25MHz with properties of steel from Table 7.1 using equations (3.9) and (3.10). The results are shown in Fig. 7.2 (This is the same as Fig. 3.10 but repeated here for reading convenience). From the curve, it can be seen that the thickness has to be larger than 4 mm to allow both A_0 and S_0 wave modes to transform into Rayleigh waves.
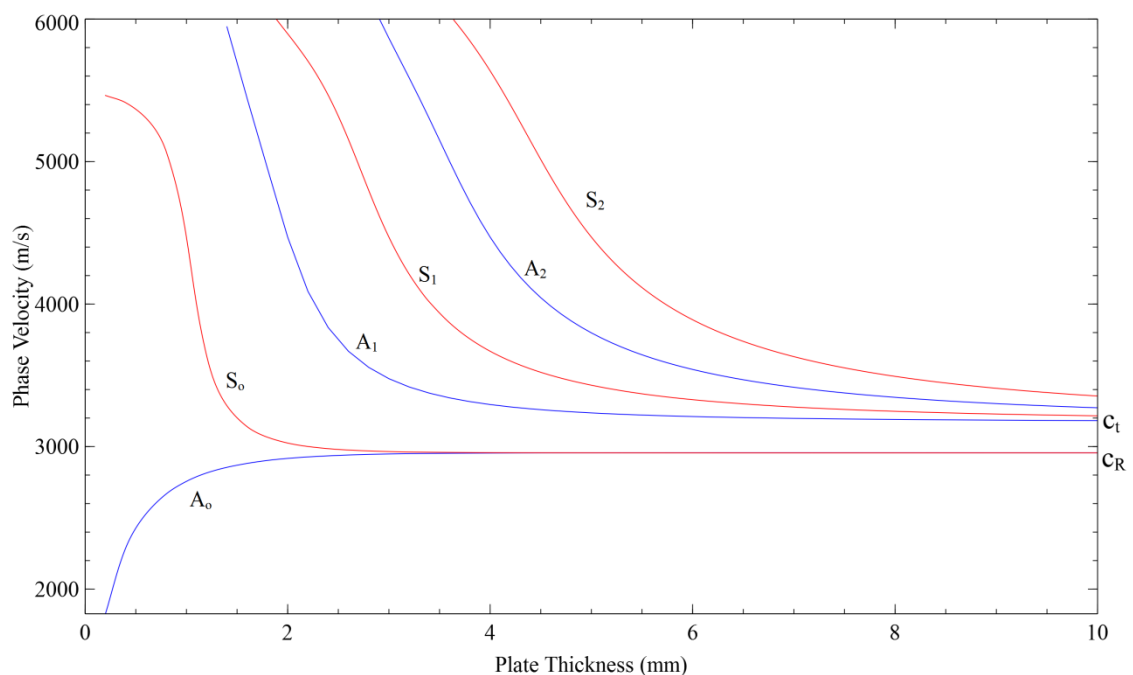
Fig. 7.2 Dispersion curves calculated for the experiments

In addition to using the Lamb wave dispersion curve, equation (3.12) was also used to determine the minimum thickness that is required to unambiguously generate Rayleigh waves. By using wave velocity data provided in Table 3.1, the relationship between M and the thickness of the substrate are plotted out in Fig. 7.3 using equation (3.12).

A conservative estimate for x where A_o and S_o behaves like Rayleigh waves was set at 500 mm (c.f. Fig. 3.11). This gives the condition that $M >> 385$ for a Rayleigh wave wavelength, λ_r of 1.3 mm. From Fig. 7.3, it can be seen that at thicknesses beyond 3mm, the condition that $M >> 385$ is readily fulfilled. In the experiments, the thickness of the EN24 steel used was 28 mm.
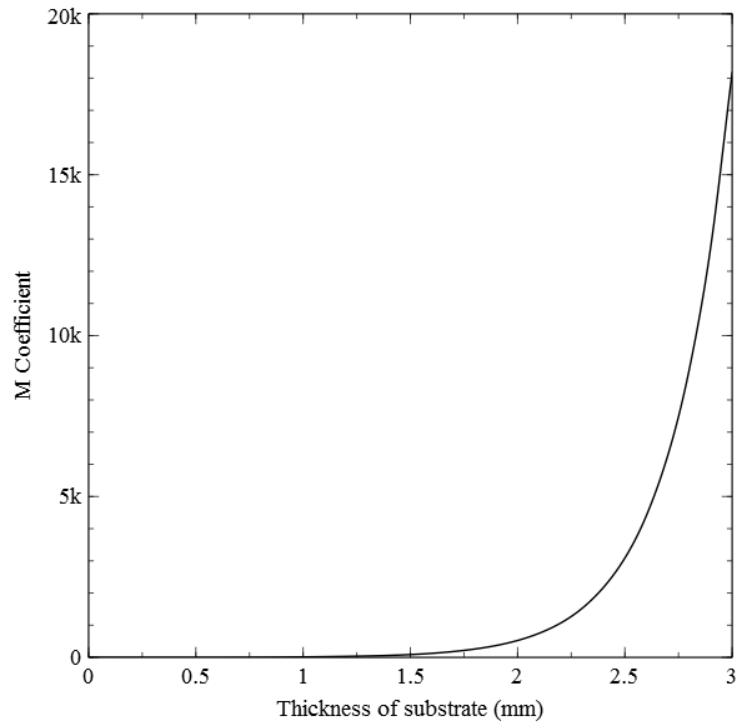
Fig. 7.3 *M* coefficient to determine minimum substrate thickness

7.2 Test Cases

Careful consideration was given in developing the type of test cases that would yield data that allows meaningful comparisons to be made against data from chapters 5 and 6. Consideration was also given to what can practically be achieved given the facilities available as well as whether the stimulus (change in load range, roughness of contact etc) introduced will cause a measurable change (i.e. a significant enough change in amplitude).

Two types of tests were chosen. One in which the roughness of the contact interface is varied and one in which the pairs of materials at the contacting interface was varied.

7.2.1 Tests with Varying Roughness
In this test, cylindrical specimens made out of steel were used. The elastic properties of steel are given in Table 7.1.

Table 7.1 Properties of the materials used (Callister & Rethwisch 2011, Efunda n.d., Knovel 2014, Theplasticshop.co.uk 2005)

Parameter	Steel (EN24)	Aluminum (6082)	Brass (CZ121)	Copper (C101)	Perspex
E (Young's Modulus)	210 GPa	69GPa	97GPa	117GPa	2.74GPa
v (Poisson's Ratio)	0.3	0.33	0.34	0.34	0.39
D (Specimen diameter)	10 mm	9.5mm	9.5mm	9.5mm	10mm
G (Shear modulus)	80.7 GPa	26GPa	36.2GPa	43.6GPa	0.986GPa
ρ (Density)	7850 kg/m^3	2685 kg/m^3	8470 kg/m^3	8800 kg/m^3	1180 kg/m^3

The roughness of each specimen was produced by wet sanding each specimen on a lathe with different grades of abrasive paper. Care was taken to ensure that the roughness of the specimen was homogeneous as much as possible. The steel specimens that were prepared are shown in Fig. 7.4.

Fig. 7.4 Steel specimens

In the case of the steel block (i.e. the substrate), two different roughnesses were prepared. In the first instance, the steel block was grounded using a surface grinder to produce a flat surface. The grounded surface was used in the first series of tests. The same steel block is then polished to a mirror finish to produce a much smoother contact and the same series of tests were conducted. The polishing process was performed by wet sanding the surface of the steel block with progressively finer grits of sandpaper until a mirror finish was achieved.

The roughness of the specimens and the steel block can be obtained by using a stylus profilometer (SURFTEST SV-600) manufactured by Mitutoyo. The resulting measurements for both root mean squared roughness (σ) and centre line averagess (R_a) are shown in Table 7.2.

Table 7.2 Roughness properties for the series of tests conducted

	σ (µm)	R_a (µm)
Specimen 1 (Steel)	0.071	0.05
Specimen 2 (Steel)	0.112	0.081
Specimen 3 (Steel)	0.130	0.092
Specimen 4 (Steel)	0.177	0.138
Brass	0.08	0.056
Copper	0.109	0.082
Aluminium	0.21	0.112
Perspex	0.142	0.072
Steel Block (Grounded)	1.179	0.950
Steel Block (Polished)	0.094	0.071

In this way, the combined roughness at the interface can be varied by cycling through the contact pairs. It should be noted that with repeated testing, the roughness of the specimens and the steel block will change as the asperities are flattened out. To avoid this, both the steel block and specimens were touched up when necessary with their respective finishing operations.

7.2.2 Tests with Different Material Combination

Different material combinations were tested by varying the material of the cylindrical specimen while keeping the material of the substrate unchanged. Aluminum (6082), brass (CZ121), copper (C101) and perspex were chosen due to their availability and widespread usage, together with a large enough spectrum in mechanical properties in order to see differences in the amplitudes of the reflected waves.

Fig. 7.5 The different materials used.

The properties of the materials listed are given in Table 7.1. Testing of the materials was performed with the polished steel block. Each of the specimens was polished to a mirror finish by wet sending with increasingly finer grits of abrasive paper. However, a final step where a commercial polishing compound (Brasso) was used was required to achieve a mirror finish, particularly in aluminium due to the softness of the material. The specimens used are shown in Fig. 7.5.

The roughness properties of the different specimens, measured with a stylus profilometer is shown in Table 7.2.

7.3 Loading of the Specimens

Loading of the specimens was achieved using a tension-compression machine manufactured by Tinius Olsen (Model H25KS). The schematic of the testing machine is shown in Fig. 7.6. The main mechanism through which the load is applied is via

actuators that move the crosshead vertically up or down. The machine used has a capacity of up to 25kN. A load cell is attached to the cross head to measure the loads applied.
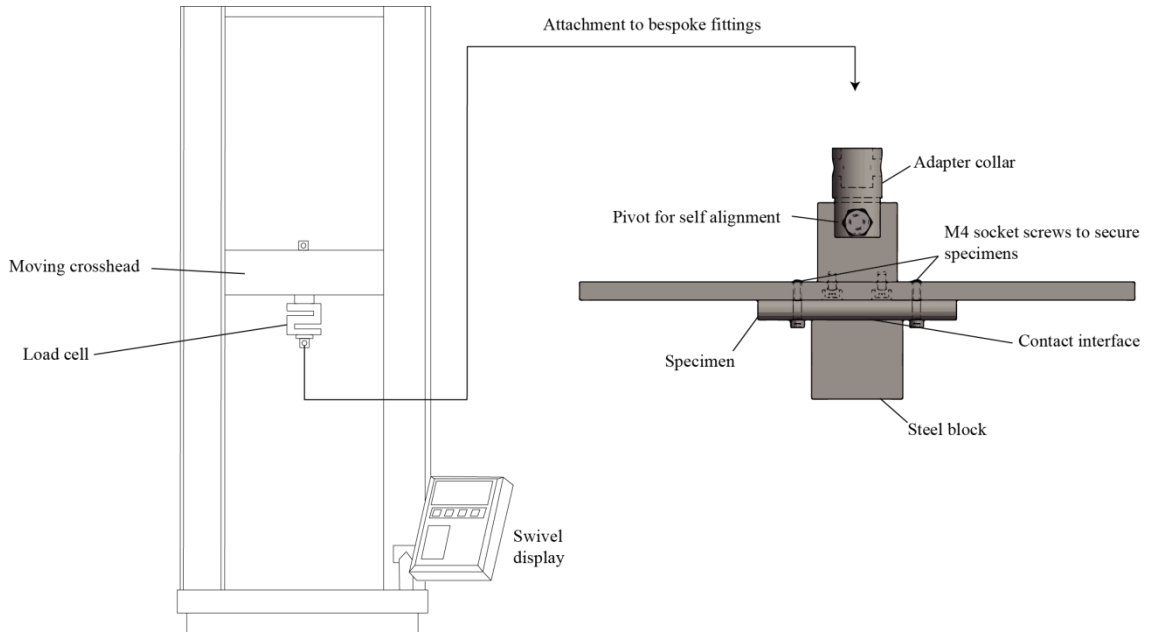
Fig. 7.6 Loading apparatus

Bespoke fittings were required for the experiments. The design of the attachments is shown in Fig. 7.6. The function of the pivot is to allow self alignment of the specimen to the surface of the steel block. The specimens are secured to the adapter via two M4 socket screws. Fig. 7.7 shows an actual image of the experimental rig.
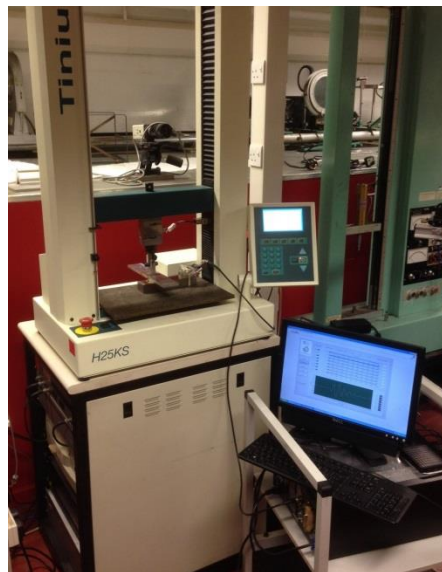
Fig. 7.7 Image of the experimental rig

The nature of the load applied by the crosshead can be controlled via a PC unit attached to the testing machine. A loading-unloading cycle was used to examine the difference that may occur during loading and unloading of the interface. Fig. 7.8 illustrates the loading-unloading sequence used in the experiments.

Apply small preload -10N

Apply loading at a rate of 1.5 mm/min

Load reaches predetermined maximum. Hold untill unloading sequeunce is initiated.

Begin unloading sequence at 1.5 mm/min

Load reaches original preload (10N) - hold load level until stopped by operator or the next cycle iniatiated

Fig. 7.8 Loading sequence applied during testing

First, a small preload of 10N was applied. Next, the crosshead was set to move/ compress at a rate of 1.5 mm/min. This gives a slow rise in the applied force, allowing enough time to obser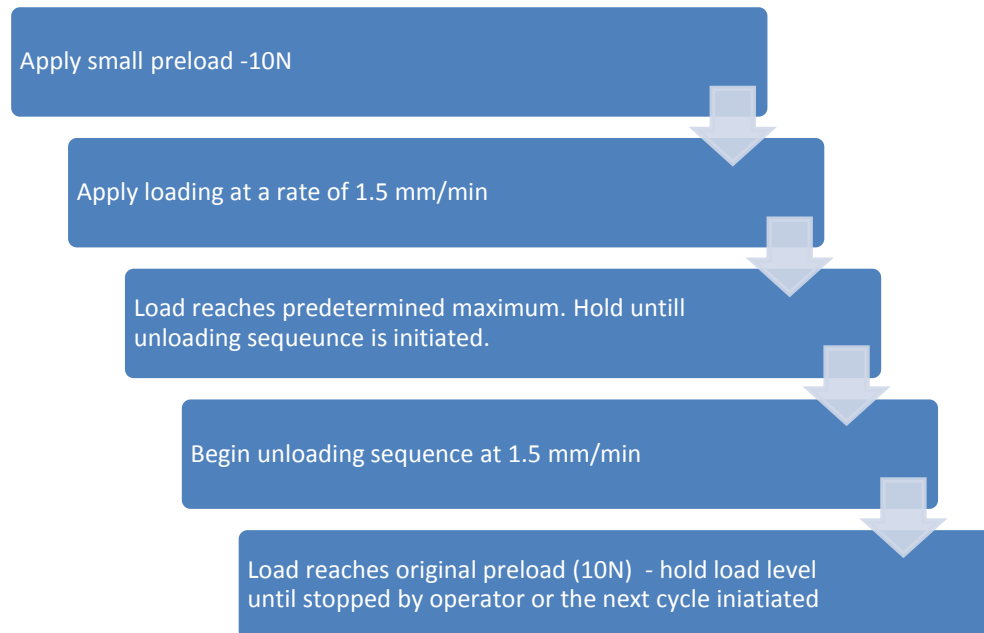ve any changes to the reflection coefficient. When a predetermined maximum load is reached, the testing machine holds the loading level for at least 15 seconds before the unloading sequence begins.

The unloading sequence takes place at the same rate at which the loading occurs. Once the load reduces to the preload, the machine is set to hold the loading levels at preload until an operator terminates the sequence or the next loading-unloading cycle is initiated.

The reason for maintaining the preload between each cycle is to ensure that the same asperities are in contact for all load cycles. For all the tests conducted, three loading-unloading cycles were performed.

The maximum load differs depending on the material of the cylindrical specimen. They are determined in such a way as to ensure that the load does not grossly exceed the yield point. This allows observation of the reflection coefficients over a large range of force while maintaining the elastic assumption. The calculation is based on Hertzian contact

theory for line contacts. Table 7.3 gives the maximum load applied to the different types of specimens used in the tests conducted.

Table 7.3 Load threshold for the different specimens

Material	Compressive Yield Strength	Diameter	Maximum applied load	Maximum applied stress
Steel	680 MPa (Steel-Express n.d.)	10mm	2400N	619MPa
Brass	360 - 580 MPa (Aalco 2014a)	9.5mm	1200N	360 MPa
Copper	200-400MPa (Aalco 2014b)	9.5mm	1200N	383 MPa
Aluminium	306 – 322 MPa (Yibo et al. 2013)	9.5mm	1200N	311 MPa
Perspex	63.4 MPa – 75MPa (Callister & Rethwisch 2011; Ltd 2008)	10mm	1200N	73 MPa

While loading takes place, the changes in load are saved to allow correlation with the ultrasonic data. An example of the load history is shown in Fig. 7.9 for a steel specimen for a single cycle.
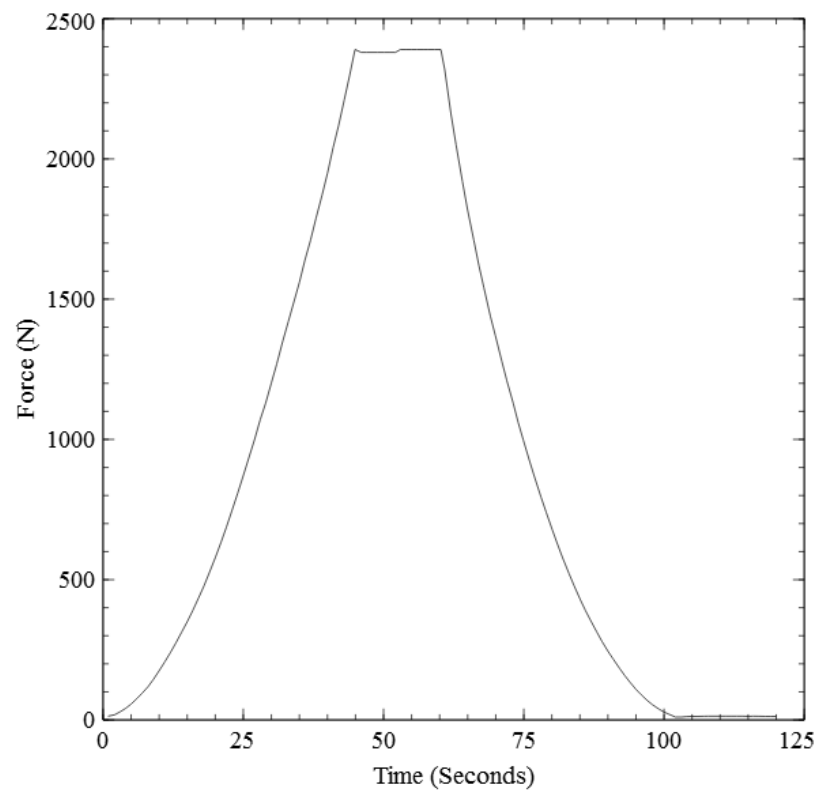
Fig. 7.9 Load history for a steel-steel contact

7.4 Ultrasonic Instrumentation

The ultrasonic system used is shown schematically in Fig. 7.10. Generation of the Rayleigh waves is done using a variable angle wedge transducer (Fig. 7.1). The variability of the angle of the wedge allows 'tuning' of the wedge to generate the maximum amount of Rayleigh waves. The transducer has a centre frequency of 2.25MHz and operates in pulse-echo mode.

A standard consumer computer was fitted with specialized data acquisition and ultrasonic hardware. This allows the transducer unit to be driven 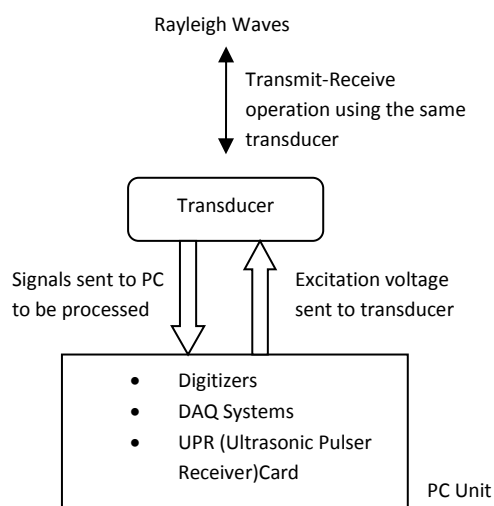directly from the PC. Analog to digital convertors (digitizers) convert the analog signals from the transducer into digital format to allow the computer to process the signals. In the same way, digital command signals are converted into analog form to energize the transducer.

Fig. 7.10 Schematics of the ultrasonic system used in the tests

Programs written in the LabVIEW[3] (version 8.1) environment were used to allow communication between the various hardware involved. In addition, recording of the ultrasonic signals and subsequent data processing are also handled using LabVIEW.

An excitation signal of 100V was applied to the transducer at a rate of 160Hz. This means that 160 signals are sent down the substrate each second. Each of the signal forms a single 'frame' or scan (e.g. Fig. 7.11) of the travelling waveform which are stored and analysed in the post-processing stage. In this way, a real time recording of the reflected pulse can be recreated during post processing.

Coupling between the transducer and the steel block was achieved using viscous mineral oil. To maintain a constant coupling force and avoid drifting of the transducer, an elastic band was used to secure the transducer to the steel block. The transducer is

---

[3] LabVIEW is a graphical programming software used here for it's strength to communicate between various pieces of hardware. In addition, post processing tasks such as signal and data analysis can be performed using this software

positioned in such a way as to allow the generated pulse to travel straight along the length of the steel block.

Even with the precautions taken to ensure the similar coupling conditions between the ultrasonic wedge and the substrate, variations in the transmitted pulses still occurs each time the experiments are set up. This is likely due to minute variations in both the positioning as well as amount of couplant used. For this reason, a reference pulse is taken for each loading-unloading cycle and reflection coefficients are thus calculated based on their individual reference pulses. In this manner, the effects caused by the variations introduced during set up are accounted for as they cancel off when reflection coefficients are evaluated since the effects of the variations are present in both the reference and reflected pulse.

7.5 Collection and Processing of Experimental Data

This section details the methods involved in data collection and processing.

7.5.1 Recording the Reference Signal

Before the start of each experiment, a reference signal was taken from which the reflection coefficient can be calculated. The reference signal also serves as way to single out the reflected pulse from all nominal pulses.
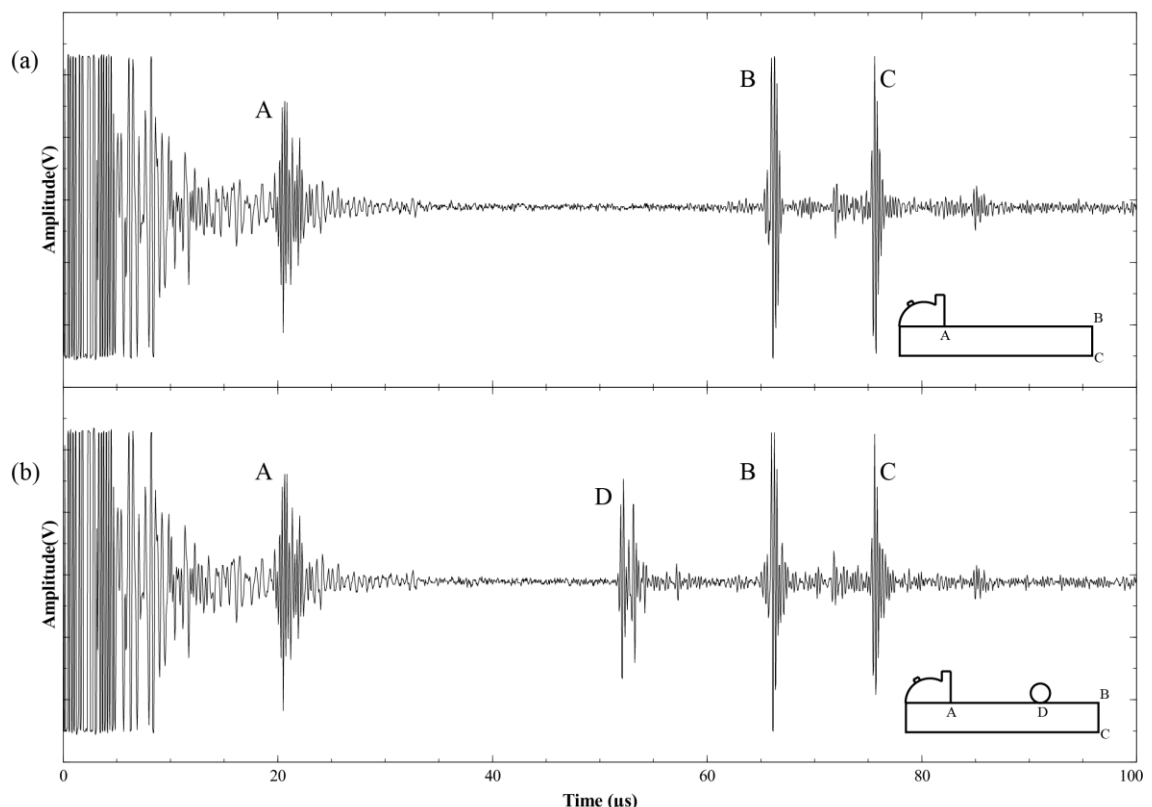
Fig. 7.11 Identifying reflected pules and recording the reference signal (a) Without specimen (b) With specimen

A signal is first sent down the steel block without any form of loading to obtain the reference signal. Fig. 7.11a shows an example of how the data in time domain would look like. Nominal reflections occur at the wedge-steel interface (A), the first edge of the steel block (B) and the second edge of the steel block (C) which are indicated in the insert diagram.

When the specimen is loaded, the appearance of a reflected pulse, D is evident in Fig. 7.11b. The location of each of the pulses can be cross checked with time of flight measurements to ensure that the interpretation of each pulse is correct.

The evaluation of reflection coefficients requires measurements of the incident pulse amplitudes at D (i.e. the reference pulse). There are two ways of achieving this:

1. Direct measurements using an identical transducer placed at D.
2. Estimating the incident pulse at D using reflections from a known geometry.

While it is desirable to use the first option, the variations introduced due to coupling effects are detrimental to the accuracy of the measurements and hence, the second option is utilized. The reflection coefficient from a geometry identical to the edge B has been studied numerically by Gautesen (2002). The results are summarized in Fig. 7.12.
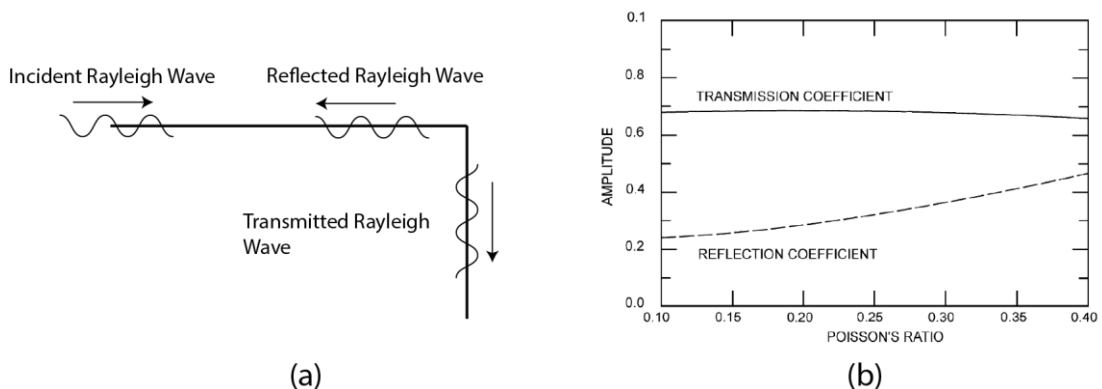
Fig. 7.12 Reflection from the edge of a quarter space (Gautesen 2002)

When an incident pulse strikes the edge of an elastic isotropic quarter space, both reflected and transmitted Rayleigh waves are generated as shown in Fig. 7.12a. The results by Gautesen have shown that both reflection and transmission coefficient are only a function of the Poisson's ratio of the material (Fig. 7.12b).

Since the Poisson's ratio for the substrate used (EN24 steel) is known to be 0.3, the reflection coefficient of Rayleigh waves from the edge, B can be estimated from Fig. 7.12b to be approximately 0.35 i.e. the edge, B reflects 35% of the energy of the incident Rayleigh wave. Hence, the incident amplitude at B can therefore be determined using the relationship below

$$Incident\ amplitude\ at\ B = \frac{Reflected\ amplitude\ at\ B}{0.35} \qquad (7.1)$$

Due to the effects of attenuation, the incident amplitude at B is lower than the incident amplitude at D. Fig. 7.13 illustrates this. Thus, the incident amplitude at D can be obtained by compensating for the amplitude lost through the effects of attenuation.
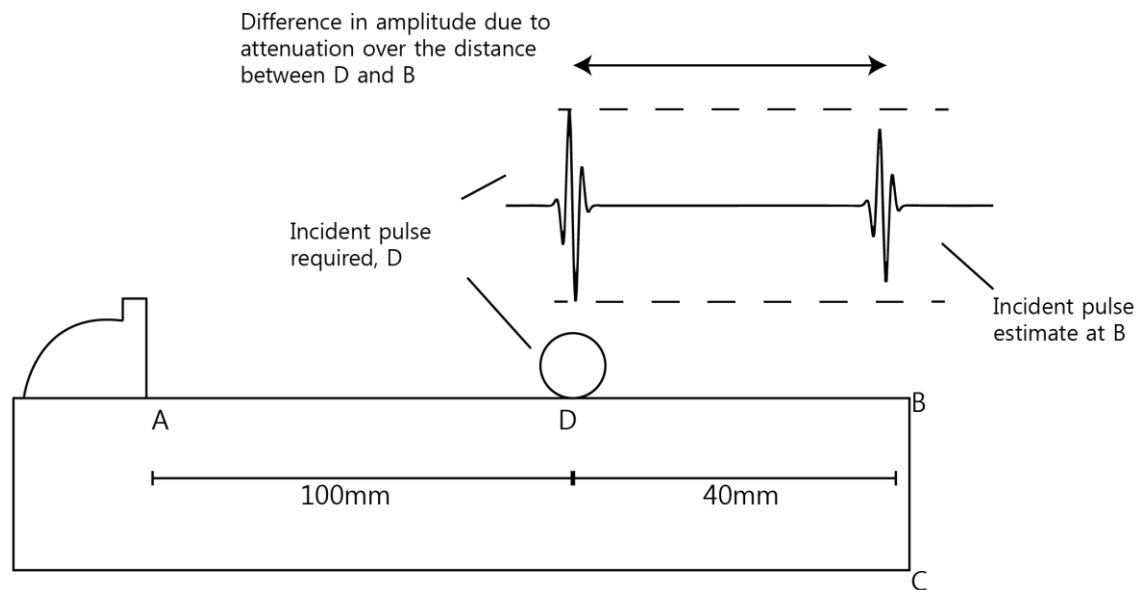
Fig. 7.13 Effects of attenuation when estimating incident pulse amplitude

7.5.2 Attenuation of Rayleigh Waves Due to Absorption and Scattering

It was shown in section 3.4.1 that the Rayleigh wave attenuation coefficients are linearly dependent on the attenuation coefficients of both longitudinal and transverse waves. In practice, accurate measurements of attenuation coefficient that specifically quantifies loss due to absorption and scattering are difficult to obtain due to the added losses from beam spreading and coupling of the transducers which are difficult to quantify.

Table 7.4 lists the longitudinal wave attenuation coefficients for various materials that have been measured where corrections has been made to account for effects of beam spreading and coupling effects.

Table 7.4 Attenuation coefficients for various types of steel

Material	Frequency	α Nepers/m
4150 Steel (Roderick & Truell 1952)	5MHz	~ 0.9
Stainless steel (Lerch et al. 2006)	6 MHz	~ 1
0.75% Carbon Steel (Kazuo 1957)	2.5MHz – 5MHz	~ 1-2
Chromium Molybedenum Steel (Kazuo 1957)	2.5MHz – 5MHz	~ 2
EN8 Steel (Darbari et al. 1968)	5MHz	1.6
EN45 Steel (Darbari et al. 1968)	5MHz	1.3

It can be seen that for materials with similar properties to the substrate (EN24 steel) at comparable frequencies, the attenuation coefficient is approximately 1 Neper/m. Thus,

an assumption is made based on available literature data that the loss between B and D is approximately 1 Neper/m. This results in a loss of approximately 8% in amplitude for a distance of 40mm between B and D.

7.5.3 Attenuation Due to Spreading of Rayleigh Waves

To calculate the effects of spreading on the amplitude of Rayleigh waves, equation (3.8) is utilised. The distance between D and B is 40mm. Thus, the spreading loss for the experiments conducted can be calculated to be (c.f. Fig. 7.13)

$$\frac{\text{Amplitude at } D}{\text{Amplitude at } B} = \sqrt{\frac{\text{Distance}, AB}{\text{Distance}, AD}} \tag{7.2}$$

The distances, AB and AD are measured to be 140mm and 100mm respectively. This yields a loss due to spreading between B and D of approximately 18%.

7.5.4 Evaluating the Incident Pulse Amplitude

The total loss due to effects of spreading, absorption and scattering is approximately 26% for the experiments conducted here. This means that

Incident wave amplitude at D $\times$ 0.74 = Incident wave amplitude at B

By substituting (7.1), the reference amplitude i.e. incident wave amplitude at D can be determined to be

$$\text{Reference Amplitude} = 3.861 A_B \tag{7.3}$$

Where A_B is the reflected pulse amplitude from B (Fig. 7.11a)
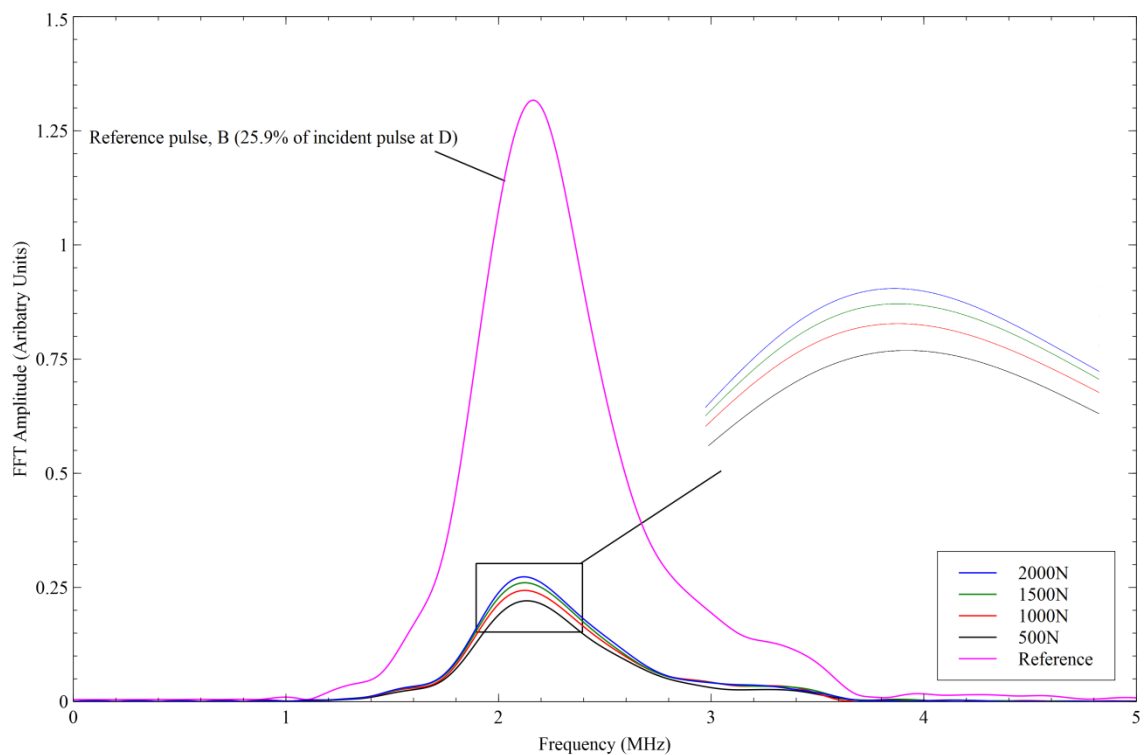
7.5.5 Evaluating Reflection Coefficient
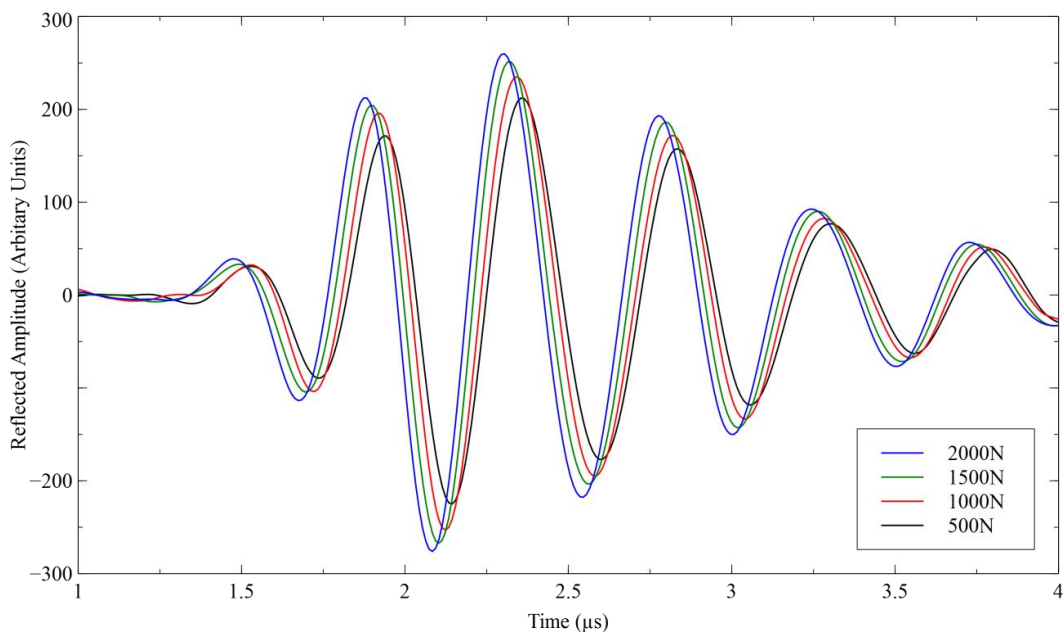
Fig. 7.14 Reflected pulses from the contact interface, D at various loads

Fig. 7.14 shows the reflected pulses extracted at discrete loading levels to illustrate how they change with load. A bandpass 2nd order Butterworth Filter with a sampling frequency of 100MHz was applied before hand to remove noise from the signal. The lower and upper cut-off frequency was approximately 2MHz and 4MHz respectively. The data shown in Fig. 7.14 is then converted into the frequency domain via application of the FFT (Fast Fourier Transform) algorithm.

Fig. 7.15 shows the data once they are converted into the frequency domain. It can be seen that each pulse contains amplitudes that lie across a spectrum of frequencies. Only amplitudes that remain within a bandwidth of -2.5dB are taken into account. In other words, amplitudes below 75% of the peak amplitude are discarded. This results in a frequency range of between 1.9MHz and 2.4MHz. Outside this bandwidth, the data becomes increasingly noisy and are thus discarded.

Fig. 7.15 Frequency domain of reflected pulses from the edge B and the contact interface, D

Each of the reflected pulses are then divided by the reference pulse and compensated for losses using equation (7.3) to obtain the reflection coefficient across -2.5dB. This is shown in Fig. 7.16 and it can be seen that over the range of the frequency considered, the reflection coefficient remains a constant. The slight waviness is attributed to electrical and background noise from the measuring apparatus.

The reflection coefficient can easily be converted to K_σ and K_τ by utilizing (5.35) and (5.36) provided that C is known. To illustrate, the conversion in Fig. 7.16 is done for C=0.288. Since the reflection coefficient is directly proportional to K_σ and K_τ, data for the stiffnesses can be represented by separate vertical axes.
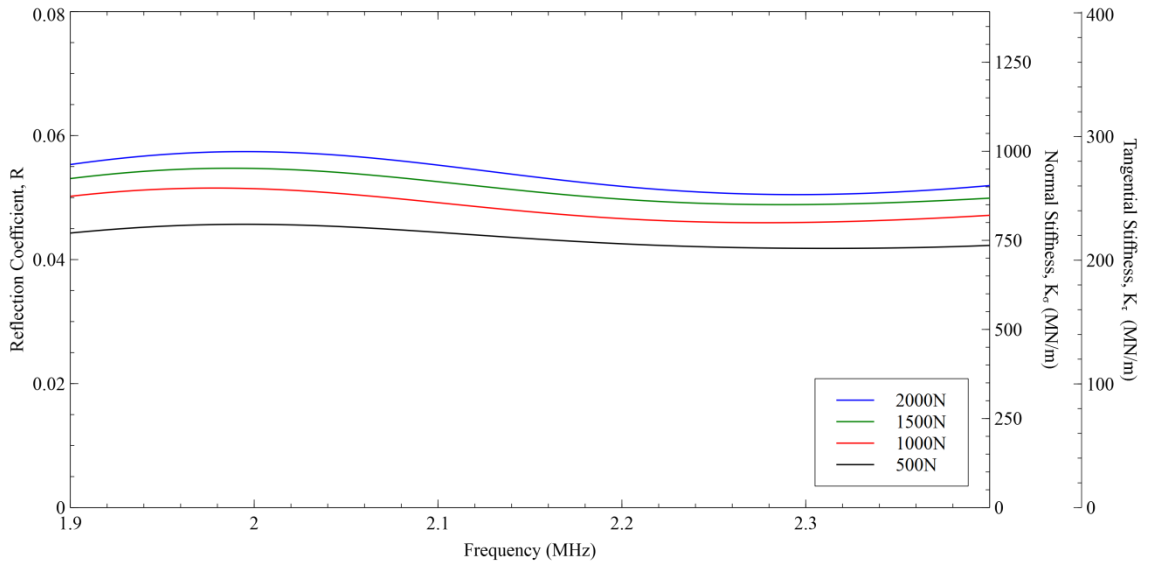
Fig. 7.16 Reflection coefficient and stiffness components at -2.5dB bandwidth

In the actual test, the pulses are recorded at a rate of 160 times per second. This result in over 10000 pulses recorded for each set of test that runs for approximately 100 seconds. Doing so allows the changes that occur during each loading-unloading cycle to be observed in a continuous fashion.

7.6 Results and Discussions

7.6.1 Tests at Varying Roughness
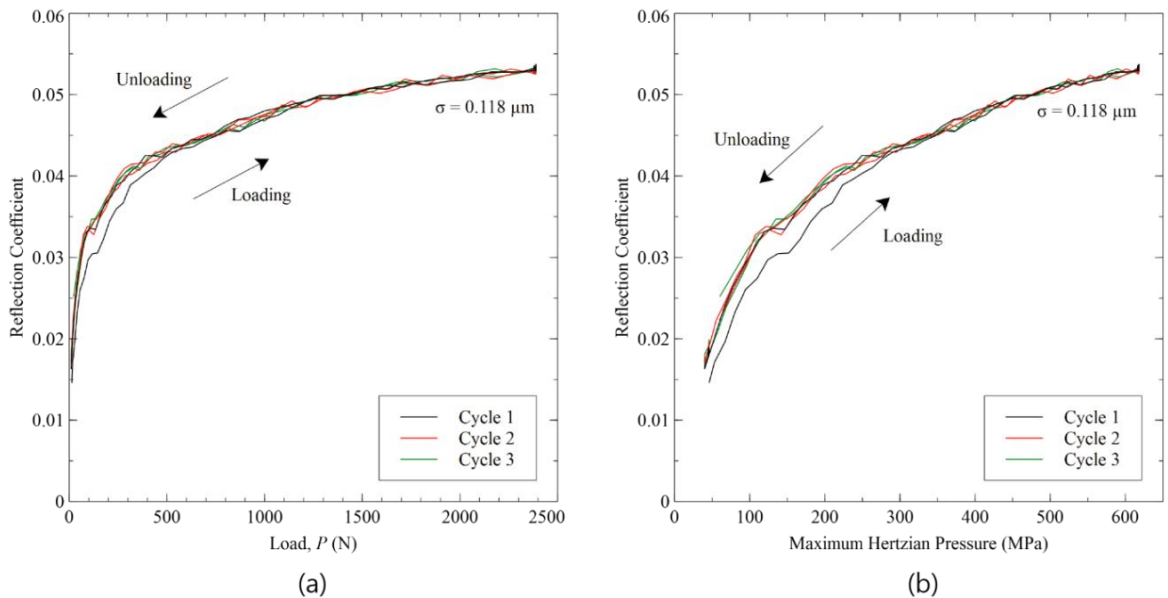
Fig. 7.17 Reflection coefficients for a line contact plotted against (a) load, P (b) maximum Hertzian pressure

Fig. 7.17 shows the reflection coefficient for a steel-steel contact with a combined roughness, σ of 0.118 µm. Three load cycles were applied according to methods

specified in section 7.3. It can be seen that irreversibility takes place in the form of hysteresis, evident in the larger loading loops formed in the first cycle. This is caused by the asperities undergoing plastic deformation as they are crushed due to higher local pressure at the asperity tips.

Subsequent loading cycles no longer behave in this manner, indicating that the asperities have undergone work hardening and thus are able to resist further plastic deformation i.e. shakedown has occurred. Similar phenomenon were observed in early work on ultrasonic bulk waves (Drinkwater et al. 1996; Dwyer-Joyce et al. 2001) where this hysteresis was attributed to irreversible adhesion at the interface.

Fig. 7.18 Comparison between a smooth and rough interface plotted against (a) load, *P* (b) maximum Hertzian pressure

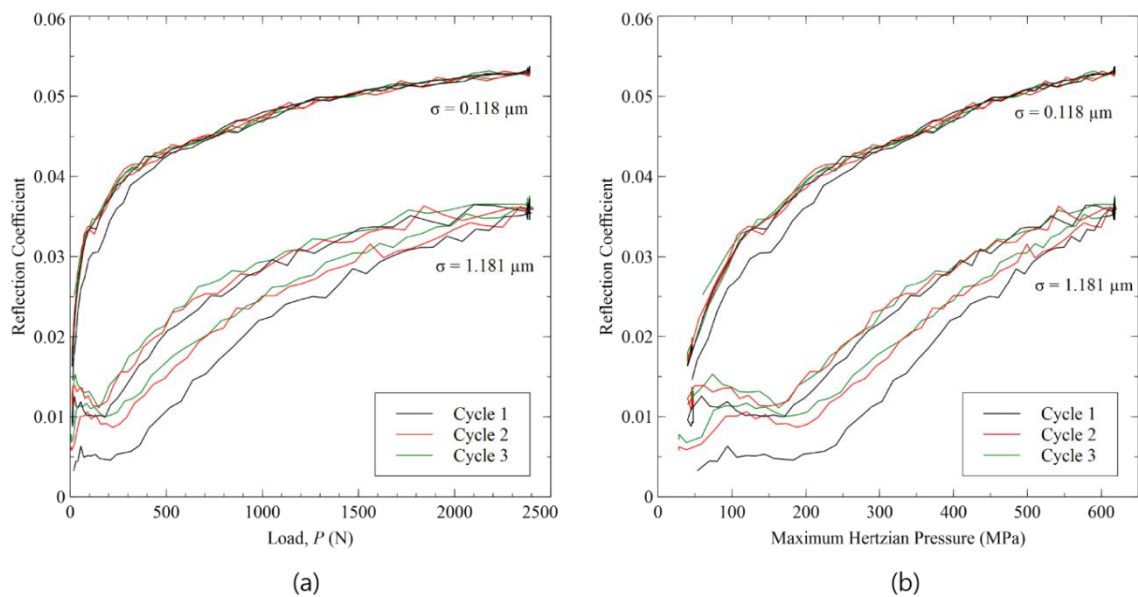The case for an interface where the contact is rough ($\sigma = 1.181$ µm) is shown in Fig. 7.18. It can be seen that when the interface is rough, the reflection coefficient decreases. Another difference is that the hysteresis loops formed for rough contacts are much larger compared to when the contacts are smooth. This is expected as rougher surfaces undergo more plastic deformation when pressed together.

The hysteretic behaviour in rough contacts persists beyond the first loading cycle. This suggests a repeatable irreversibility caused by an increase in roughness of the interface. It could be that due to the higher roughness, more of the asperities interlock and rub against each other as the load is cycled. The rubbing causes irreversibility in the form of friction.
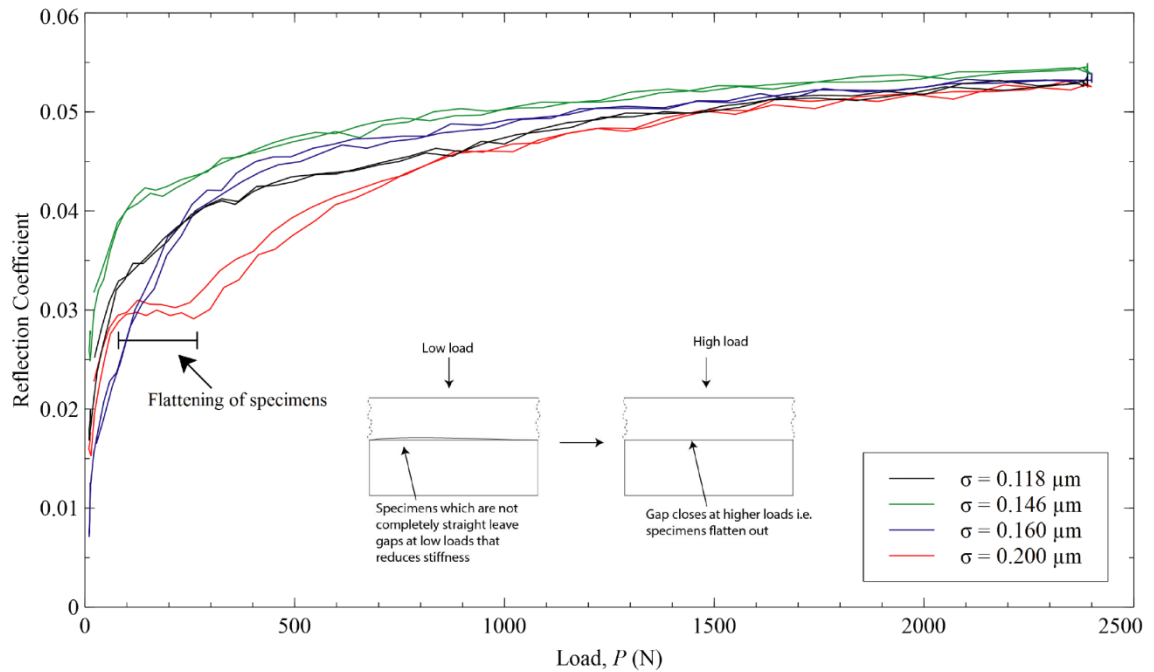
Fig. 7.19 Reflection coefficients from interfaces with intermediate roughness

Fig. 7.19 shows the results obtained with contacts of intermediate roughness between 0.118 µm to 0.2 µm. The results shown are cycle 3 of each test. Although the reflection does appear to decrease when the interface becomes rougher (at 0.2 µm), in general, there is no appreciable difference in the results obtained. This is likely due to the close proximity between the roughness of the interface, preventing any highly noticeable change to manifest in the reflection coefficient data.

In some cases, where the specimens were not perfectly straight along their axis, the contact area at low loads decreases due to the added curvature. This resulted in a lower reflection coefficient while flattening of the specimens takes place. This behaviour is illustrated in Fig. 7.19 and can also be seen to occur in Fig. 7.18 when the contact interface is rough.

7.6.2 Tests with Different Contact Pairs

To study the reflection characteristics of differing contact pairs, four different contact pairs were tested. In all cases, the substrate (i.e. the steel block) used remained the same while the cylindrical specimens were varied. Care was taken to ensure that the interface roughness formed by each contact pairs were similar to reduce dependencies of the results on roughness of the interface, allowing meaningful comparisons to be made based upon the differences in material properties. The properties of the interface formed by the contact pairs are given in Table 7.5.

Table 7.5 Interface properties for the various interface tested

Contact Pair	Combined roughness, σ (μm)	Combined Young's modulus, E'(GPa)
Steel-Steel	0.118	115.35
Copper-Steel	0.144	84.09
Brass-Steel	0.123	74.34
Aluminium-Steel	0.230	51.98
Perspex-Steel	0.170	3.19

Fig. 7.20 shows the results for the different contact pairs. Also shown are results for the smooth steel-steel contact from Fig. 7.17 with similar σ at 0.118 μm. It can be seen that R decreases with a decrease in E' of the interface. This agrees with observations made in the analytical model (Fig. 5.10). It can also be seen that the aluminium-steel contact shows considerable flattening effects.
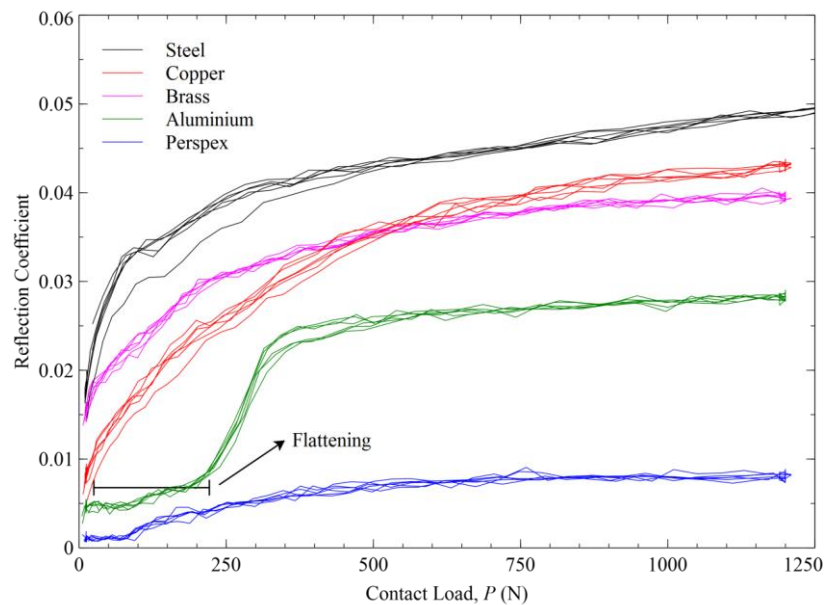
Fig. 7.20 Experimental results obtained from tests with varying contact pairs

Plotting R against E' in Fig. 7.21 reveals that the reflection coefficient is approximately a linear function of E', implying that interface stiffness is also a linear function of E'. This is in agreement with previous studies performed in developing stiffness expressions for a contact interface (Królikowski & Szczepek 1993; Mulvihill et al. 2013; Nagy 1992).
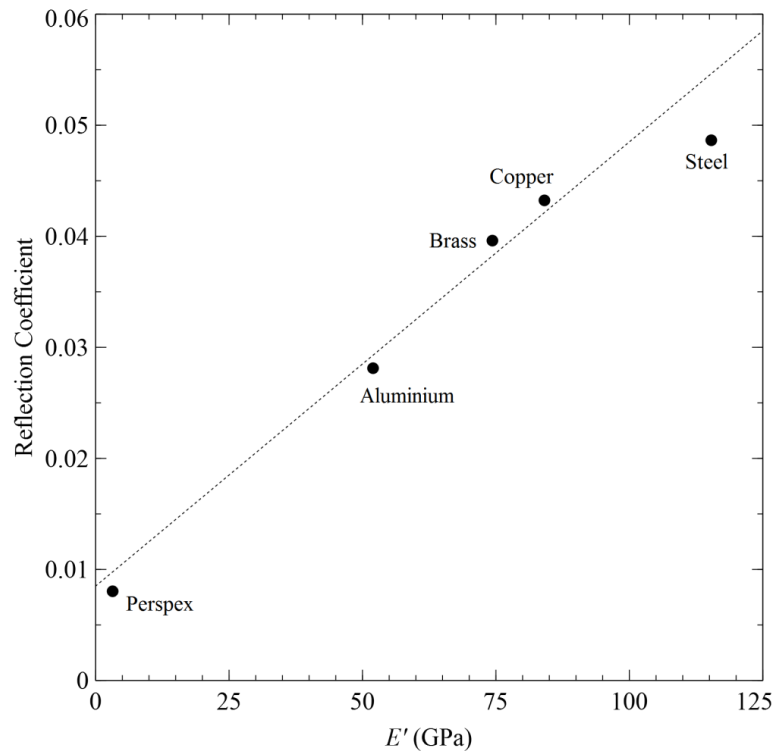
Fig. 7.21 R vs E' at 1200 N for different specimens loaded onto a steel surface

7.6.3 Comparison with Analytical and Finite Element Predictions

In this section, the predictions from both the analytical and finite element model are calculated and compared to experimental results. The roughness parameters required in calculating the analytical and finite element curves are approximated from profilometer measurements and are given in Table 7.6.

Table 7.6 β and η for each contact pair, approximated from profilometer measurements

Contact pair	Radius of asperity tip, β (μm)	Density of asperities, η (m^{-2})
Steel-Steel ($\sigma = 0.118$ μm)	43.78	3.53×10^{10}
Steel-Steel ($\sigma = 1.181$ μm)	10.5	6.16×10^{8}
Brass-Steel	12.67	5.74×10^{10}
Copper-Steel	11.41	4.62×10^{10}
Aluminium-Steel	31.56	3.01×10^{10}
Perspex-Steel	23.83	1.03×10^{10}

The predictions are calculated for stiffness ratio of C ranging from 0.288 to 0.8235 and thus appear over a range as an area instead of a single curve. Fig. 7.22 shows both analytical and COMSOL predictions overlaid on experimental data for a steel-steel contact, shown previously in Fig. 7.18.
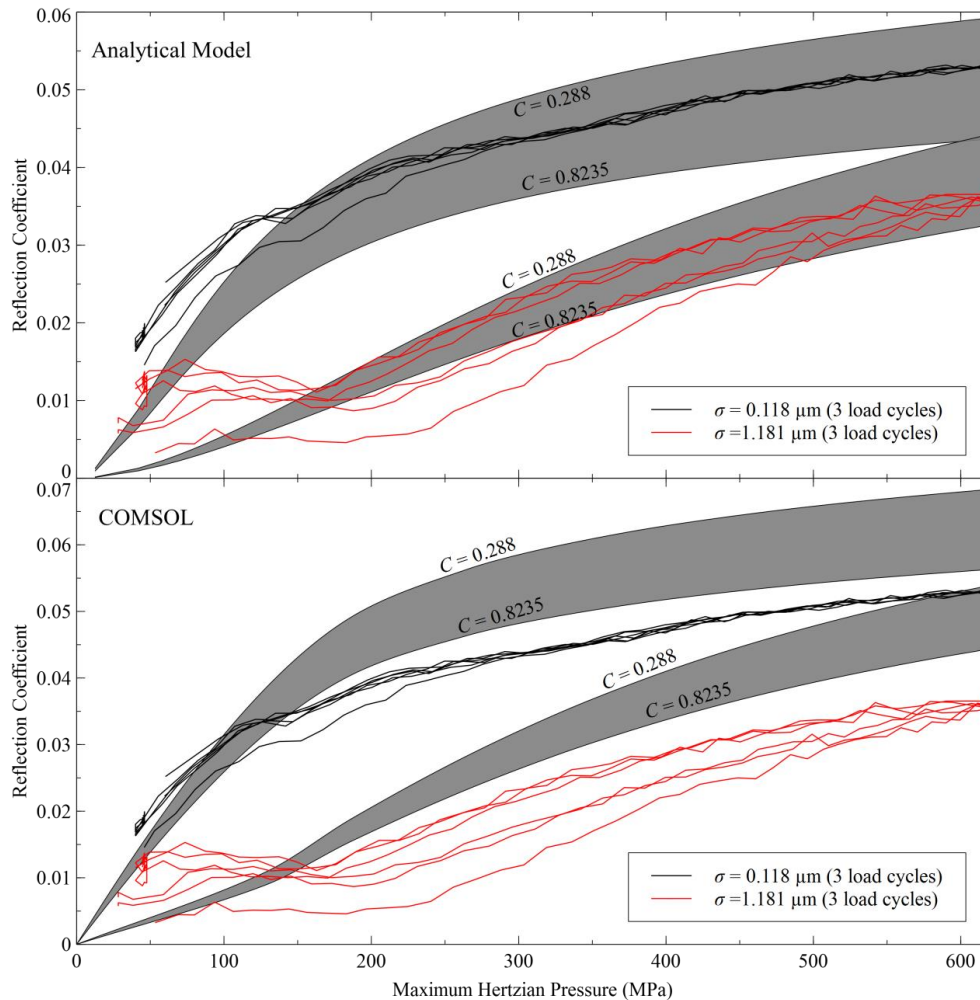
Fig. 7.22 Analytical and COMSOL (finite element) predictions compared to experimental data for a steel-steel contact

It can be seen that there is a good agreement among results obtained analytically, experimentally and from finite element simulations for both rough and smooth cases. Analytically, the experimental data appears to fall roughly midway between the limits of stiffness ratios used while FEA results predict higher reflection coefficients.

One source of error arises from the fact that in calculating the asperity stiffness, the theoretical (i.e. both analytical and FE) models assumes elastic deformation of the asperities. It is clear from the observed hysteresis loops that plastic deformation of the asperities takes places, causing deviations from both analytical and finite element models. The plastic deformation is less pronounced in the case of a smooth contact; hence the match is better in this case for the analytical model. Relaxation of full elastic assumption may allow the prediction of plastic effects, but at the cost of greater complexity in the theoretical models.

While the theoretical models are capable of tracking changes in interface roughness via a variation in contact stiffness, the models do not account for any roughness that might exist on the remaining free surface (i.e. the remaining free surface was implicitly assumed to be perfectly smooth). Studies have shown that in the presence of significant roughness, the Rayleigh waves will experience both dispersion (Tarasenko et al. 2003)

and attenuation effects (De-Billy et al. 1987). However, for the frequency and range of roughness used in this study, this effect is small and thus is thought to not have a significant influence on the experimental results.

Fig. 7.23 shows the comparisons made for tests performed with varying contact pairs. For contacts formed by metallic pairs, there is a good agreement between theoretical predictions and experimental data. As with the case of a steel-steel contact, reflection coefficient results predicted by the finite element method tend to be higher than both experimental and analytical results.

The exception here is in the case of a Perspex-steel contact, where both analytical and finite element predicts a reflection coefficient far lower than observed experimentally over the whole loading cycle. This could be caused by contact adhesion, an effect which was not accounted for in the theoretical predictions. Adhesion is known to effectively increase the contact area of surfaces in contact through interatomic attractive forces between the surfaces in contact (Johnson 1985), thus increasing the Rayleigh wave reflection by increasing contact compliance.

The effects of adhesion are generally small and thus the increase in R is likewise small. This is not significant in cases where R is high e.g. in steel-steel contacts, however, in the case of a Perspex-steel contact where R is low; the increase in R due to adhesion becomes significant and thus results in a reflection coefficient much higher than estimated by analytical and FE methods.

Additionally, rigid cylinder assumptions used in calculating asperity stiffness would not have been appropriate for comparatively soft materials such as Perspex. The Perspex specimen would have undergone significant deformation, resulting in a much larger actual contact area, increasing stiffness and hence reflection coefficient.
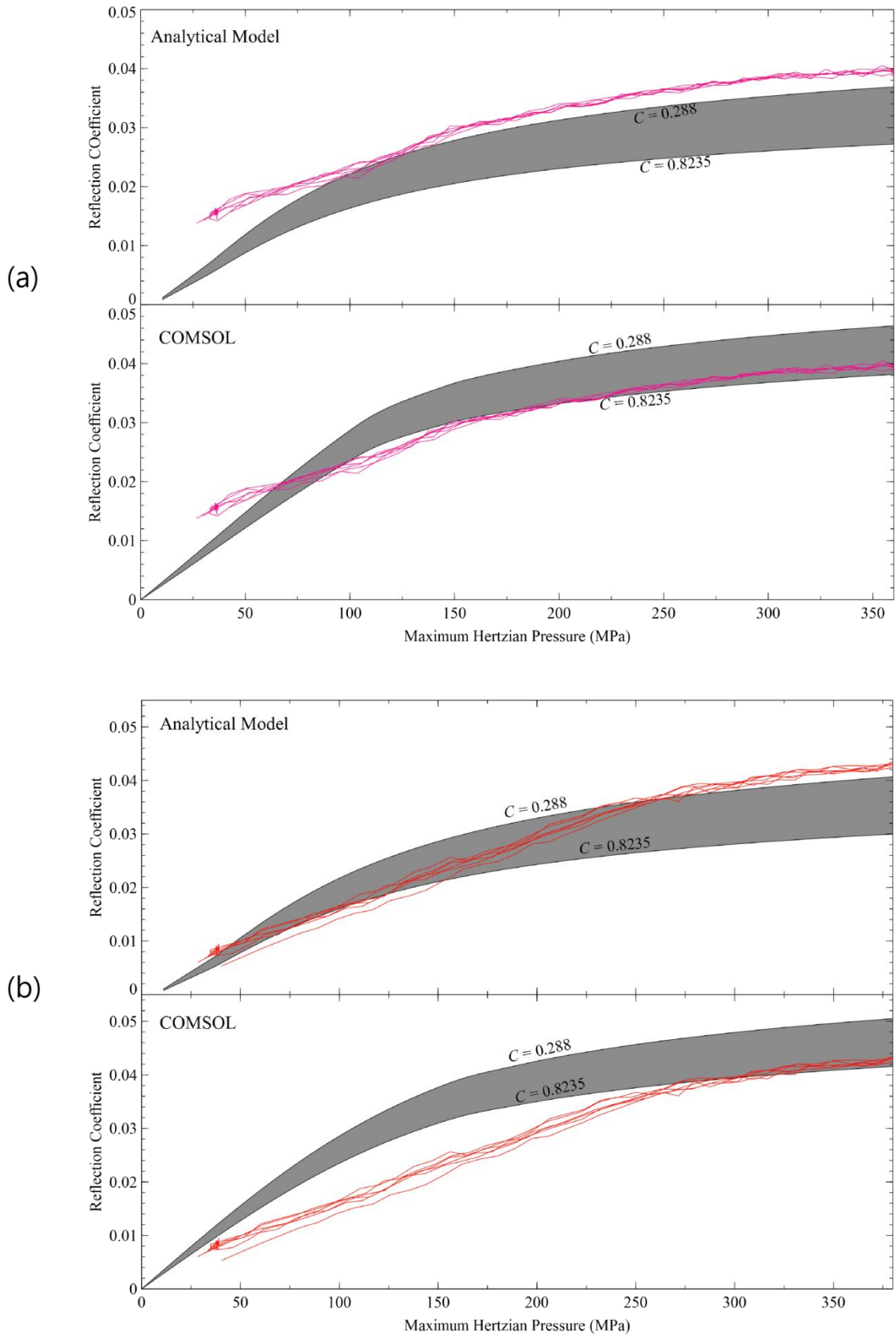
Fig. 7.23 Analytical and COMSOL (finite element) predictions compared to experimental results for (a) brass-steel contact (b) copper-steel contact
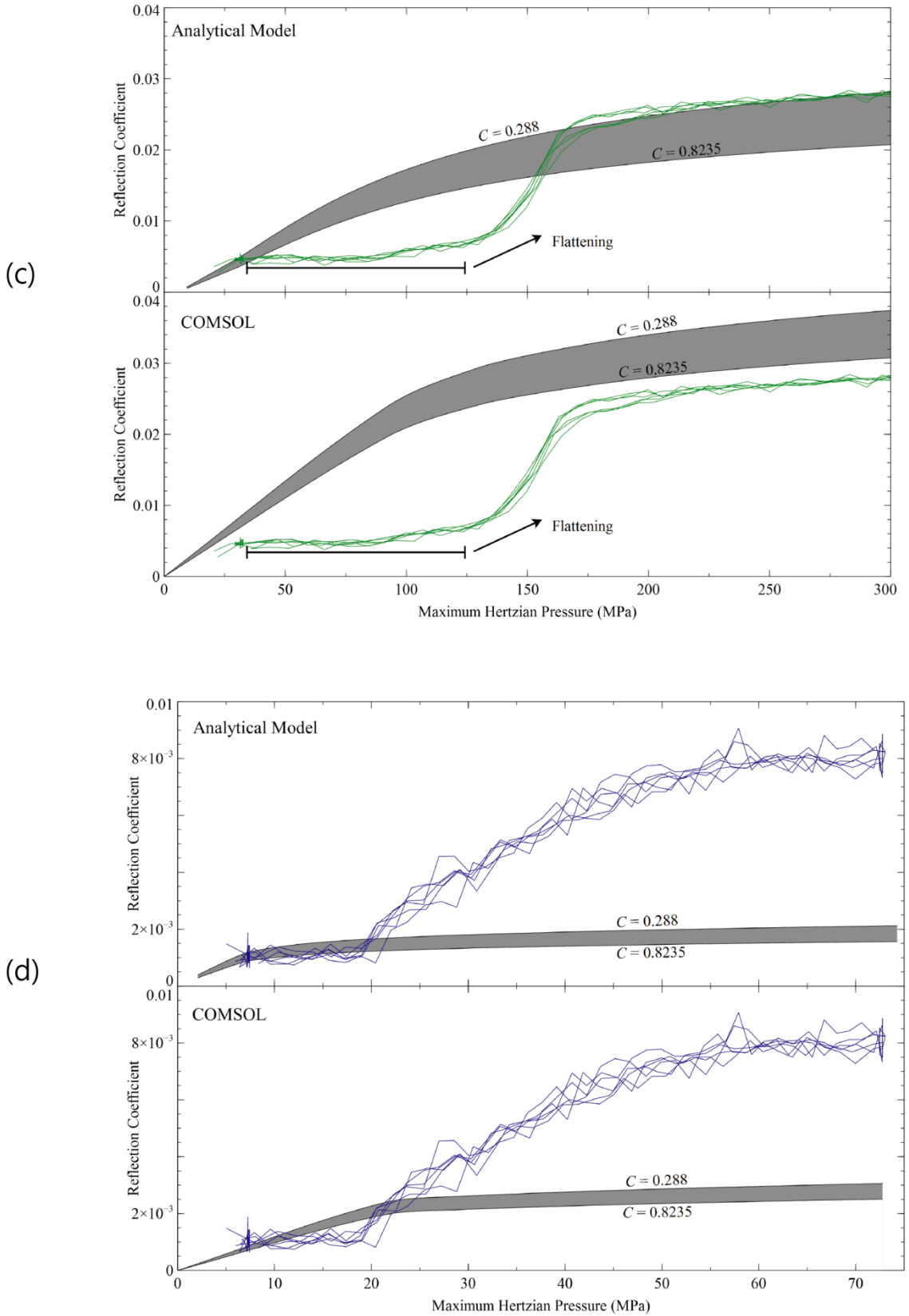
Fig. 7.22 (contd.) Analytical and COMSOL (finite element) predictions compared to experimental results (c) aluminium-steel contact (d) Perspex-steel contact.

Interface stiffness predictions from reflection coefficients

A useful feature of the analytical model developed is that it presents a convenient way of predicting interface stiffness from reflection coefficient measurements by using equations (5.35) and (5.36). The key parameter that is required to accomplish this task is the stiffness ratio of a particular interface. The analytical data was calculated based on the extremes of C established from literature (from 0.288 to 0.8235). The stiffness ratio for each specific experiment can be estimated by fitting the experimental data onto the shaded area of the analytical curves given in Fig. 7.22 and Fig. 7.23. Table 7.7 shows the resulting approximations. In this way, K_σ and K_τ of an interface can be determined by virtue of the Rayleigh wave reflection from an interface.

Table 7.7 Stiffness predictions based from reflection coefficients

Contact Pair	Approximate C from experimental data	K_σ and K_τ predictions based on R calculated from (5.35) and (5.36)
Steel-Steel (Smooth)	0.537	$R = 4.869 \times 10^{-11} K_\sigma$ $R = 9.067 \times 10^{-11} K_\tau$
Steel-Steel (Rough)	0.664	$R = 4.522 \times 10^{-11} K_\sigma$ $R = 6.806 \times 10^{-11} K_\tau$
Brass-Steel Aluminum-Steel Copper-Steel	0.288	$R = 5.548 \times 10^{-11} K_\sigma$ $R = 19.25 \times 10^{-11} K_\tau$

7.7 Conclusions

In this chapter, Rayleigh wave interactions with a contact interface were studied experimentally. The contact interface was generated by pressing cylindrical specimens onto a steel surface. The effects of varying roughness of the interface and using different material combinations were studied.

An increase in roughness reduces the overall reflection coefficient, with a clear increase in the size of the hysteresis loops when roughness is increased. The results obtain also suggests that R forms a linear relationship with E'.

The results obtained experimentally agreed well when compared to both analytical and finite element models. Errors become significant at low R values due to adhesion effects.

8 Application to Condition Monitoring of Lip Seals

Lip seals, alternatively also known as oil, radial or shaft seals are common engineering components that are used for sealing the interface of rotating machineries. This chapter details pilot work done in exploring ways where Rayleigh waves can be applied as a condition monitoring tool to monitor failure of lip seals.

8.1 Background

Sealing is an integral part of machineries that require strict lubrication conditions to properly function. The function of a seal is to prevent both lubricant leakage and ingress of unwanted contaminants into the lubricated systems.

A lip seal is used to seal the interface of a rotating shaft. The earliest form of a rotary seal was made out of leather (Brown 1995). Over the years, improvement in materials and an understanding of how lubrication affects the operation of this type of seals has greatly improved the performance and reliability of a modern day lip seal.
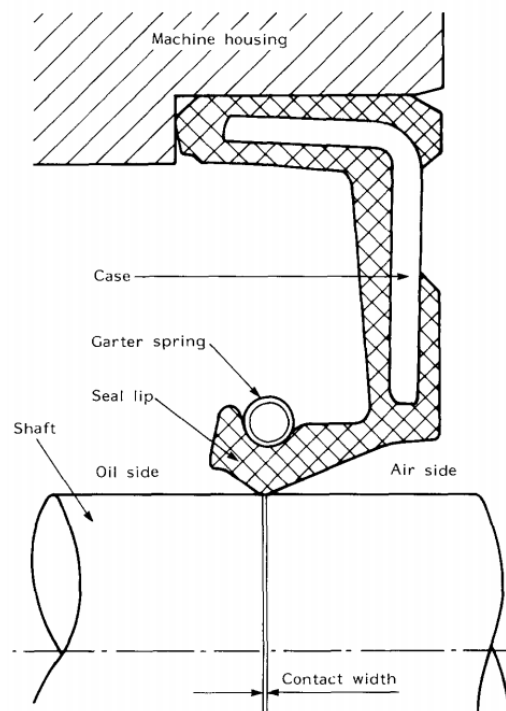
Fig. 8.1 Structure of a conventional lip seal (Stakenborg 1988)

The essential features of a conventional lip seal are shown in Fig. 8.1. The lip seals are fitted onto a housing by way of interference. This holds the seal in place, ensuring that they do not spin together with the shaft. The bulk of the lip seal is commonly made out

of some form of synthetic rubber, modified for specific applications. The rubber is moulded onto a metallic casing to add rigidity to the body of the seal.

Contact with the shaft is maintained via the elasticity of the lip itself. Garter springs are sometimes added to maintain the contact. Though the design of the lip seals is surprisingly simple, the mechanism through which sealing is achieved is complex and only recently been properly understood.

Under regular operation, there exists a layer of lubricating film between the lip and the shaft in the sealing zone (Stakenborg 1988; Salant 1999). This is perplexing since the existence of a liquid film in the sealing zone would cause a leakage of the fluid. Though various propositions have been put forth to explain this phenomena, the current accepted view is that the lubricant is kept sealed via a reverse pumping mechanism (Salant 2010; Salant 1999; Baart et al. 2009).

The manner in which the reverse pumping mechanism takes place is illustrated in Fig. 8.2. The asymmetrical design of the lip seal plays an important role in allowing the reverse pumping mechanism to take place. As the shaft rotates, the asperities are sheared and displaced to form a collection of miniature wedges or micro vanes that drags the fluid into the sealing zone.
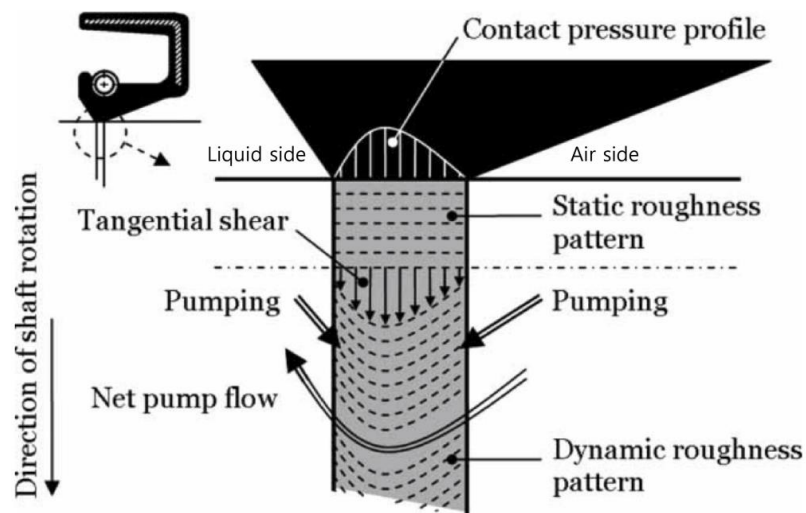
Fig. 8.2 The reverse pumping mechanism (Baart et al. 2009)

Due to the asymmetrical design, the formation of the vanes is uneven, with more vanes appearing on the air side. When the shaft rotates, the vanes on the liquid side will pump liquid out to the air side and vice versa for vanes on the air side. Since there are more vanes that are present on the air side, the net pumping action will be towards the liquid side, hence keeping the liquid sealed.

Although lip seals are generally reliable, failures can and still do happen. The critical area where failure often happens is at the sealing zone. In applications where unexpected seal failure and maintenance are costly affairs (e.g. offshore wind turbines),

it would be beneficial if some form of condition monitoring system can be applied in monitoring lip seals, particularly at the sealing zone (i.e. the seal-shaft interface).

Due to the manner in which the lip seals are installed, it is impractical to employ conventional ultrasonic waves due to the attenuative properties of elastomeric lip seal as well as the multiple interfaces that are often present in the housing of the sealing system. However, the manner in which Rayleigh waves works presents a convenient solution as Rayleigh waves can be made to travel down the axis of the shaft, directly reaching the sealing zone.

The goal of the work carried out here is then to explore ways in which a condition monitoring system based on ultrasonic Rayleigh wave principles can be applied to probe a lip seal system.

8.2 Seal Failure Modes

Lip seals can fail in many different ways. Common lip seal failure modes are detailed in Table 8.1 together with the possible causes.

Table 8.1 Lip seal failure modes (Brown 1995; Austin et al. 1979)

Failure Mode	Causes
Excessive Leakage	• Improper installation methods leading to misalignments and damaged seals • Insufficient sealing pressure/ low interference force • Lip overload • Seal operated in wrong direction i.e. air/ oil side facing the wrong direction
High temperatures	• Lubrication starvation at the sealing zone leading to high frictional forces • Excessive preload • Excessive pressure
Excessive wear in both shaft and seal	• Ingress of dirt and contaminants either in lubricant supply or from the atmosphere • Excessive operating temperature • Excessive pressure and load • Sealing zone starved of lubrication, leading to direct contact between seal and shaft
Seal hardening / cracking	• Long term exposure to harsh operating conditions • Chemically incompatible lubricant being sealed. • Excessive temperatures accelerates hardening

# 8.3 Measuring Seals Misalignment Due to Cocking[4]

A common cause of failure in lip seals occur when the installation of a lip seal is not performed correctly. This can result in, among many other things, a situation which is termed a 'cocked' seal. An example of a cocked seal is shown in Fig. 8.3.

When this happens, the seal appears to be slanted at an angle, the degree of which depends on how severe the cocking is. During operation, if a seal is cocked, it causes uneven wear in the lip of the seal, leading to regions of higher stresses which in turn lead to higher temperature. All of this causes early failure of the seals.

In this section, a method of assessing seals misalignment due to cocking via the use of reflected Rayleigh wave is presented.

8.3.1 Working Concept

Fig. 8.3 illustrates the working concept employed to detect misalignments due to lip seal cocking. It can be seen that a small horizontal misalignment is introduced due to the slant of the lip seal.
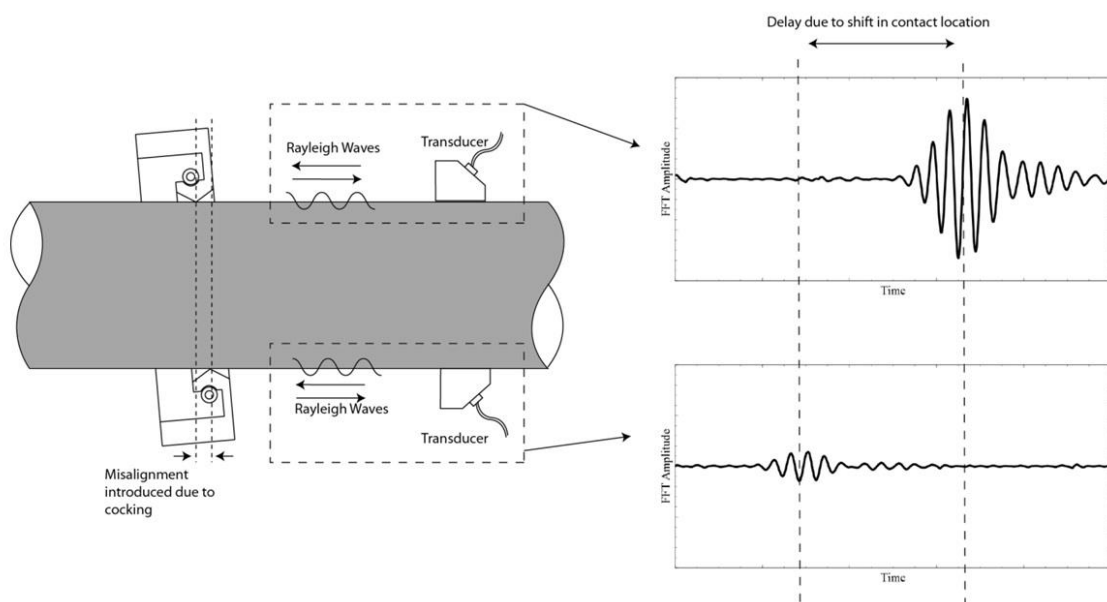
Fig. 8.3 Working concept in misalignment measurements of lip seals using Rayleigh waves

The misalignment is to be determined using conventional time of flight principles. To illustrate, Fig. 8.3 shows two identical Rayleigh wave sensors that are placed at the top and bottom of the shaft at the same nominal distance from the lip seal. Because the contact interface at the top is further away from the transducer, the reflected pulse from the contact interface arrives later compared to the reflected pulse from the bottom.

The delay in the arrival times of the echoes allows prediction of the misalignments as long as the speed of Rayleigh wave in the shaft is known. The difference in amplitude

---

[4] The work performed in this section was presented and published as a conference paper at the Society of Tribologists and Lubrication Engineers (STLE) 69th Annual Meeting and Exhibition (E. S. OOI & Dwyer-Joyce 2014).

of the two pulses are thought to be a direct result of the change in film geometry at the sealing zone. This is further explored in section 8.4.

8.3.2 Experimental Apparatus

In order to demonstrate the method, a series of tests were conducted on housings with misalignments that were intentionally added. Fig. 8.4 shows the general setup of the experiment. One end of a EN24 steel shaft, measuring 60mm in diameter was machined into a taper that fits the tail stock of a lathe.

A bespoke housing that houses the lip seal is attached on the chuck of the lathe. The simulated rotary motion was obtained as the chuck spins while the steel shaft remains static. Fig. 8.5 shows the design of the housing that was used. Misalignments were introduced by tilting the counter-bore at an angle, θ. In this study, two housings were made out of T68 aluminium with a θ of 3° and 5°.
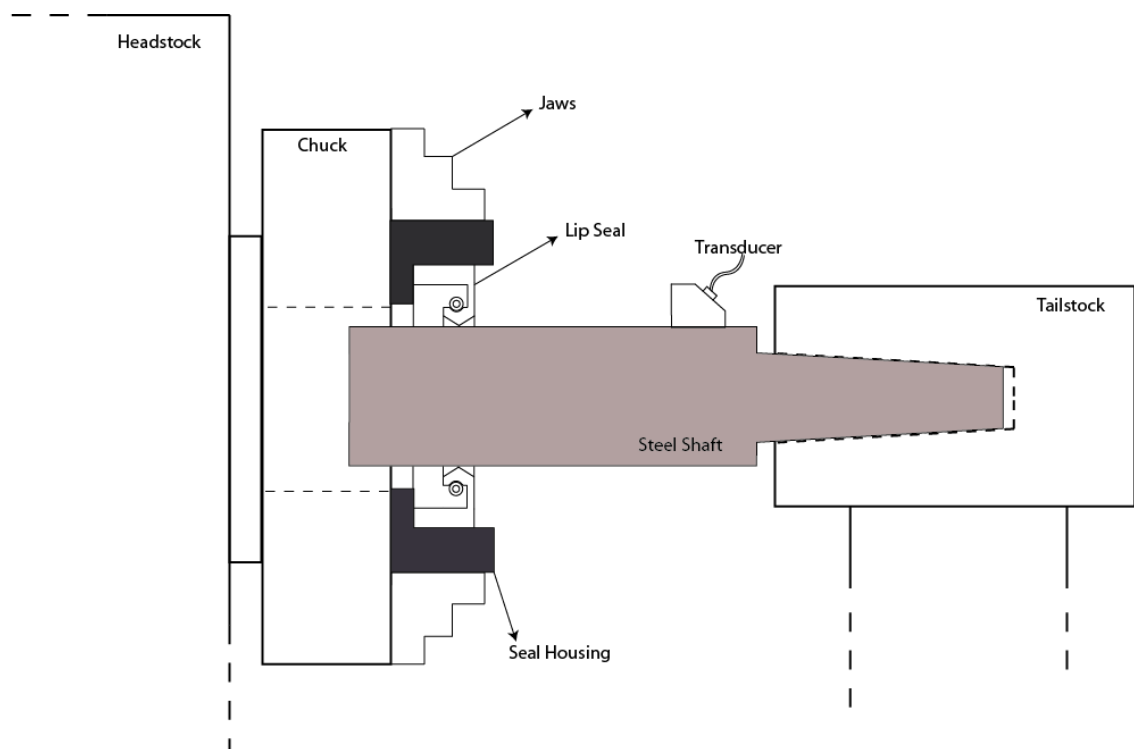
Fig. 8.4 Layout for lip seal interface measurements
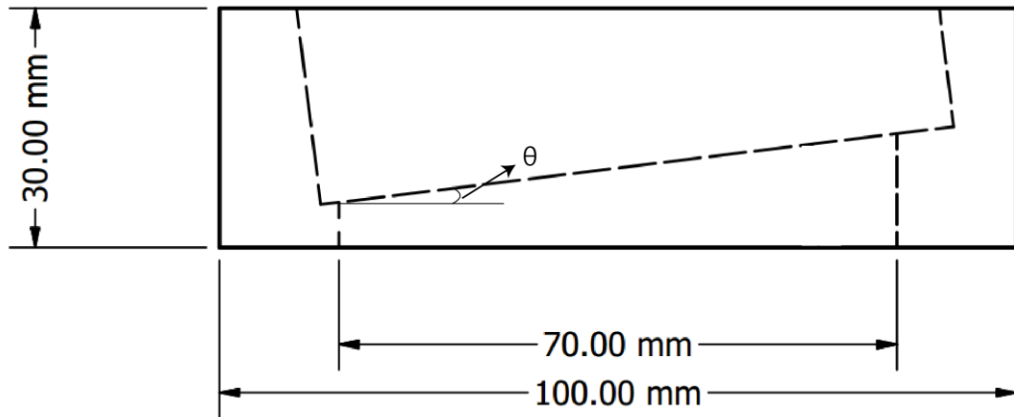
Fig. 8.5 Design of misaligned housing

The Rayleigh wave was generated using the angled wedge method detailed in section 3.3. The perspex wedge was custom made so that the profile of the base of the wedge matches perfectly with the circularity of the cylinder. A standard 2.5MHz longitudinal wave transducer 6.35mm in diameter was attached to the perspex wedge to generate Rayleigh wave via Snell's law. The same ultrasonic system as described in section 7.4 is used here.

8.3.3 Direct Measurements of Misalignment

In order to verify misalignment measurements obtained using Rayleigh waves, an independent form of measurement is required to which the ultrasonic data can be compared. The misalignment of the seals can be directly measured by coating the portion of the shaft which is in contact with the seal with ink. This is then followed by rotating the lip seal which causes the ink underneath the contact zone to be rubbed off, allowing a direct measurement of misalignment using a calliper. To facilitate the process, a small amount of acetone was spread across the lip of the seal. This makes the 'rubbing off' process easier and produces a clearer picture of the misalignment.

Fig. 8.6 Formation of wear tracks due to rubbing of seals across ink coatings

Fig. 8.6 shows the formation of 'wear tracks' which represents the portion of the coated area where the ink is removed due to contact with the misaligned seals. Using this method, the misalignment caused by the two housings are measured and tabulated in Table 8.2. These results can then be compared with measurements from the ultrasonic method to confirm if the measurements made were correct.

Table 8.2 Misalignment measurements measured from the wear tracks

Housing	Misalignment (mm)
$\theta = 3^o$	5.0 ± 0.1
$\theta = 5^o$	5.8 ± 0.1

8.3.4 Data Collection and Post-Processing

Before the start of each test, a small amount of lubricant (Shell Turbo T64) was applied to the circumference of the lip to supply the necessary lubrication required. The presence of the lubricant also helps in producing a larger amplitude reflection, making detection of the pulse easier.

Once the lubricant was applied, the housing was fitted onto the lathe and the shaft, together with the transducer. The transducer was operated at a frequency of 2.25MHz. An initial check was done in the same way as described in section 7.5 to single out the reflection that arises from the sealing zone.

Upon identifying the pulse, the DAQ (Data acquisition) system was then set to record data at a rate of 200 times per second (i.e. snapshots of the reflected pulse was taken at a rate of 200 times per second) for 10 seconds. In this way, a history of the pulse movement was saved in real time as the seal is being rotated around the shaft. The lathe was operated at 25rpm and the movement of the pulse across one revolution (approximately 2.5 seconds) is shown in Fig. 8.7.
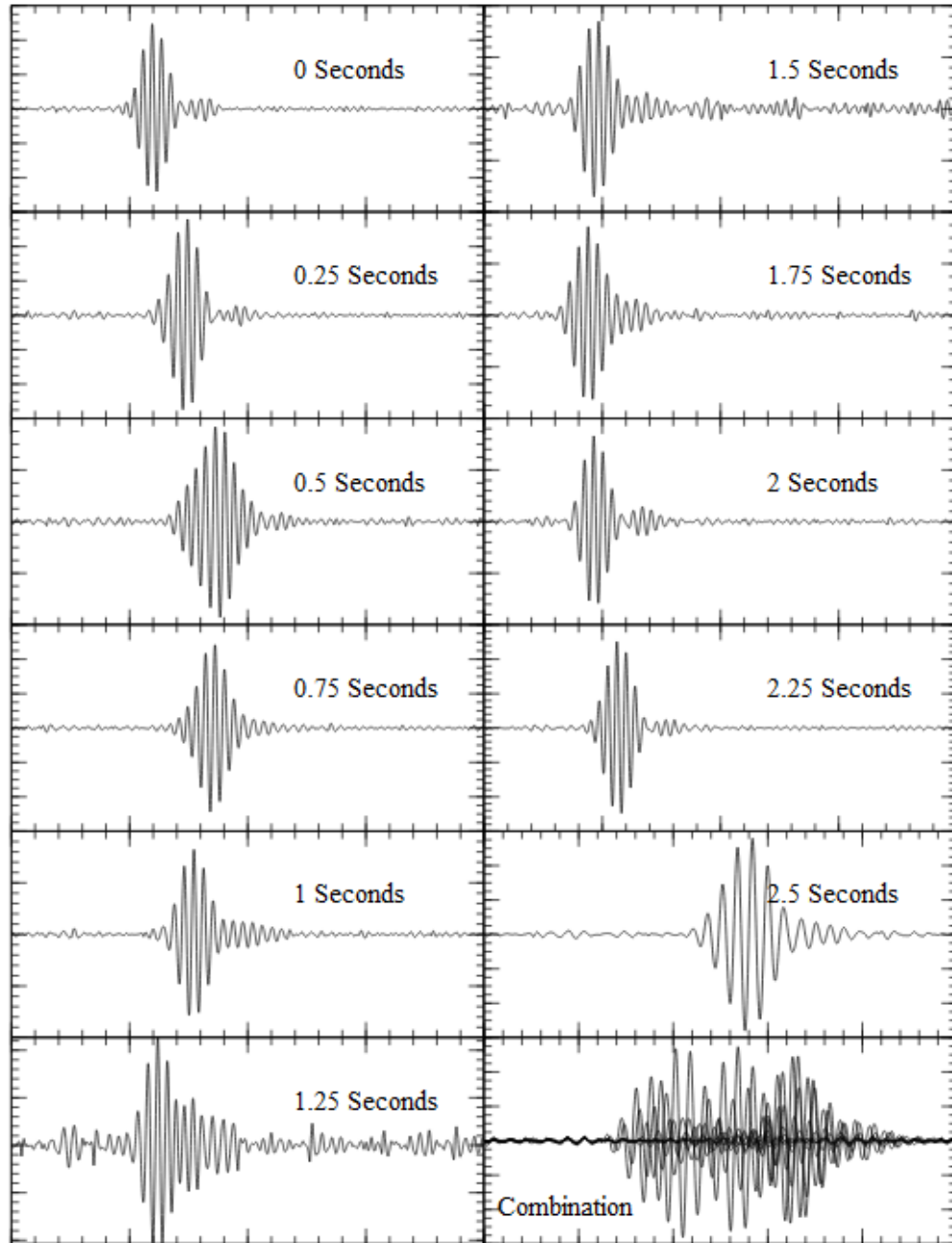
Fig. 8.7 Movement of the reflected pulse from the sealing zone over one revolution

From the viewpoint of the transducer, the movement of the sealing zone will appear as a reciprocating motion moving back and forth. The movement of the pulse was tracked by using algorithms programmed in LabVIEW that tracks the movement of the highest peak in each wave packet. The plot of a sample data is shown in Fig. 8.8. It can be seen that the movement of the pulse follows a sinusoid path which agrees with the geometry of the cocked seals as it rotates. The misalignment can thus be measured as the difference between the peak and valley of the sinusoid.
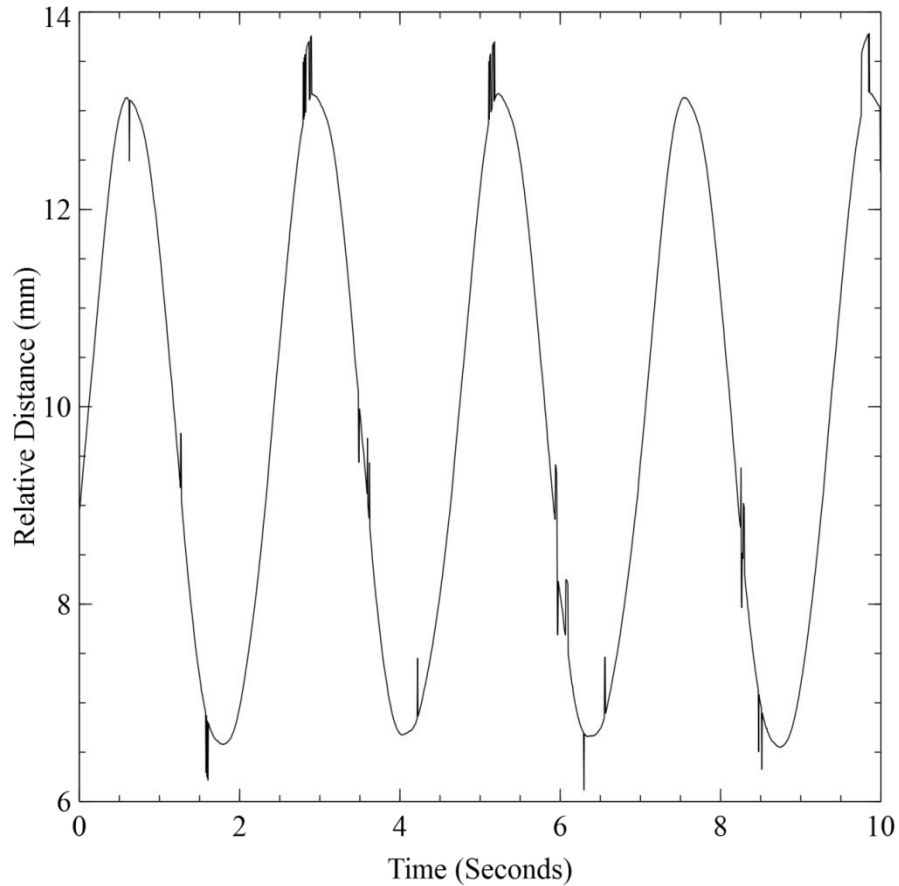
Fig. 8.8 Movement of the ultrasonic pulse reflected from the sealing zone.

For consistency, the tests were repeated at least 10 times for each housing. The results are plotted together with the misalignment measured from the wear tracks in Fig. 8.6 and are shown in Fig. 8.9. It can be seen that the results were repeatable within a tolerance of $\pm$ 1mm for both housings, with an average of 6.2mm for the 3° housing and 6.9mm for the 5° housing.
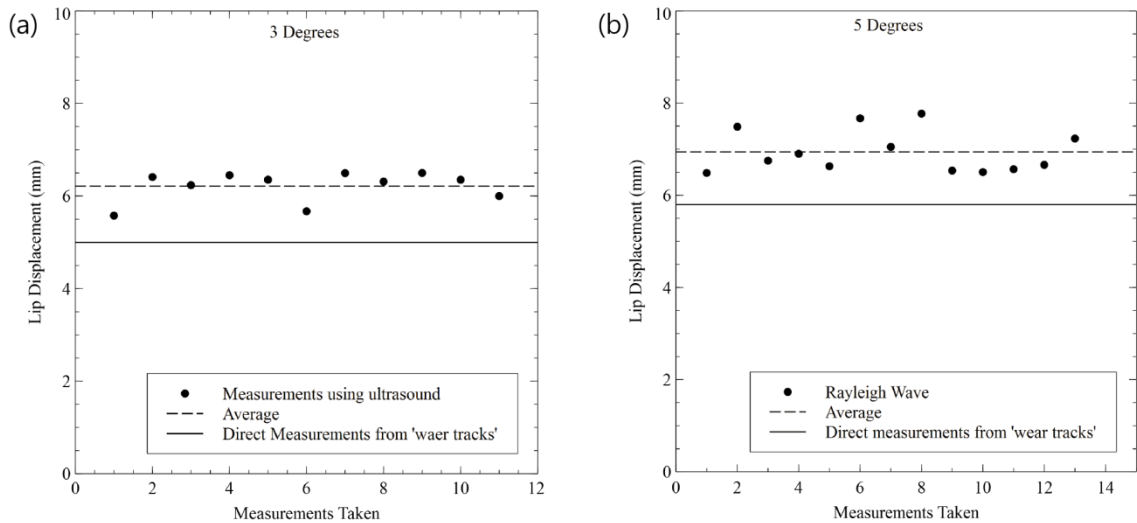
Fig. 8.9 Seals misalignment measurements (a) 3 degrees slant (b) 5 degrees slant

It is obvious from the results that in both cases, the measurement obtained using the ultrasound method is approximately 1.2 mm higher than the values obtained from the wear tracks in Fig. 8.6. This discrepancy can be explained upon closer examination of the behaviour of cocked seal as it rotates, as shown in Fig. 8.10. The apparent reciprocating movement of the lip caused by cocking results in a build-up of oil at the forward facing side of the seal, depending on the movement direction. These oil builds-ups are the main reflectors of the ultrasonic waves, thus, resulting in a slightly larger measured misalignment compared to the actual value.
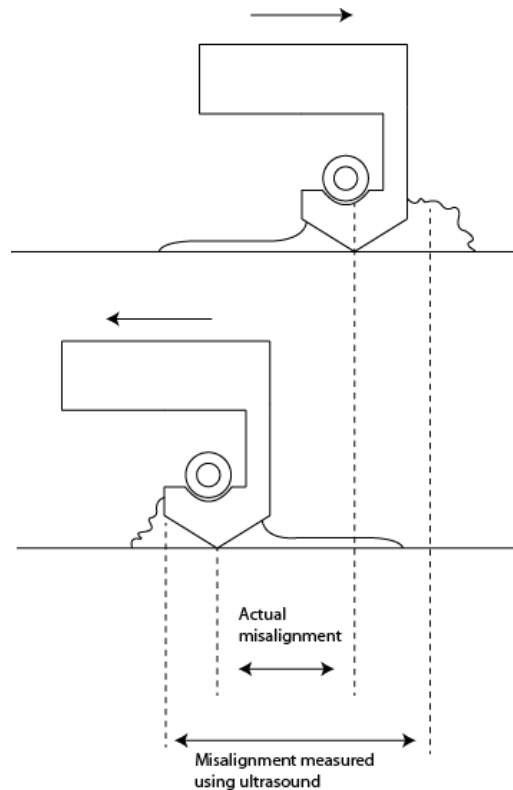
Fig. 8.10 Effect of oil build up

8.4 Monitoring Lip Seal Contact

In this section, several exploratory tests were performed to monitor a functioning lip seal using ultrasonic Rayleigh waves. With the exception of a different housing, the same setup and apparatus detailed in section 8.3.2 were used in the tests conducted here (c.f. Fig. 8.4). The design of the seal housing used here is shown in Fig. 8.11.

The housing was designed to allow proper functioning of the lip seal when the chuck of the lathe is rotated. The seal used in the experiments are standard nitrile rubber seal manufactured by Paulstra having a 60 mm bore, 80 mm outer diameter and 3 mm in thickness with an operating temperature of -30°C to 110°C.

The housing was made out of T68 aluminum. All of the tests were performed under ambient pressure and temperature with varying lathe speeds.

<div align="center">(a)   (b)</div>
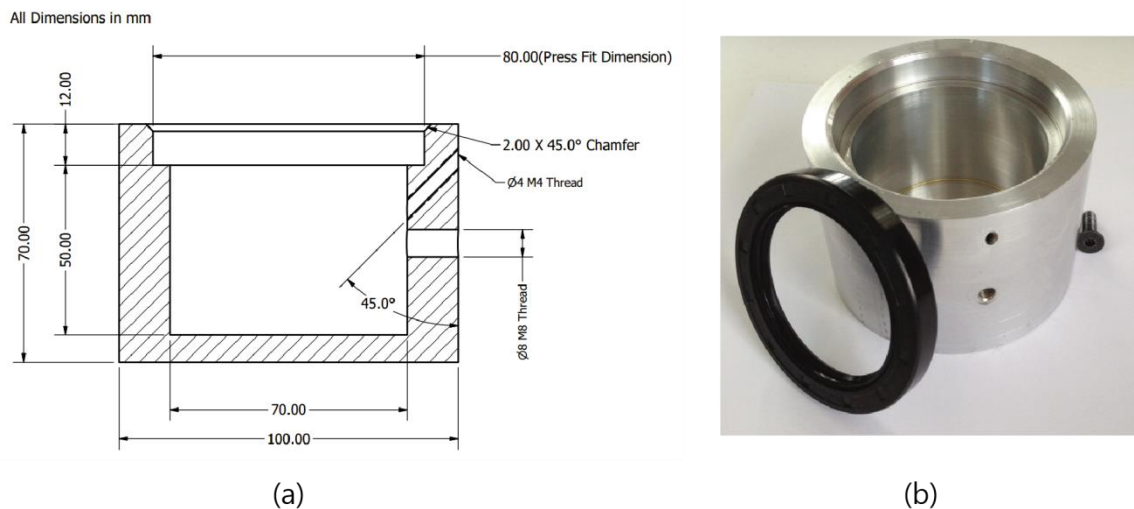
Fig. 8.11 Seal housing (a) Schematic (b) After manufacture

8.4.1 Tests on New Seals

Since the work here is exploratory in nature, it is intuitive to begin by first observing ultrasonic monitoring data from an undamaged seal in regular operation. A new seal (Specimen 1) was used for this purpose and all the required components are assembled on the lathe.

Mineral oil (Shell turbo T68) was then added into the housing to ensure that a supply of lubricant was always present, preventing lubricant starvation in the sealing zone.

The seal was allowed to stabilise at the intended speeds before actual measurements were taken. Ultrasonic monitoring data were recorded for 10 seconds each time at a rate of 10 kHz. This means that in the span of 10 seconds, 10000 waveforms were recorded. Table 8.3 gives the range of speeds that were tested, together with the amount of points that were measured over one revolution of the housing.

Table 8.3 Range of speed and measurement per revolution

Speed (rpm)	No. of captured points/ revolution
80	7500
190	3158
260	2308
350	1714
470	1277
625	960
840	714

Fig. 8.12 shows the monitoring data for the test conducted at 80rpm. The value quoted on the Y-Axis (FFT Amplitude) is a representation of the magnitude of the echo from the sealing zone. This was obtained by windowing the full envelope of the reflected

pulse from the sealing zone and performing an FFT on the pulse from which the FFT amplitude can be extracted (The process of conversion to frequency domain using FFT is simillar to that described in section 7.5.5). A cyclic behavior is evident from the captured data, with the repetition of each cycle corresponding exactly to 1 revolution of the shaft.
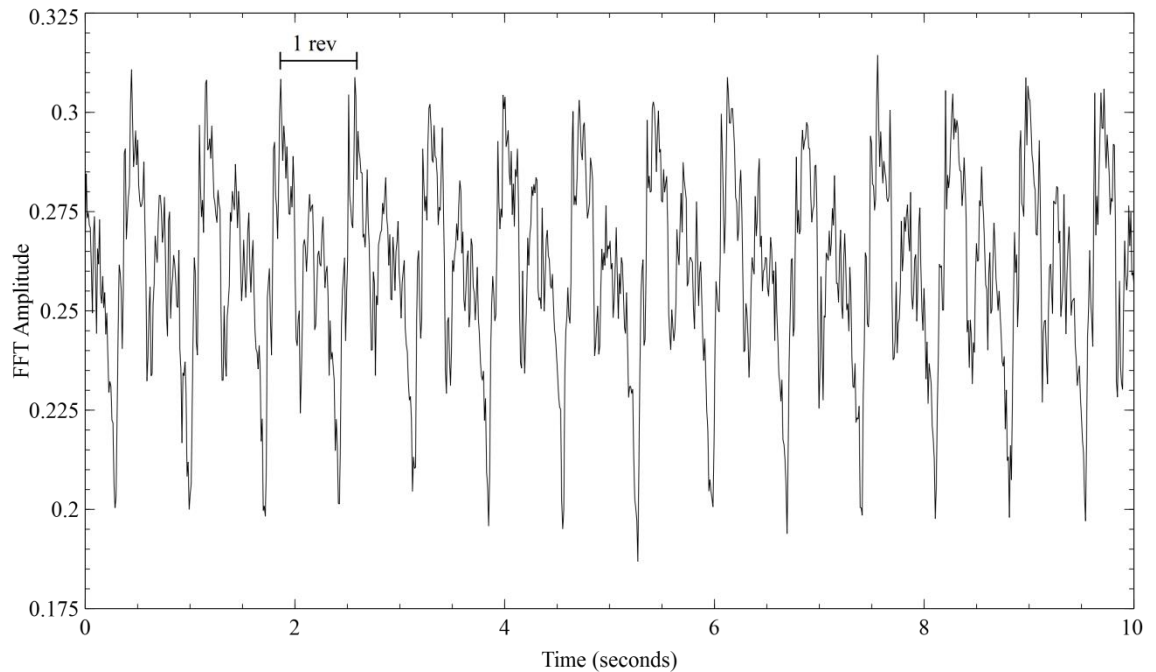
Fig. 8.12 Monitoring data of Specimen 1 rotating at 80rpm

Test data at varying speeds over 1 revolution are shown in Fig. 8.13. It can be seen that the qualitative behaviour of each repeating cycle in the monitoring data remains roughly the same for the range of speeds tested.
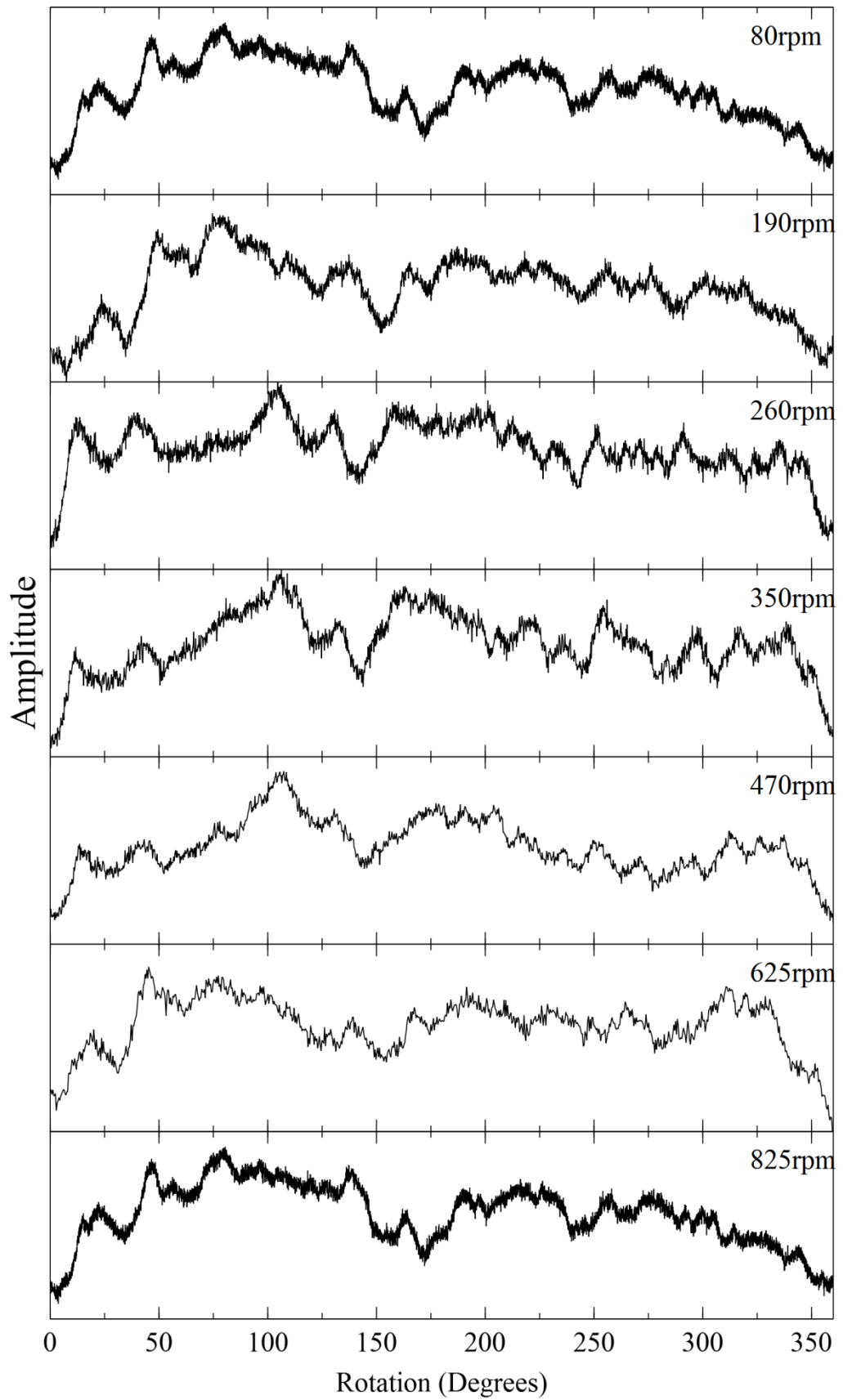
Fig. 8.13 Cyclic behaviour of Specimen 1 operating at different speeds shown over a single revolution

Using the same seal, repeat tests were conducted at different instances (i.e. different test days, upon diassembly and reassembly of rig) and the results at 350rpm are shown in Fig. 8.14. It can be seen that in this case, although the cyclic behaviour persists, the shape of each cycle varies with each test.
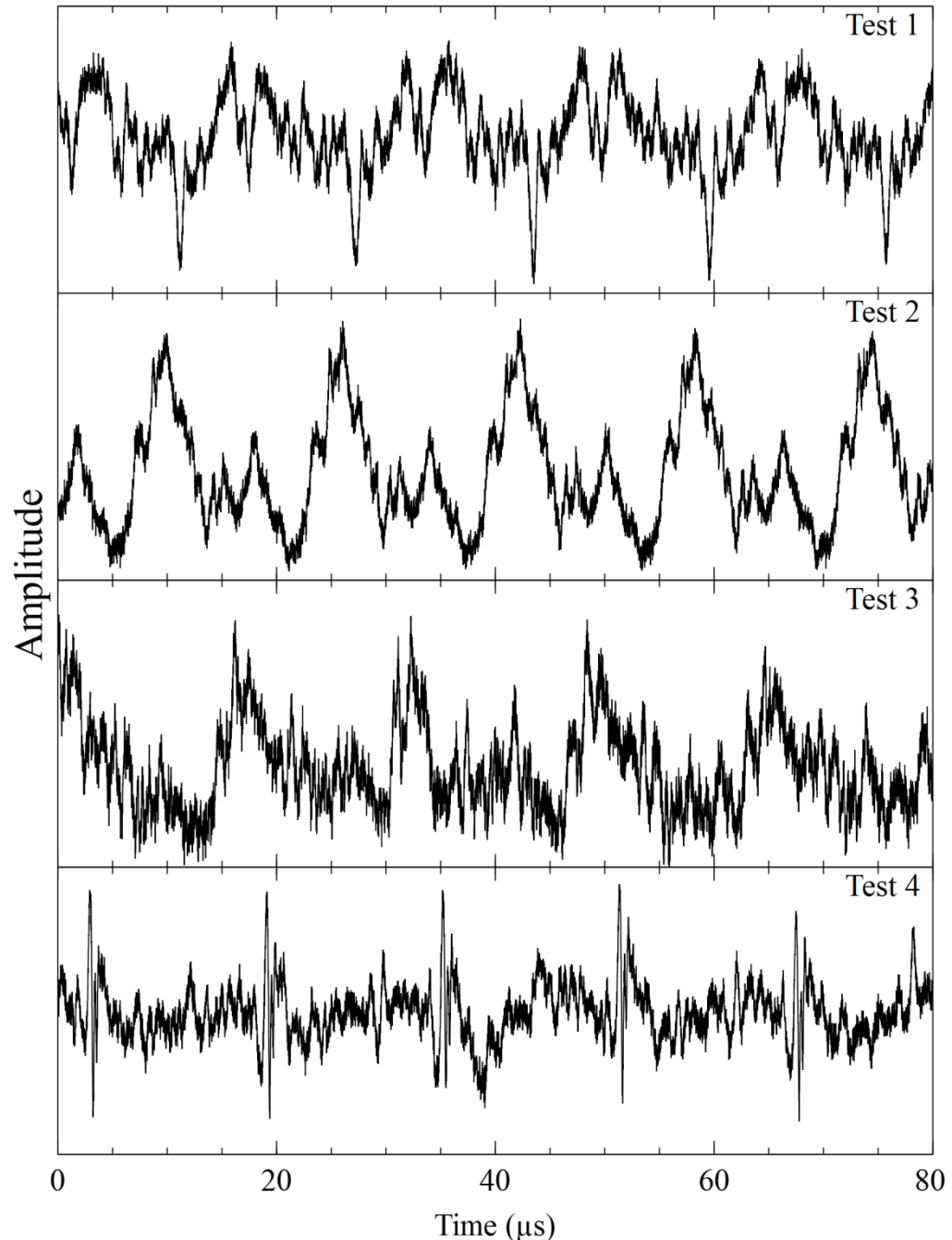
Fig. 8.14 Cyclic behavior variation of Specimen 1 at 350rpm at different test instances.

A quantitative analysis of the results from both Fig. 8.13 and Fig. 8.14 was performed by evaluating the mean FFT amplitude across time and plotting the results in Fig. 8.15. For each set of test, two test runs were conducted. It can be seen that outside of the similarity observed between the repeats (test runs) of the same test, there is very little

correlation between Tests 1-4 even when the conditions under which the tests were conducted were similar.
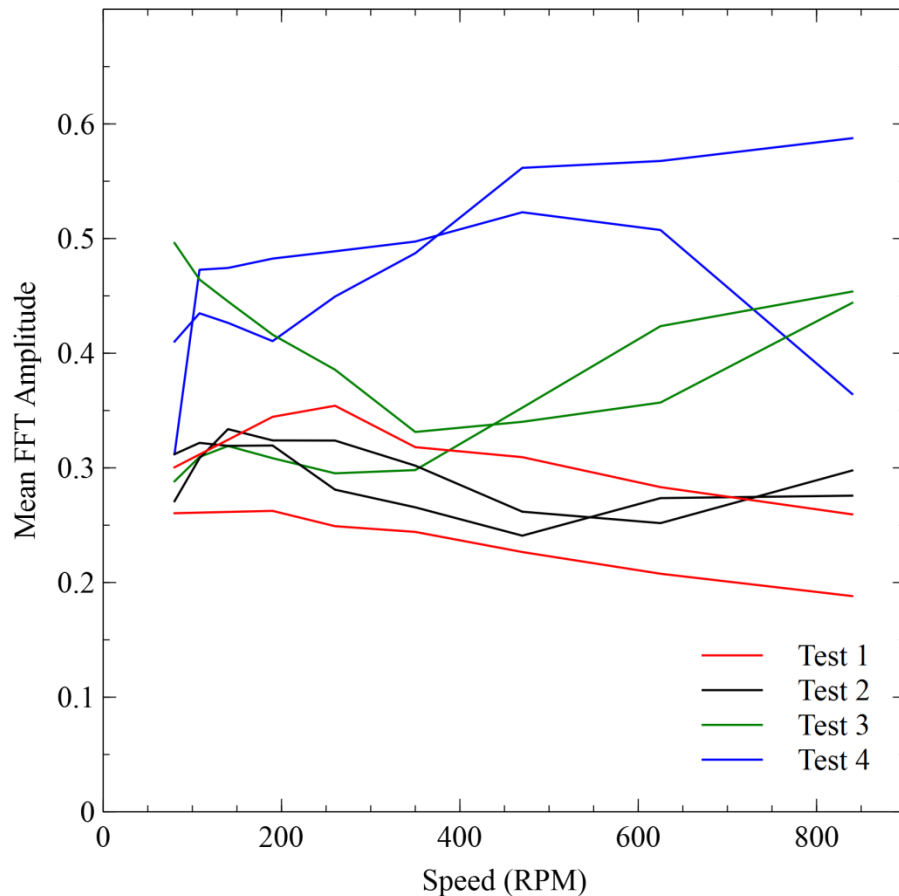
Fig. 8.15 Reflected wave amplitude from the sealing zone of Specimen 1 with increasing speed. 2 repeats for each test.

Based on the results obtained, the findings can be summarised as follows:

1. Monitoring data of reflected Rayleigh wave from a lip seal has shown a persistent cyclic behavior.
2. The shape of the cycles remain the same as rotational speed was increased (Fig. 8.13).
3. The shape of the cycles change when testing was repeated at different instances. For example, when the tests was repeated at a different day or upon disassembly and reassembly of the experimental apparatus (Fig. 8.14).
4. Quantitatively, the amplitude of the reflected wave follows the same trend only when the tests were repeated during the same test instance (i.e. Test 1, repetitions 1 and 2 will have a similar trend and likewise with other test instances).
5. Different tests instances show no relatable trends.

In regular operation of lip seals, a layer of lubricating film exist at the sealing zone and it is this lubricating film that reflects the ultrasound signal. The cyclic behaviour

observed in all the tests suggests that the film changes in a cyclic fashion during operation.

Studies on Rayleigh wave interactions with a liquid film have been sparse. Of the few reviewed in Chapter 4, results from McHale et al (McHale et al. 1999) suggests that even a small change in dimensions of a liquid strip would greatly effect the reflected amplitude. Works performed by Billy and Quentin (De Billy & Quentin 1983) have shown how the meniscus formed by a liquid in contact with a solid has a profound effect on the passage of Rayleigh wave through the liquid. Thus, one conjecture that can be drawn is that the cyclic behaviour observed is, in part due to the changing shape of the meniscus that is formed on the air side of the lip seal as the shaft rotates.

Additionally, this observation can be extended to further explain the dissimilarity between tests data obtained at different test instances. For each test instance, initial setup of the experiments requires assembly of the shaft and the seal housing on the lathe. It is likely that doing so changes the basic shape of the meniscus for each test instance, thus affecting repeatability of the data, especially when the reflected amplitude is thought to be highly sensitive of the shape of the meniscus.

At this stage, it is difficult to attribute the monitoring data to a single phenomenon as the changes that occur at the sealing zone are complex and consists of a combination of various changing features of the sealing film (e.g. cavitation and viscosity changes).

8.4.2 Tests on Damaged Seals

Defects were intentionally added to the lip of two seals (the same make as Specimen 1). The artificial defects are shown in Fig. 8.16.

(a)   (b)
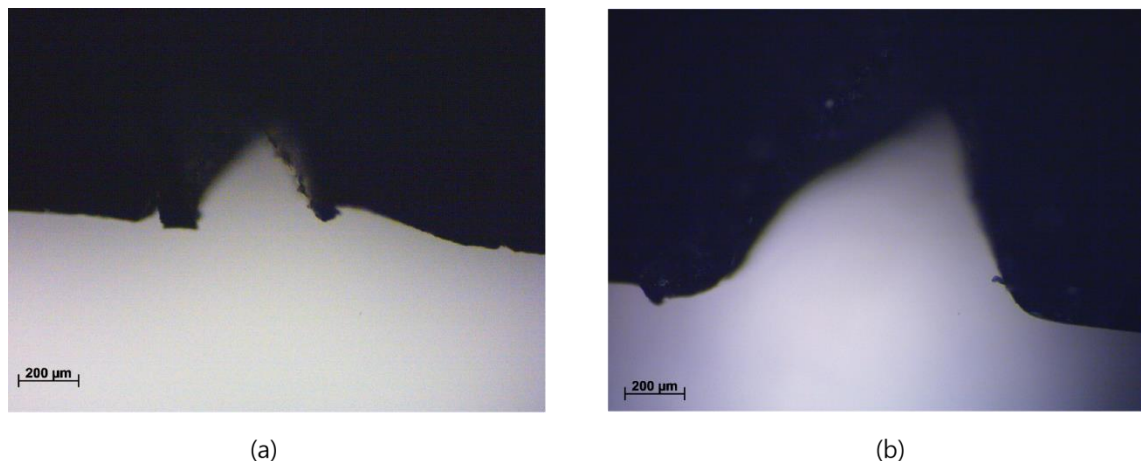
Fig. 8.16 Artificial defects added to the lips seals (a) Medium defect (b) Large defect

The seals were tested in the same way as Specimen 1 and the monitoring data for 1 revolution is plotted in Fig. 8.17 for both seals with medium and large artificial defects. It can be seen that, in contrast to an undamaged seal, the cyclic behaviour undergoes some changes as the rotational speed was increased. This is noticeable especially when going from 80rpm to 260rpm.

The marked change going from 80rpm to 260rpm can be explained by using the reverse pumping mechanism of lip seals. At low speeds, the pumping rate due to the reverse pumping mechanism is small and thus unable to cope with the leakage of the seals. As the speed increases, so does the pumping rate. To a certain extent, this stabilises the film geometry, resulting in a less dramatic change in the shape of the cycles at higher speeds. It should be noted however that some leakage still occurs, even at high speeds, as confirmed with visual observation of the sealing zone.
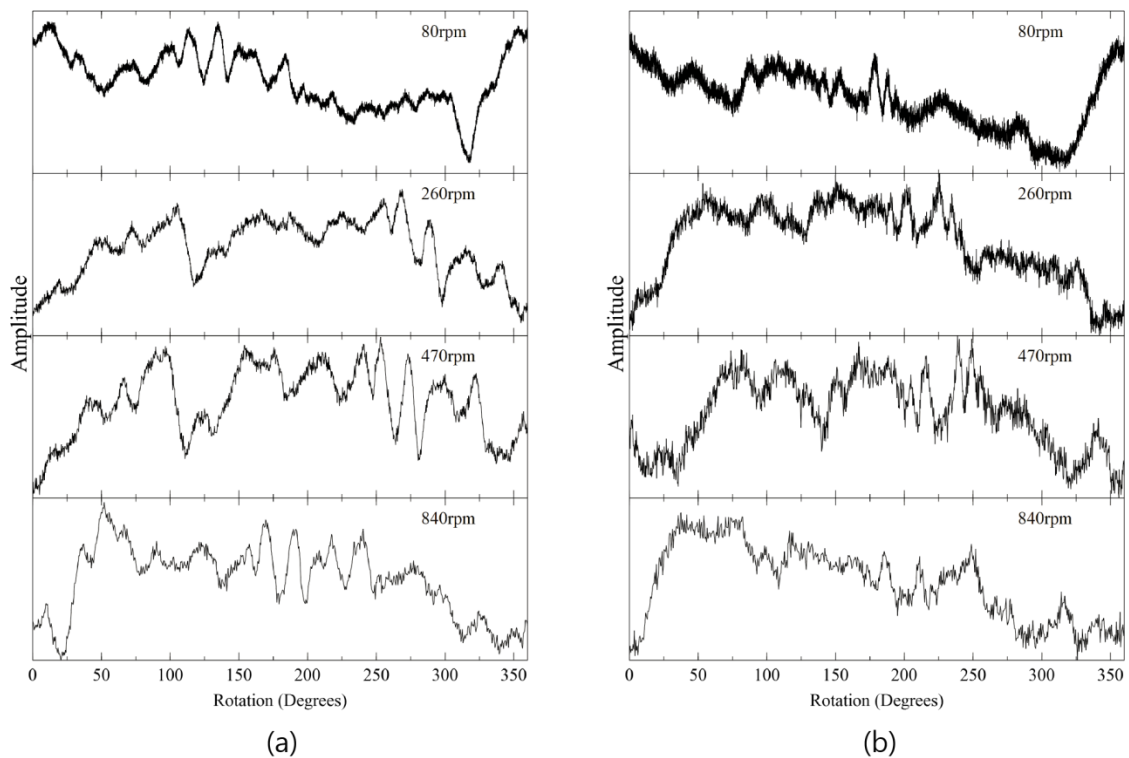
Fig. 8.17 Monitoring Data (a) Medium Defect (b) Large Defect

Examination of the monitoring data reveals no distinctive outliers (e.g. spikes in data) that can be confidently identified to arise from the defect as it passes over the region monitored by the sensors.

A quantitative assessment of the data in Fig. 8.17 was performed by taking the mean of the FFT amplitude across time and plotting them against rotational speed. The results are shown in Fig. 8.18. It appears that there is no distinct pattern of reflected wave amplitude as rotational speed is increased. However, the reflected amplitude for the seal with a large defect is much smaller than the nominal amplitudes obtained thus far. This seems to suggest that higher leakages results in a much lower reflection coefficient.
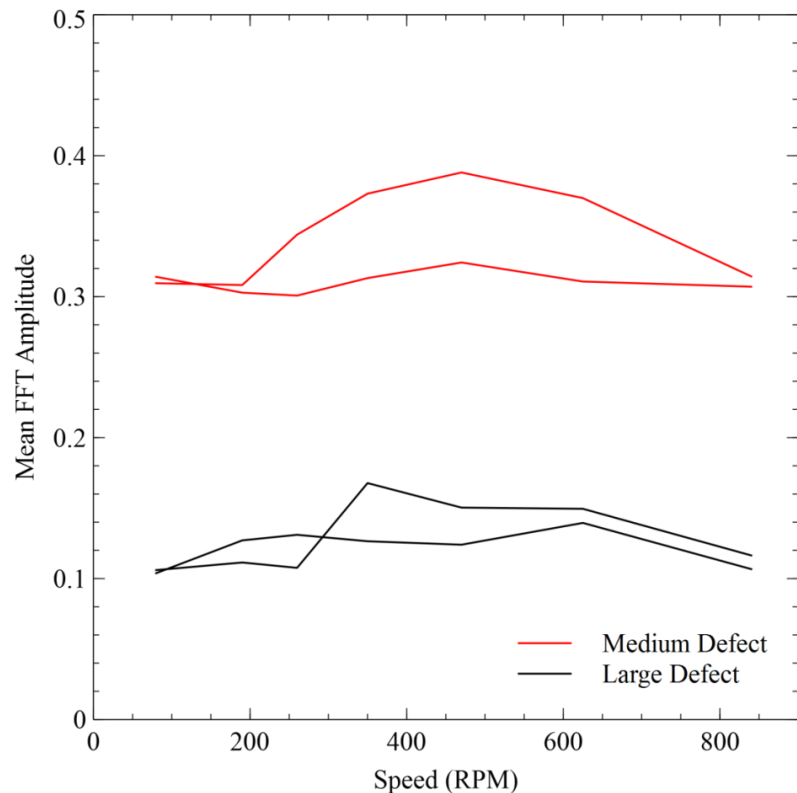
Fig. 8.18 Variation in reflected amplitude for seals with artificial defects

8.4.3 Monitoring Degradation of a Lubricating Film

A mode of failure that occurs in a lip seal happens when the sealing zone is starved of liquid lubricant and hence runs 'dry'. This causes an increase in friction which leads to higher temperatures, both of which shortens the lifespan of an operating seal.

Experience has shown that the presence of a lubricating film results in better echoes detected from the sealing zone. Thus based on this premise, it would be possible to detect incipient failures as the seal starts to run dry. The working principle is that as the lubricating film begins to dissipate, the reflected amplitude should, in theory reduce accordingly.

As a starting point, the same setup used in the preceding section was used here. Attempts to induce failure were made by adding small amounts of acetone at set intervals to the sealing zone. It is expected that the acetone should dissolve the oil, reducing viscosity and hence allowing the oil in the sealing zone to leak away. However, the results obtained show no perceivable change to the monitoring data.

Upon further inspection of the sealing zone, it was discovered that copious amount of oil-acetone mixture was still present underneath the sealing zone. Though at this stage the lubricating film was formed by the degraded oil-acetone mixture, the monitoring data was not sensitive enough to detect the changes to the composition of the lubricating film.

113

In order to generate a fully dry sealing interface, pure acetone was used in place of lubricating oil. It is expected that acetone, being a volatile fluid would easily evaporate from the sealing zone during operation due to an increase in temperature, hence producing a fully dry contact.

A small amount of acetone, enough to fully lubricate the sealing zone over the entire circumference of the lip seal was initially added to the seal. The lathe was then operated at 260 rpm for a period of 60 seconds. The reflected pulse was continuously recorded for the duration of the test. This was repeated a total of three times and the results are shown in Fig. 8.19.

It can be seen that the amplitude of the reflected pulse decreases in a linear fashion with time, suggesting that the evaporation of the acetone at the sealing zone takes place in a similar fashion. At approximately 40s, the sealing zone begins transition into fully dry conditions. The ultrasonic monitoring data reflects this, with peaks appearing followed by a flattening of the curve.
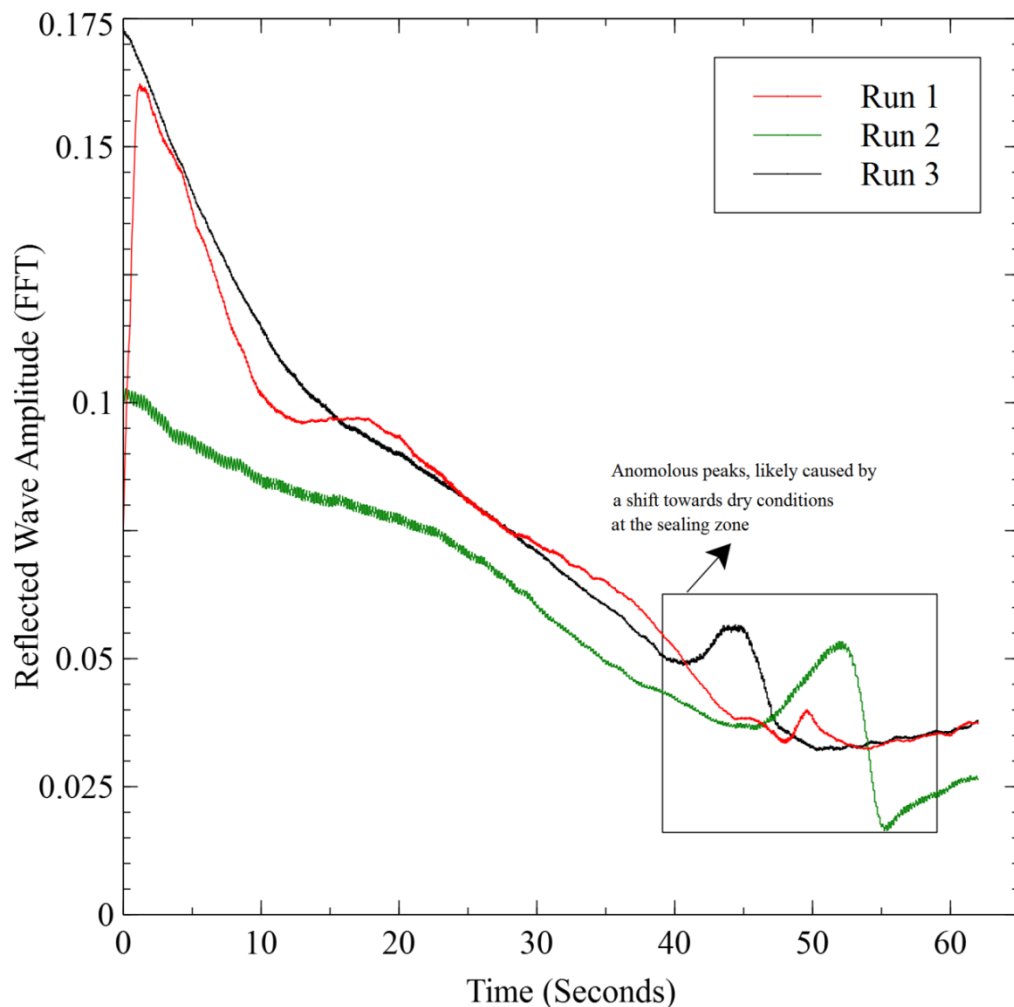
Fig. 8.19 Acetone degradation at the sealing zone of a lip seal operating at 260rpm

8.5 Discussion

The exploratory work performed here shows potential in the application of Rayleigh wave to monitor lip seals. In particular, experiments conducted to measure seals misalignment due to cocking were promising with consistent readings measured over many repeats. In addition, the technique is beneficial as it relies on tried and tested TOF methods, thus elimnating the need for specialist interpretation of the monitoring data. Though there is an overestimation of apporximately 1mm in the ultrasonic data, this value is expected to not greatly vary between differing lip seals and thus, a correction can be made to provide an accurate measure of lip seal misalignment.

When a working seal was monitored, cyclical behaviour was observed in all the tests conducted. This shows that at least on a qualitative level, the ultrasonic system is capable of picking up cyclic data patterns that directly reflect the behaviour of the lubricant at the sealing interface. The challenge lies with deciphering components of the ultrasound signal that relates to changes in the lubricating film at the sealing zone. The main difficulty faced here is that the effects that a lubricating film has on reflected Rayleigh waves is still not fully understood. Advancement of work in this area will open up doors in better undertanding the monitoring data obtained.

Another complexity when monitoring lip seals lies in the variability of the lubricating film formed. The tests have shown that reflected Rayleigh waves are sensitive towards changes in geometry of the lubricating film formed. However, in operating lip seals, the shape of the lubricating film is not a controlled parameter and thus likely to vary considerably, even among simillar applications. Again, if it was possible to relate changes in the ultrasound signal to changes in film geometry, then the monitroing data can be inteprated to provide a real time description of the nature of the lubricating film.

The same challenge was faced when monitoring cases of lubricant film degradation. Though the experiments was sucessfull in obseving the transition between a lubricated seal towards a seal that runs dry, the data remains qualitative in nature.

The experiments were conducted using a seal housing that rotates while the shaft remains static. This configuration was chosen to allow practical use of the ultrasonic system available. In practice, it is the shaft that rotates with respect to the seal. Doing so introduces complications when using conventional ultrasonic sensors as some form of coupling is required between the surface of the shaft and the ultrasonic sensors in order to propogate Rayleigh waves down the shaft. This cannot be easily achieved, particularly when the shaft is rotating at high speeds. One solution to this is via the use of air coupled transducers i.e. EMATs (Electomagnetic transducers) that eliminates the need for physical coupling with the shaft.

A major concern regarding the use of acetone is that the material of which the lip seals are made out of (Nitrile) has a low chemical resistance towards acetone. Precautions were taken by using only small quantities of acetone for each test and running the tests in short intervals to prevent any reactions that may occur. Additional precautions were

taken by visually inspecting the seals for damage after testing to ensure that no damage to the seals has taken place.

8.6 Conclusions

Lip seals are common engineering components which are simple in design yet the physical phenomenon that governs its effective operation are complex in nature. Pilot work done in this chapter have focused on using Rayleigh wave to condition monitor lip seals in operation.

Misalignments due to cocking have been sucessfully measured using TOF principles and has the advantage of being conceptually simple to understand, requiring no specialist interpretation of ultrasonic data obtained.

Monitoring data obtained from a lip seal under operation have shown repeating cyclic patterns indicating that the ultrasonic system is capable of detecting some form of physical change that occur at the sealing interface. However, the knowledge gaps in understanding how Rayleigh wave interacts with a fluid film, coupled with the highly variable nature of fluid shape resulted in inconsistent monitoring data obtained and prevented any further interpretation of the ultrasonic data.

Lip seals with artificial defects were tested also tested. However, the data have thus far only been qualitative with no firm detection of the defect using ultrasonic Rayleigh waves.

Tests conducted in observing fluid film degradation at the sealing zone was sucessful, with the ultrasonic data showing a steady drop in reflected Rayleigh wave amplitude as the lubricating film degrades via evaporation, inducing dry conditions at the sealing zone.

9 Conclusions

The aim of the work here was to develop a better understanding of how Rayleigh wave interacts with an interface. This was motivated by the desire to develop a condition monitoring device that uses Rayleigh waves. First, an intuitive model of the interface was developed by assuming that the contact can be modelled as a series of springs. Led by this view, finite element simulations and experimental work were performed to obtain the results which are then cross examined against each other as well as with the analytical model. The agreement were excellent, validating that the model of the interface was acceptable and thus allowing information previously inaccessible to be extracted from Rayleigh wave reflection data.

The main conclusions derived from each chapter of original work are given in the following sub-sections.

9.1 Development of a Novel Analytical Model (Chapter 5)

A novel analytical model was developed by modelling the interface as a discrete interface connected by springs with both normal and tangential stiffness. The idea behind the model is simple, as a Rayleigh wave impinges on the modelled springs; the springs are excited and in turn generates a reflected waveform of its own. It was shown that the stiffness is directly proportional to reflection coefficient, thus allowing the prediction of interface stiffness directly from reflection coefficients of a Rayleigh wave. Though the study here was performed using line contacts, no restrictions were imposed on the geometry of the surface that comes into contact, as long as the interface appears discrete to the incoming Rayleigh wave (i.e. contact dimensions are much smaller than wavelength of the Rayleigh wave)

9.2 Finite Element Simulations (Chapter 6)

The analytical model developed was further studied by using finite element simulations. This was performed using COMSOL, a finite element software package. Comparisons between FE and analytical results show an overall good agreement. Qualitatively, the agreements were excellent, with FE results demonstrating the same linear relationship between stiffness and reflection coefficient that was first shown in the analytical model. Quantitatively, the FE method predicts a higher reflection coefficient with errors ranging from 32% to 6%. It was also shown that the magnitude of the errors is influenced by both stiffness and stiffness ratio, decreasing with an increase in stiffness and/ or decrease in stiffness ratio.

The errors are thought to stem from the use of a downscaled model, causing near field effects to potentially influence the results. Suggestions to address these issues are given in section 9.5.

9.3 Experimental Measurements (Chapter 7)

Experimental work was carried out to study how Rayleigh wave interacts with an interface. A line contact was formed by pressing a cylindrical specimen onto the surface of a steel block. Rayleigh waves were generated using the angled wedge method operating in pulse-echo mode.

The effects of varying roughness of the interface and using different material combinations were studied. Changes that reduce interface stiffness such as an increase in roughness and a decrease in Young's Modulus of the contacting pair was found to decrease reflection coefficients obtained experimentally.

The experimental data obtained agreed well with results from the analytical model and FE simulations with higher errors experienced when reflection coefficients were lower. This was attributed to effects of surface adhesion. Based on the reflection coefficients, predictions of interface stiffness were possible by using the analytical model as long as the stiffness ratio, which can be estimated from experimental results, is known. In this way, it is possible to probe interface stiffness via the use of reflected Rayleigh waves.

9.4 Exploratory Work on Lip Seals (Chapter 8)

Exploratory work was undertaken in this chapter to demonstrate the potential of Rayleigh wave as a condition monitoring tool to monitor lip seals in operation. This was done using an experimental setup by sending down a pulse of Rayleigh wave down a steel shaft that makes direct contact with the lip seals. Reflected waves that stem from the sealing zone were recorded and analysed.

It was shown that measurements of lip seal misalignment were possible by measuring the delay in time of arrival of the reflected pulse from the seal interface. An added benefit is that the technique uses fundamental ultrasonic properties, thus eliminating the need for specialist interpretation of the ultrasound data.

Under normal operation, there exists a thin layer of film at the sealing zone. Attempts were made to ultrasonically monitor the changes in this fluid film as the seal operates where cyclic patterns corresponding to the operating speed of the seals were observed. This indicates that the ultrasonic system was capable of measuring some form of physical interaction that takes place at the sealing zone. However, repeatability of the data was an issue and this was thought to be induced by the variation of the meniscus of the lubricant formed at the sealing zone.

Attempts made in observing fluid film degradation at the sealing zone were successful qualitatively. The reflected amplitude showed a steady drop in magnitude as the lubricant at the sealing zone degrades via evaporation which causes the seal to run under dry conditions.

At this stage, the experimental work performed using Rayleigh waves has shown that it is fully feasible to obtain ultrasonic readings from a lip seal. Previously, this has not

been possible using conventional bulk waves. However, existing knowledge gaps and variability in the data hamper further progress in this area as interpretation of the monitoring data was not possible outside of rudimentary qualitative correlations.

9.5 Future Work and Recommendations

The analytical model developed in this research serves the purpose of providing an intuitive understanding of how Rayleigh waves interact with a contact interface. The scope of this research project has so far been limited to a discrete interface, with experiments carried out on line contact. A natural progression of this work would be to generalize the model developed here. This would allow application of Rayleigh waves to a larger variety of contact interfaces. Generalizations can be made to include

- Non discrete contact. This allows interfaces with significant contact area to be probed using Rayleigh waves.
- Plastic effects, improving accuracy of the model, especially in the case of rougher surfaces where plastic crushing of asperity becomes significant
- Effects due to surfaces in relative motion. So far the model has concentrated on static loading of two surfaces. If the two surfaces are in relative motion, potentially, Rayleigh waves could be used to measure frictional forces at the interface.

The results presented in this work have been validated by comparing reflection coefficients obtained experimentally, analytically and via FE simulations. The interface stiffness has so far not been measured experimentally. It would be an interesting prospect to experimentally measure both the normal and tangential interface stiffness and make a comparison against predicted results to further validate the work performed here. In this way, the stiffness ratio which has so far been largely an approximated variable can be unambiguously determined for the specific case of a line contact studied here.

Though finite element predictions have shown satisfactory agreement with both analytical and experimental results, there are still elements that could benefit from further work to improve accuracy of the model. With the right resources, true to scale models can be simulated to mitigate near field effects that have been identified as a potential cause of the errors observed in the model.

One area in which high impact further work could be performed is in the understanding of how Rayleigh wave interacts with a fluid film sandwiched between an interfaces. This has far reaching consequences as many common components rely on such a fluid film for optimum performance (e.g. bearings, seals, gears). Work on lip seals (Chapter 8) have shown that although current experimental techniques are capable of capturing Rayleigh wave data from the sealing zone, the lack in understanding prevented further interpretation of the ultrasonic data. Thus, extension of the analytical model to include a thin film layer at the contact would greatly aid in improving the applicability of Rayleigh waves as a condition monitoring tool.

Additionally, the consistency of the monitoring data from a lip seal has thus far been hampered by the variability of the shape of the film produced at the sealing zone. A method of generating a consistent shape of the film would likely produce a more consistent set of data obtained, thus allowing for a more informed interpretation of the monitoring data.

The work performed on lip seals have so far been applied in a research setting, with the Rayleigh wave being generated on a static shaft while the seal is rotated. For the technique to be applicable in the field, the issue of generating Rayleigh waves on a rotating shaft has to be addressed. Contactless methods of generating Rayleigh waves are perhaps ideal for this, with active research being conducted using laser generated Rayleigh waves as well as the established use of EMATs in the industry. Research efforts can be focused on adapting these existing technologies to the monitoring of lip seals to improve robustness of the technique.

References

Aalco, 2014a. Copper~Brass~Bronze - Brass - CW614N Brass Rod. Available at: http://www.aalco.co.uk/datasheets/CopperBrassBronze-CW614N-Brass-Rod_31.ashx.

Aalco, 2014b. Copper~Brass~Bronze - Pure Copper - CW004A Sheet and Plate. Available at: http://www.aalco.co.uk/datasheets/CopperBrassBronze-CW004A-Sheet-and-Plate_32.ashx.

Angel, Y.C. & Achenbach, J.D., 1984. REFLECTION AND TRANSMISSION OF OBLIQUELY INCIDENT RAYLEIGH WAVES BY A SURFACE-BREAKING CRACK. *Journal of the Acoustical Society of America*, 75(2), pp.313–319.

Austin, R.M. et al., 1979. *The Seal Users Handbook* 2nd Editio., BHRA Fluid Engineering.

Avan, E.Y., Mills, R. & Dwyer-Joyce, R., 2010. Ultrasonic imaging of the piston ring oil film during operation in a motored engine - towards oil film thickness measurement. *SAE International Journal of Fuels and Lubricants*, 3(2), pp.786–793.

Baart, P., Lugt, P.M. & Prakash, B., 2009. Review of the lubrication, sealing, and pumping mechanisms in oil- and grease-lubricated radial lip seals. *Proceedings of the Institution of Mechanical Engineers, Part J: Journal of Engineering Tribology*, 223(3), pp.347–358.

Baltazar, A., Rokhlin, S.I. & Pecorari, C., 2002. On the relationship between ultrasonic and micromechanical properties of contacting rough surfaces. *Journal of the Mechanics and Physics of Solids*, 50(7), pp.1397–1416.

Beheshti, A. & Khonsari, M.M., 2012. Asperity micro-contact models as applied to the deformation of rough line contact. *Tribology International*, 52, pp.61–74.

De Billy, M. & Quentin, G., 1983. Experimental study of the Scholte wave propagation on a plane surface partially immersed in a liquid. *Journal of Applied Physics*, 54(8), pp.4314–4322.

Biwa, S., Suzuki, A. & Ohno, N., 2005. Evaluation of interface wave velocity, reflection coefficients and interfacial stiffnesses of contacting surfaces. *Ultrasonics*, 43(6), pp.495–502.

Brown, M., 1995. *Seals and Sealing Handbook* 4th ed., Oxford: Elsevier Advanced Technology.

Callister, W.D. & Rethwisch, D.G., 2011. *Materials Science and Engineering* SI Version., John Wiley & Sons.

Chen, D.-P. & Haus, H.A., 1985. Analysis of Metal-Strip SAW Gratings and Transducers. *IEEE Transactions on Sonics and Ultrasonics*, SU-32, pp.395–408.

Cook, D.A. & Berthelot, Y.H., 2001. Detection of small surface-breaking fatigue cracks in steel using scattering of Rayleigh waves. *NDT and E International*, 34(7), pp.483–492.

Darbari, G.S., Singh, R.P. & Verma, G.S., 1968. Ultrasonic attenuation in carbon steel and stainless steel at elevated temperatures. *Journal of Applied Physics*, 39(5), pp.2238–2245.

Datta, S. & Hunsinger, B.J., 1979. First-order reflection coefficient of surface acoustic waves from thin-strip overlays. *Journal of Applied Physics*, 50(9), pp.5661–5665.

Datta, S. & Papanikolaou, S., 1986. *Surface Acoustic Wave Devices* 1st ed., USA: Prentice-Hall.

De-Billy, M., Quentin, G. & Baron, E., 1987. Attenuation measurements of an ultrasonic Rayleigh wave propagating along rough surfaces. *Journal of Applied Physics*, 61(6), p.2140.

Ding, X. et al., 2013. Surface acoustic wave microfluidics. *Lab on a Chip - Miniaturisation for Chemistry and Biology*, 13(18), pp.3626–3649.

Ditri, J.J. & Rajana, K.M., 1995. Analysis of the Wedge Method of Generating Guided Waves. In D. O. Thompson & D. E. Chimenti, eds. *Review of Progress in Quantitative Nondestructive Evaluation*. Springer US, pp. 163–170.

Dixon, S. & Palmer, S.B., 2004. Wideband low frequency generation and detection of Lamb and Rayleigh waves using electromagnetic acoustic transducers (EMATs). *Ultrasonics*, 42(10), pp.1129–1136.

Drinkwater, B.W. et al., 2009. Ultrasonic measurement of rolling bearing lubrication using piezoelectric thin films. *Journal of Tribology*, 131(1), pp.1–8.

Drinkwater, B.W., Dwyer-Joyce, R.S. & Cawley, P., 1996. A study of the interaction between ultrasound and a partially contacting solid-solid interface. *Proceedings of the Royal Society A: Mathematical, Physical and Engineering Sciences*, 452(1955), pp.2613–2628.

Dwyer-Joyce, R.S., Drinkwater, B.W. & Donohoe, C.J., 2003. The measurement of lubricant-film thickness using ultrasound. *Proceedings of the Royal Society A: Mathematical, Physical and Engineering Sciences*, 459(2032), pp.957–976.

Dwyer-Joyce, R.S., Drinkwater, B.W. & Quinn, A.M., 2001. The use of ultrasound in the investigation of rough surface interfaces. *Journal of Tribology*, 123(1), pp.8–16.

Dwyer-Joyce, R.S., Harper, P. & Drinkwater, B.W., 2004. A method for the measurement of hydrodynamic oil films using ultrasonic reflection. *Tribology Letters*, 17(2), pp.337–348.

E. S. OOI & Dwyer-Joyce, R.S., 2014. A Method of Evaluating Misalignments in Rotary Seals Using Ultrasonic Rayleigh Waves. In *Society of Tribologists & Lubrication Engineers Annual Meeting & Exhibition 2014*. Society of Tribologists and Lubrications Engineers, p. 1029.

Efunda, No Title. Available at: http://www.efunda.com/home.cfm [Accessed November 11, 2014].

Gautesen, A.K., 2002. Scattering of a Rayleigh wave by an elastic quarter space - Revisited. *Wave Motion*, 35(1), pp.91–98.

Gelinck, E.R.M. & Schipper, D.J., 1999. Deformation of rough line contacts. *Journal of Tribology*, 121(3), pp.449–454.

Gonzalez-Valadez, M., Baltazar, A. & Dwyer-Joyce, R.S., 2010. Study of interfacial stiffness ratio of a rough surface in contact using a spring model. *Wear*, 268(2-3), pp.373–379.

Graczykowski, B., 2012. The reflection of Rayleigh surface waves from single steps and grooves. *Journal of Applied Physics*, 112(10).

Greenwood, J.A. & Williamson, J.B.P., 1966. Contact of Nominally Flat Surfaces. *Proceedings of the Royal Society A*, 295, pp.300–319.

Hess, P., 2002. Surface acoustic waves in materials science. *Physics Today*, 55(3), pp.42–47.

Hévin, G. et al., 1998. Characterisation of surface cracks with rayleigh waves: A numerical model. *NDT and E International*, 31(4), pp.289–297.

Hull, B. & John, V., 1988. *Non-Destructive Testing*, London: Macmillan Education Ltd.

Innerspec, Technology. , 2014(23 September). Available at: http://www.innerspec.com/node/18.

Johnson, K.L., 1985. *Contact Mechanics* 1st ed., Cambridge: Press Syndicate.

Kazuo, K., 1957. Ultrasonic Attenuation in Steel and Cast Iron. *Science reports of the Research Institutes, Tohoku University. Ser. A, Physics, chemistry and metallurgy*, 9.

Keary, P., Vine, F.J. & Hallam, A., 1990. *Global Tectonics* 1st ed. A. Hallam, ed., Great Britian: Blackwell Scientific Publications.

Kendall.K & Tabor.D, 1971. An Ultrasonic Study of the Area of Contact Between Stationary and Sliding Surfaces. *Proceedings of the Royal Society A*, 323, pp.321–340.

Knovel, 2014. No Title. Available at: http://app.knovel.com/web/index.v.

Krautkrämer, J., 1969. *Ultrasonic testing of materials*, London: Allen & Unwin.

Królikowski, J. & Szczepek, J., 1993. Assessment of tangential and normal stiffness of contact between rough surfaces using ultrasonic method. *Wear*, 160(2), pp.253–258.

Lamb, H., 1904. On the Propagation of Tremors over the Surface of an Elastic Solid. *Philosophical Transactions of The Royal Society A*, 203, pp.1–42.

Lamb, H., 1917. On Waves in an Elastic Plate. *Proceedings of the Royal Society of London A: Mathematical, Physical and Engineering Sciences*, 93(648), pp.114–128.

Lerch, T.P., Cepel, R. & Neal, S.P., 2006. Attenuation coefficient estimation using experimental diffraction corrections with multiple interface reflections. *Ultrasonics*, 44(1), pp.83–92.

Lo, C.C., 1969. Elastic contact of rough cylinders. *International Journal of Mechanical Sciences*, 11(1), pp.105–106,IN7–IN8,107–115.

Lowe, M.J.S., Alleyne, D.N. & Cawley, P., 1998. Defect detection in pipes using guided waves. *Ultrasonics*, 36(1-5), pp.147–154.

Ltd, P.D., 2008. Product Guide, The essential reference for semi-finished plastic products. , p.205. Available at: http://www.perspex.co.uk/Perspex/media/Media/Technical Library/Product Brochures/PDL-Product-Guide.pdf [Accessed December 12, 2014].

McHale, G. et al., 1999. Surface acoustic wave resonances in the spreading of viscous fluids. *Physical Review B - Condensed Matter and Materials Physics*, 59(12), pp.8262–8270.

McMaster, R.C., 1959. *Nondestructive Testing Handbook* 1st ed. R. C. McMaster, ed., United States of America: The Ronald Press Company.

Mills, R.S., Avan, E.Y. & Dwyer-Joyce, R.S., 2013. Piezoelectric sensors to monitor lubricant film thickness at piston-cylinder contacts in a fired engine. *Proceedings of the Institution of Mechanical Engineers, Part J: Journal of Engineering Tribology*, 227(2), pp.100–111.

Mindlin, R.D., 1949. Compliance of elastic bodies in contact. *Journal of Applied Mechanics*, 16, pp.259–268.

Mulvihill, D.M. et al., 2013. A Comparison of Contact Stiffness Measurements Obtained by the Digital Image Correlation and Ultrasound Techniques. *Experimental Mechanics*, 53(7), pp.1245–1263.

Murfin, A.S. et al., 2000. Laser-ultrasound detection systems: a comparative study with Rayleigh waves. *Measurement Science and Technology*, 11(8), pp.1208–1219.

Nagy, P.B., 1992. Ultrasonic classification of imperfect interfaces. *Journal of Nondestructive Evaluation*, 11(3-4), pp.127–139.

Olympus, Wave Front Dynamics. Available at: http://www.olympus-ims.com/en/ndt-tutorials/transducers/wave-front/.

Onda, 2003. Acoustic Properties of Solids. , p.7. Available at: http://www.ondacorp.com/images/Solids.pdf.

Pialucha, T. & Cawley, P., 1994. The detection of thin embedded layers using normal incidence ultrasound. *Ultrasonics*, 32(6), pp.431–440.

Plessky, V.P. & Simonian, A.W., 1991. Rayleigh wave reflection and scattering on a resonator. *Physics Letters A*, 155(4-5), pp.281–284.

Puttock, M.J. & Thwaite, E.G., 1969. Elastic Compression of Spheres and Cylinders at Point and Line Contact. *National Standards Laboratory Technical Paper*, (25), p.15.

Rayleigh, Lord, 1885. On Waves Propagated along the Plane Surface of an Elastic Solid. *Proceedings of the London Mathematical Society* , s1-17 (1), pp.4–11.

Reddyhoff, T., Dwyer-Joyce, R.S. & Harper, P., 2008. A new approach for the measurement of film thickness in liquid face seals. *Tribology Transactions*, 51(2), pp.140–149.

Roderick, R.L. & Truell, R., 1952. The measurement of ultrasonic attenuation in solids by the pulse technique and some results in steel. *Journal of Applied Physics*, 23(2), pp.267–279.

Royer, D. & Chenu, C., 2000. Experimental and theoretical waveforms of Rayleigh waves generated by a thermoelastic laser line source. *Ultrasonics*, 38(9), pp.891–895.

Rudy, T., 1967. An Ultrasonic Method of Measuring Piston Ring Bore Contact Patterns. In *SAE Technical Paper*. Detroit, pp. 1–8.

Salant, R.F., 2010. Soft elastohydrodynamic analysis of rotary lip seals. *Proceedings of the Institution of Mechanical Engineers, Part C: Journal of Mechanical Engineering Science*, 224(12), pp.2637–2647.

Salant, R.F., 1999. Theory of lubrication of elastomeric rotary shaft seals. *Proceedings of the Institution of Mechanical Engineers, Part J: Journal of Engineering Tribology*, 213(3), pp.189–201.

Stakenborg, M.J.L., 1988. On the sealing mechanism of radial lip seals. *Tribology International*, 21(6), pp.335–340.

Steel-Express, EN24T Steel Properties. Available at: http://www.steelexpress.co.uk/engineeringsteel/EN24T-properties.html [Accessed November 11, 2014].

Tarasenko, A.A., Jastrabìk, L. & Tarasenko, N.A., 2003. Effect of roughness on the elastic surface wave propagation. *The European Physical Journal Applied Physics*, 24(1), pp.3–12.

Tattersall, H.G., 1973. The ultrasonic pulse-echo technique as applied to adhesion testing. *Journal of Physics D: Applied Physics*, 6(7), pp.819–832.

Theplasticshop.co.uk, 2005. Workshop Handbook. , p.28. Available at: http://www.theplasticshop.co.uk/plastic_technical_data_sheets/working_with_perspex_manual.pdf [Accessed December 14, 2001].

Viktorov, I.A., 1967. *Rayleigh and Lamb Waves; Physical Theory and Applications*, New York: Plenum P.

Yibo, P. et al., 2013. Dynamic Mechanical Behaviors of 6082-T6 Aluminum Alloy. *Advances in Mechanical Engineering*, 2013, pp.1–8.

Zhang, C. & Achenbach, J.D., 1988. Numerical analysis of surface-wave scattering by the boundary element method. *Wave Motion*, 10(4), pp.365–374.

Appendix A Exact Expressions of φ, φ', ψ and ψ'

The expressions for ψ, φ, ψ' and φ' are given as (Lamb 1904)

$$\psi = \frac{2k^2\alpha(2\kappa^2 - k^2)^2}{-B} \tag{A.1}$$

$$\phi, \psi' = \frac{k^2(2\kappa^2 - k^2)^3}{-\kappa B} \tag{A.2}$$

$$\phi' = \frac{2k^2\beta(2\kappa^2 - k^2)^2}{-B} \tag{A.3}$$

Where

$$k = \left(\frac{\omega^2\rho}{G}\right)^{1/2}$$

$\omega = Angular\ frequency$

$\rho = Density$

$G = Shear\ Modulus$

$\alpha = (\kappa^2 - h^2)^{1/2}$

$\kappa = \dfrac{\omega}{c}$

$c = Rayleigh\ wave\ speed$

$$h = \left(\frac{\omega^2\rho}{\lambda + 2G}\right)^{1/2}$$

$\lambda = Lam\acute{e}s\ first\ parameter$

$\beta = (\kappa^2 - k^2)^{1/2}$

$$B = -16k^6\kappa\left(1 - \frac{\left(6 - \frac{4h^2}{k^2}\right)\kappa^2}{k^2} + \frac{\left(6 - \frac{h^2}{k^2}\right)\kappa^4}{k^4}\right)$$

Appendix B Asperity Stiffness Approximation

For an elastic contact of rough cylinders with a Gaussian distribution of asperities, the load can be expressed as (Lo 1969; Gelinck & Schipper 1999)

$$p(y,x) = \frac{8}{3} l\eta E' \beta^{1/2} \int_{h}^{\infty} (y-h)^{3/2} \frac{\exp(\frac{-y^2}{2\sigma^2})}{\sigma\sqrt{2\pi}} \, dy \qquad (B.1)$$

By assuming that the cylinder is much stiffer than the asperities during contact, h can be expressed as

$$h(x) = h_o + \frac{x^2}{2R} \qquad (B.2)$$

Following the derivation in pages 47 and 48 i.e. equations (5.18) to (5.25), the expression for distributed stiffness using a Gaussian distribution of asperity height was obtained as:

$$k_{\sigma-asperity} = 4l\eta E' \beta^{1/2} \int_{h}^{\infty} (y-h)^{1/2} \frac{\exp(\frac{-y^2}{2\sigma^2})}{\sigma\sqrt{2\pi}} \, dy \qquad (B.3)$$

(B.3) represents the distributed stiffness at the interface. To obtain the total stiffness (B.3) is integrated along the x-coordinate to obtain

$$K_{\sigma-asperity} = \int_{-\infty}^{\infty} k_{\sigma-asperity} \, dx \qquad (B.4)$$

Both (B.1) and (B.3) are numerically integrated using the trapezoidal method to obtain the following approximate expressions

$$p(y,x) = \left(\frac{8}{3} l\eta E_3 \beta^{1/2}\right) \times 0.11\sigma^{1.4} e^{\frac{-1.7h}{\sigma}} \qquad (B.5)$$

$$k_{\sigma-asperity} = \left(4l\eta E' \beta^{1/2}\right) \times 0.6\sigma^{0.5} e^{\frac{-1.5h}{\sigma}} \qquad (B.6)$$

To calculate total asperity stiffness, expressions for h are required. They are determined on a case by case basis. Here, the sample case of a steel-steel contact in Chapter 4 where $\eta = 10^9$ m^{-2}, $\beta = 20\mu$m and $\sigma = 1\mu$m is assumed. For an interface in static contact, the equilibrium of forces must be fulfilled (Beheshti & Khonsari 2012) . Hence

$$Total\ load, P = \int_{-\infty}^{\infty} (B.5)\ dx$$

By substituting the parameters and performing the integration, the equation above can be expressed as

$$P = 1882e^{-1.7 \times 10^6 h_o} \tag{B.7}$$

Rearranging (B.7) for h_o

$$h_o = -5.88 \times 10^{-7} \ln(5.3 \times 10^{-4} P) \tag{B.8}$$

Having found h_o, the full expression for h can be expressed as

$$h(x) = -5.88 \times 10^{-7} \ln(5.3 \times 10^{-4} P) + \frac{x^2}{2R} \tag{B.9}$$

Substituting (B.9) into (B.6) followed by an integration using (5.26), the expression for asperity stiffness at the interface can be calculated to give

$$K_{\sigma-asperity} = 3.54 \times 10^6 P^{0.88}\ N/m \tag{B.10}$$

The procedure here can be repeated for different η, β and σ.